Experimental Constraints on the Chromite-Melt Partitioning Behaviour of Rhenium and Platinum-Group Elements

by

Parisa Sattari

A thesis submitted in conformity with the requirements
for the Degree of Master of Science,
Graduate Department of Geology
University of Toronto

0-612-53465-0

ACKNOWLEDGEMENTS

This thesis has required input, collaboration and inspiration from numerous people. First, I would like to appreciate my supervisor, Dr. J. M. Brenan, who introduced me to the world of experimental petrology and its implications for understanding igneous processes. I am grateful to him for his continuous support, encouragement, exchanging ideas and his hands on expertise from the start to the completion of this thesis. I hope to retain the remarkable enthusiasm and curiosity of discovery that I often saw in him.

I thank my supervisory committee members; Grant Henderson and Tony Naldrett for their input and excitement for my research.

I also thank Dr. W. McDonough, at Harvard University, and Dr. I. Horn, at E.T.H., (Zurich), for their support and assistance in LA-ICP-MS analyses and interpretations of data during the course of my thesis.

I thank our technical services staff at the Department of Geology for their support during the completion of this project. Claudio Cermignani is appreciated for his assistance and helpful suggestions in EMP analyses. He is the mediator relating the user and the Cameca SX50 probe with its UNIX-software, especially at times when the communication seems futile. The staff in the Polish/Thin section lab are thanked for preparing samples for analysis. Karyn Gorra is thanked for her artistic expertise in photography and slide shows. Dr. N. Coombs's assistance is also appreciated in SEM training at the Geology Department.

For essential financial support, I am grateful to the Department of Geology for nominating me for an Ellesworth Award in Mineralogy, and Ontario Graduate Scholarship during the course of my studies.

I would like to thank the graduate and undergraduate students in the high pressure lab of the Geology Department whom I met, built and restructured equipment in the lab, shared ideas and good times with.

I wish to thank my father, Bahman and my mother, Azam, deeply for their incredible love and support throughout my thesis. Special thanks to my sisters, Andrea (M.Sc.), and Panteh-a for their remarkable advice and inspiration over the past years, even though I frequently missed attending plans as I promised, and postponed the tasks at hand to a time in the future. This thesis is the result of their tremendous encouragement.

Lastly, I would like to thank my fiancé, Andrew G. Conly (PhD-candidate), for being my listener when I needed an ear, providing endless support during my downfalls, and sharing his expertise in CorelDraw 7,8, and 9 to produce artistic graphs. His efforts to bring a smile on my face when a high-pressure experiment died, and his encouragement to overcome my frequent writer blocks, are greatly appreciated.

Abstract

Experimental Constraints on the Chromite-Melt Partitioning Behaviour of Rhenium and Platinum-Group Elements

Master of Science, 2000

Parisa Sattari, Department of Geology, University of Toronto

Abundant geochemical and petrological data exists to suggest that chromite may be an important phase in concentrating and fractionating the PGEs in mafic/ultramafic systems. To investigate this possibility, chromite/silicate- and sulphide-melt partitioning experiments have been conducted at conditions of pressure, temperature and fO_2 appropriate for basalt genesis. Trace elements in run products were determined *in situ* using laser ablation ICP-MS, which allowed us to discern both phase homogeneity and detect the presence of sulphide or alloy contaminants. Experiments yielded absolute chromite/silicate melt partition coefficients (Ds) for Re (0.15) and maximum values for the PGEs (Ru< 10.1; Os <4.3; Ir <1; Pd <0.23; Rh<0.17). Results indicate that Re and some PGEs are incompatible in chromite, whereas compatibility of other PGEs is significantly less than previously considered. As an alternative to the PGEs being in solid solution in the chromite structure, textures produced in our experiments show entrapment of PGE-rich phases (sulphide/alloy) during chromite crystallisation, which may best explain the PGE-chromite association.

TABLE OF CONTENTS

TITLE PAGE I
ACKNOWLEDGMENTS II
ABSTRACT IV
TABLE OF CONTENT V
LIST OF TABLES VI
LIST OF FIGURES VIII

CHAPTER I: INTRODUCTION 1

CHAPTER II: EXPERIMENTAL AND ANALYTICAL TECHNIQUES 10

2.1 EXPERIMENTAL TECHNIQUES 10
2.1.1 Preparation of samples 10
2.1.2 Control of oxygen fugacity 14
2.1.3 Description of the piston cylinder apparatus 17
2.1.4 Temperature control of the piston cylinder apparatus 18
2.1.5 Liquidus temperature determination 21
2.1.6 Growth of chromite crystals from basaltic melt 21
2.1.7 Low pressure experimental protocol 24
2.2 ANALYTICAL TECHNIQUES 25
2.2.1 Electron microprobe analysis 25
2.2.2 Trace element analysis 28

CHAPTER III: RESULTS OF EXPERIMENTS 31

3.1 TEXTURAL OBSERVATION OF RUN PRODUCTS 31
3.1.1 Run products at 1 GPa 31
3.1.2 Run products at 1 atm 32
3.2 MAJOR ELEMENT COMPOSITIONS 38
3.2.1 Estimation of oxygen fugacity based on Cr solubility in melt 38
3.2.2 Major element chemistry of the run product phases 40
3.3 TRACE ELEMENT CHEMISTRY 47
3.3.1 Trace element analyses of phases produced in the run products 47
3.3.2 Trace element heterogeneity in analysed phases 50
3.3.3 Sulphide melt/silicate melt partition 59
3.3.4 Chromite/Silicate melt partition coefficients 61

CHAPTER IV: DISCUSSION OF RESULTS 63

4.1 COMPARISON OF $D_{\mathrm{METALS}}^{\mathrm{SULPHIDE\text{-}MELT/SILICATE\text{-}MELT}}$ WITH OTHER STUDIES 63
4.2 COMPARISON OF $D_{\mathrm{METAL}}^{\mathrm{MINERAL/SILICATE\text{-}MELT}}$ WITH OTHER STUDIES 66
4.3 CONTROL OF THE SPINEL STRUCTURE ON Re AND PGE PARTITIONING 69
4.4 IMPLICATIONS FOR THE BEHAVIOUR OF Re IN BASALTS AND Re/Os FRACTIONATION 73
4.5 CHROMITE AS A PGE COLLECTOR 74

CHAPTER V: CONCLUSIONS 75

REFERENCES 76

APPENDICES 84

List of Tables

Table A1. Summary of PGE contents (ppb) in various rock types........................84

Table A2.a. Experimental details: Starting material..86

Table A2.b. Summary of liquidus determination experiments...............................86

Table A2.c. Run conditions for partitioning experiments.....................................87

Table A2.d. Summary of all the phases produced in each experiments.....................88

Table A3.1. Operating conditions employed for glass- EMP analyses.......................89

Table A3.2. Operating conditions employed for chromite- EMP analyses..................90

Table A3.3. Operating conditions employed for olivine- EMP analyses....................90

Table A3.4. Operating conditions employed for clinopyroxene..............................91

Table A3.5. Operating conditions employed for alloy phases................................91

Table A3.6. Operating conditions employed for sulphide phases............................92

Table A4. Minimum detection limit (ppm) of Re and PGEs in NIST 610 glass.........93

Table A5.1. Summary of major element compositions (wt %) in glass.....................94

Table A5.2. Summary of major element compositions (wt %) in clinopyroxene..........94

Table A5.3. Summary of major element compositions (wt %) in chromite................95

Table A5.4. Summary of major element compositions (wt %) in olivine....................96

Table A5.5. Summary of major element compositions (wt %) in sulphides................96

Table A5.6. Summary of major element compositions (wt %) in alloy phases.............97

Table A6.1. Summary of Ni, PGEs and Re concentrations in glass..........................98

Table A6.2. Summary of Ni, PGEs and Re concentrations in chromite......................99

Table A6.3. Summary of Ni, PGEs and Re concentrations in olivine.......................100

Table A6.4. Summary of Ni, PGEs and Re concentrations in sulphides...................100

Table A7.1. Summary of sulphide/silicate melt partition coefficients......................101

Table A7.2. Summary of chromite/silicate melt partition coefficients 102

Table A.I. Summary of recalculations of chromite analyses................................103

Table A.II. Summary of recalculations of olivine analyses..................................107

List of Figures

Figure 1. C1-Chondrite normalised diagram depicting PGE and Re abundances in different igneous rocks....2

Figure 2. Sulphide/silicate melt and spinel/silicate melt partition-coefficients from the experimental literature....7

Figure 3. Schematics representation of graphite-lined Pt capsule configuration for high-pressure experiments....13

Figure 4. Variations of oxygen fugacity with the dissolved CO_2 content of an iron-bearing silicate melt....16

Figure 5.1. Schematic representation of the end loaded piston cylinder apparatus ...19

Figure 5.2. Schematics of the sample assembly in pressure vessel....20

Figure 6. Time-temperature history employed for partitioning experiments 23

Figure 7.a. Backscattered electron (BSE) image of PGE2b showing common phases produced in high pressure runs....33

Figure 7.b. BSE image of a subhedral chromite in PGECo 34

Figure 7.c. Digitized reflected light photomicrograph of chromite with sulphide inclusion in the PGE2b run product....34

Figure 7.d. Digitized reflected light photomicrograph of run product from the experiment PGE1d....35

Figure 7.e. BSE image of a sulphide globule in the PGE1d run product 35

Figure 7.f. BSE image of a sulphide globule in PGE5a experiment showing alloy phases....36

Figure 7.g. Digitized reflected light photomicrograph of the analysed alloy phase in the PGECo run product....36

Figure 7.h. Digitized reflected light photomicrograph of an equant chromite crystal in the PGE8a experiment....37

Figure 7.i. Digitized reflected light photomicrograph of plan view of the PGE8a.... 37

Figure 8. Plot of estimated oxygen fugacity based on Cr-solubility in melt....39

Figure 9 Ternary diagram depicting the chromite compositions in this study....43

Figure 10. Major element concentration profile measured by EMPA of a chromite..44

Figure 11. Plot of Cr^{3+}, Al^{3+}, and Fe^{3+} as a function of oxygen fugacity....45

Figure 12. Ternary plot (in at %) depicting the sulphide compositions.................46

Figure 13. Plot of calculated fO_2 and the Re abundances in the melt...................49

Figure 14.1. Plot of intensity (cps) against time (s) for representative chromite..........52

Figure 14.2. Plot of intensity (cps) against time (s) for olivine.............................53

Figure 14.3-4. Plots of intensity (cps) against time (s) for representative glasses.........54

Figure 15.1. Plot of trace element profiles for the run product of IPRe4.................56

Figure 15.2. Plot of trace element profiles for the run product of PGECoS..............57

Figure 15.3. Plot of trace element profiles for the run product of PGECo................58

Figure 16. Variation of sulphide-melt/silicate-melt partition coefficients for Ni, and Re as a function of time..60

Figure 17. Pot of Ni abundance in the silicate melt vs. the chromite-melt partition coefficient..62

Figure 18. Comparison of sulphide/silicate melt partition coefficients with previous determinations..65

Figure 19. Comparison of chromite/silicate melt partition coefficients of this study with previous estimates..68

Figure 20. Spinel/melt partition coefficient as a function of ionic radius.............72

CHAPTER I: INTRODUCTION

The geochemistry of the platinum group elements (PGEs) has been extensively studied over the past decade and despite such efforts, significant gaps still exist in our understanding of their behavior. Platinum group elements are classified geochemically as both highly siderophile and chalcophile due to their enhanced partitioning into iron and sulphur rich phases. According to the growing geochemical database, platinum group elements are divided into two groups, the IPGEs (Ir-PGEs) and PPGEs (Pd-PGEs) (Rollinson, 1993). The former corresponds to ruthenium (Ru), osmium (Os), and iridium (Ir), whereas the latter include rhodium (Rh), platinum (Pt), and palladium (Pd). Their abundances in rocks are usually portrayed on C1-Chondrite normalized plots in which they are arranged in the order of decreasing melting point (Os, Ir, Ru, Rh, Pt, Pd). The concentration of PGEs in mafic and ultramafic rocks can vary from values in the range of ppt in basaltic rocks to ppm levels in sulphide rich deposits, which is a consequence of the differing affinities of these elements for silicate, oxide, alloy and sulphide phases. Abundances and PGE patterns for different igneous rocks are presented in Table A1 (Appendix) and Figure 1. The IPGEs and PPGEs behave differently during magmatic processes such as fractional crystallisation, and partial melting, which results in the distinctive fractionation of the PGEs and Re (a PGE-like element) as portrayed in Fig 1. For this reason, the extent of IPGE/PPGE fractionation in a sample is frequently measured by the Pd/Ir. It is important to note that mantle rocks such as garnet or spinel lherzolites show unfractionated patterns (flat curves) for Re and PGEs (Mitchell and Keays, 1981; Morgan et al., 1981; Lorand et al., 1998; Barnes et al., 1985). Komatiites, which are the product of high

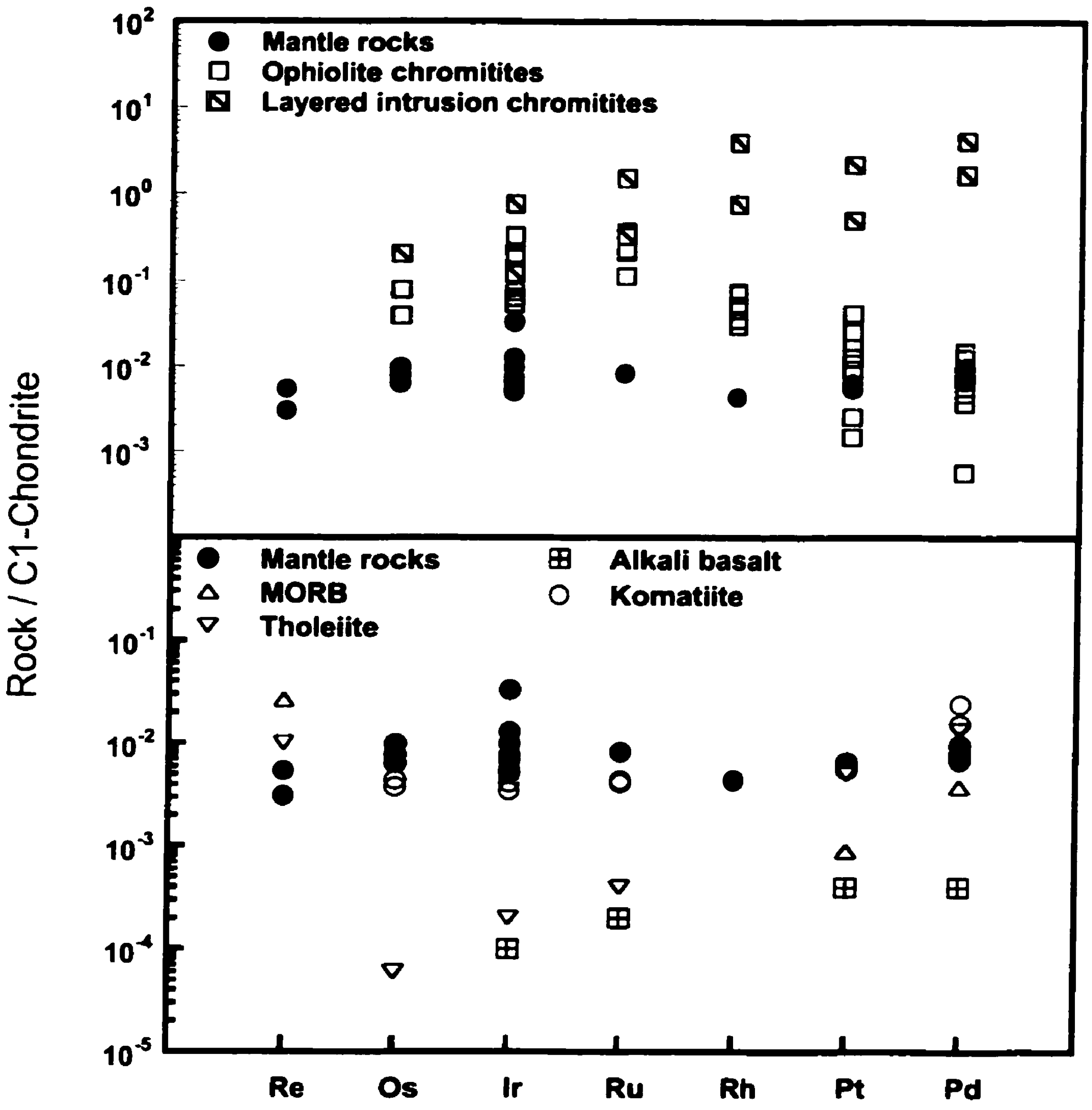

Figure 1. C1-Chondrite normalised diagram depicting PGEs and Re abundances in different igneous rocks. References and data are summarized in Table A.1.

degrees of partial melting and present undifferentiated melt, only have slightly fractionated PGE abundances (Pd/Ir ~<10) (Brugmann et al., 1987). In contrast, other mantle-derived rocks, which are produced at lower degrees of melting, such as mid ocean ridge basalt (MORB), tholeiites, and alkali basalt, show depletion of IPGEs with Pd/Ir ratios in the range of ~5-100 (Allegre and Luck, 1980; Hauri and Stanely, 1997; Rehkamper et al., 1999).

Insights into the factors that result in high concentration of PGEs, and their relative fractionation in igneous rocks have been provided by several researchers (Barnes, et al., 1985; Barnes and Picard, 1993; Maier and Barnes, 1999; Peach and Mathez, 1996; Talkington and Lipin, 1986; Von Gruenewaldt et al., 1986). Factors include control by segregation of sulphide melt, separation of PGE rich sulphides or alloy phases, fractionation of primary liquidus minerals such as olivine or chromite, and syn to post-magmatic alteration by hydrothermal fluids. Thus far, experimental studies have demonstrated the importance of sulphide melt and metallic phases in concentrating the PGEs and Re during magmatic processes, with values of sulphide and metal - silicate melt partition coefficients (D-values) exceeding 10^3 (Bezman et al., 1994; Crocket et al., 1992, 1997; Fleet et al., 1996; O'Neill, et al., 1994; Peach and Mathez, 1993, 1996; Peach et al., 1994; Peck, et al., 1992). However, Peach et al., (1994) measured similar sulphide melt-silicate melt partition coefficients for Pd and Ir of 10^4 at 1400 °C and 0.8 GPa which suggests that sulphide/silicate melt equilibrium is not a viable means for IPGE/PPGE fractionation. Their results emphasized the importance of phases other than sulphide liquid, such as oxides or alloys, in fractionating the PGEs.

The role of syn to post-magmatic fluids in concentrating PGEs in mafic and ultramafic rocks has only recently been investigated. Based on the presence of hydrothermal quartz and chlorine rich apatite associated with PGE-rich sulphides in samples from the Stillwater complex, Boudreau and McCallum (1986;1992) proposed that transport and concentration of the PGEs was by chloride species in an aqueous vapor phase. Wood (1987) calculated the volatility of PGEs as metals, oxides and chloride species at magmatic conditions. His results showed that Pd and Ru can be transported as chloride species when HCl is more abundant than H_2O and that Os and Ru may be mobile as oxide-species under relatively oxidizing conditions (fO_2 from $10^{-3.8}-10^{-8.9}$) at temperatures greater than 1130 °C. Wood (1987) also pointed out that transitional metals such as Ni, Fe, and Cu are more volatile than PGEs at high temperature, and thus, hydrothermal processes should also produce an associated enrichment of these elements along with the PGEs. Furthermore, experimental studies of Fleet and Wu (1993) showed that high concentrations of PGEs dissolve in dry, sulfurous, and saline post magmatic fluids at high temperatures. In their study, Pd, and Pt were the dominant PGEs transported, which could explain the elevated PPGE abundances in some PGE deposits associated with mafic/ultramafic igneous rocks.

Although data from both natural assemblages and experiments exist to at least partially evaluate the role of sulphides, alloys, and fluids on controlling both the absolute and relative PGE abundances in different mafic/ultramafic igneous rocks, observations to evaluate the role of primary liquidus phases such as chromite and olivine in PGE fractionations are few and yield ambiguous results. Naldrett et al., (1979) and Crocket et al., (1979), found high concentrations of IPGEs in olivine separates from komatiites, which resulted in the proposal that olivine could fractionate the PGEs during partial melting or initial stages of crystallisation. Hart and Ravizza (1996) analysed mineral separates from spinel lherzolites from Kilbourne hole, New Mexico and suggested that Os is compatible in olivine and Cr-bearing spinel, with calculated mineral-silicate melt partition coefficient greater than ~10. Mitchell and Keays (1981) reported PGE abundances in whole rock and mineral separate analysis from spinel lherzolite xenoliths. Their work revealed that other than interstitial sulphides, only Cr-spinel yielded significant PGE concentrations. Further support for a PGE association with Cr-rich spinel or chromite comes from the correlation between Ir and Cr in ultramafic rocks as reported for Komatiites from Gorgona (Brugmann et al., 1987), cumulates of Fred's flow, Munro Township (Crocket et al., 1986) and different lithologies of the Fiskenaesset Complex (Morgan, et al., 1976). In addition, cumulate chromitites from different igneous settings, such as those in layered intrusions, ophiolites, and alpine-type peridotites (McLaren and DeVilliers, 1982; Page et al., 1982; Peck and Keays, 1990, Peck et al., 1992; Talkington and Lipin, 1986; Von Gruenewaldt and Merkle, 1995) are known for anomalously high PGE concentrations. For example, the largest ore deposits of PGEs are related to chromitites in layered intrusions, such as the UG2-layer of the Bushveld and the J-M reef of the Stillwater Complexes (McLaren and DeVilliers, 1982; Page et al., 1976). These chromitites have been shown to hold a total of 7 ppm and 960 ppb of all PGEs, respectively. The chromitites of ophiolites show high concentrations of Os, and Ir relative to Rh, Pt and Pd with Pd/Ir<~1. In contrast, chromitites from layered intrusions show elevated Rh, Pt, and Pd relative to the IPGEs with Pd/Ir typically greater than 10. As shown in Fig. 1, it is clear that chromitites are characterized by their distinctive and variable IPGE/PPGE fractionation.

Experimental studies of Capobianco and Drake (1990) and Capobianco et al., (1994) demonstrated the compatibility of Ru, Rh and incompatibility of Pd in spinel, magnetite, and Cr-bearing magnetite at relatively high oxygen fugacities (fO_2) in the range of $10^{0.68}$–$10^{-5.78}$

at one atmosphere and high temperatures (from 1265 to 1400 °C). Figure 2 summarizes their partitioning data, and provides a comparison with the sulphide-silicate melt partition coefficients from recent experimental work. It is notable that their work of 1994 showed large magnetite-silicate melt partition coefficients for Rh and Ru (D_{Ru} from 100 to >4000 and D_{Rh} 250 ±120), that are comparable in magnitude to partition coefficients between immiscible sulphide and silicate melts. As a consequence of this partitioning data, Capobianco and coworkers have suggested that the crystallisation of spinel group minerals, like chromite, may concentrate and fractionate the PGEs in igneous systems.

Despite the evidence supporting the possible role of chromite in concentrating and fractionating the PGEs, there also exists observational and analytical data that counter this notion. For example, Lorand et al., (1998) determined the PGE concentrations in a suite of orogenic lherzolites from the North Pyrenean Metamorphic zone, and found no correlation between PGE content and Cr-spinel abundance. There was a systematic positive correlation between PGE and sulphur content, however, reflecting the control of sulphide. Maier and Barnes (1999) explained the association of the elevated PGE abundances with chromitites of the Bushveld Complex by fractionation of mono sulphide solid solution (mss) followed by physical separation of mss cumulates from residual sulphide liquid. Their work emphasized the importance of mss fractionation from a sulphur poor silicate melt as the controlling factor for PGE fractionation, rather than sulphide liquid / alloy segregation or crystallisation of oxide phases. Finally, it is important to note that the experimental studies of Capobianco and Drake (1990) and Capobianco et al., (1994) conducted at oxygen fugacities that were more oxidizing ($\sim 10^{0.68}$ - $10^{-5.78}$) than is reasonable for terrestrial basalt petrogenesis (fO_2 of $10^{-8.3}$ – $10^{-10.3}$ at 1200°C; Christie et al., 1986). At oxidizing

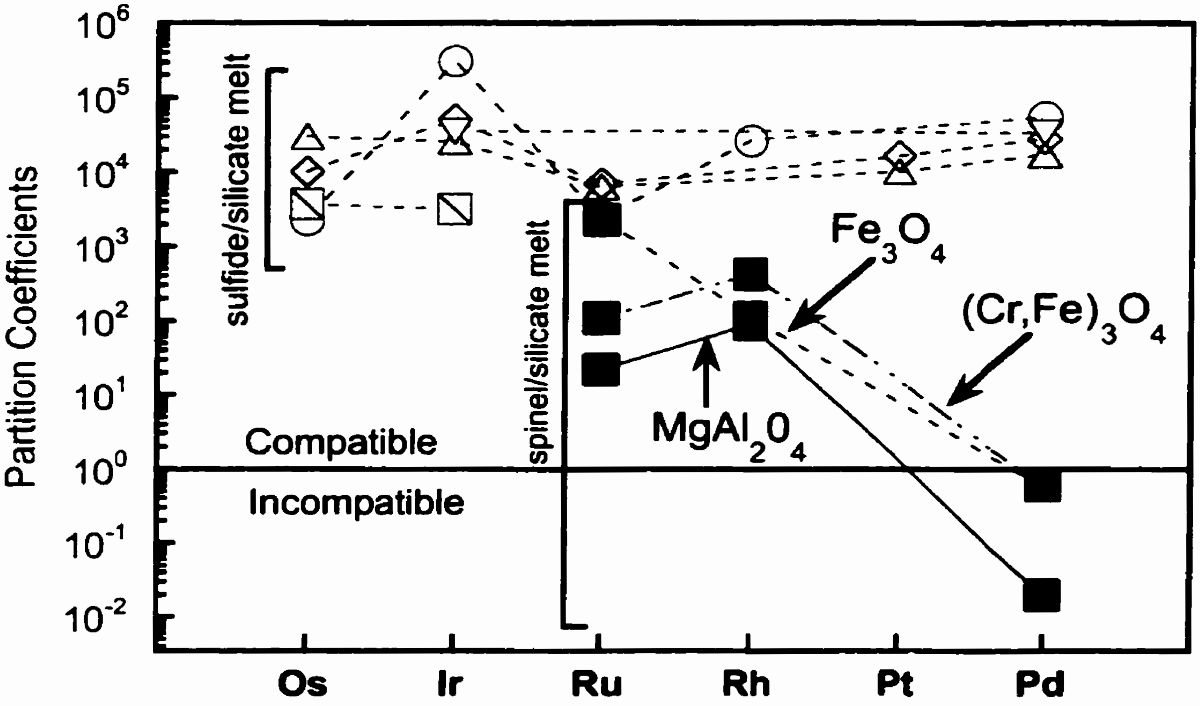

Figure 2. Sulphide/silicate melt (Bezmen et al., 1994; Crocket et al., 1992, 1997; Fleet et al., 1996; Peach et al., 1994), and spinel/silicate melt (Capobianco and Drake, 1990; Capobianco et al., 1994) partition coefficients based in the recent experimental literature.

conditions, the PGEs are thought to be dissolved predominantly as 3^+ (or higher) species, and thus readily substitute for trivalent cations such as Fe, Al, Cr, in the spinel structure. The experimental work of Borisov et al., (1993); O'Neill et al., (1994); and Ertel et al., (1999) pointed out that Rh, Pt, Pd, Ir and Re exhibit progressively lower valence states in silicate melts (i.e. 2^+ or lower) as fO_2 is reduced (from fO_2 of 10^{-2} to $<10^{-5}$). As demonstrated by Beattie (1994) and Blundy and Wood (1994), variation in ionic radius and valence state of a cation exerts a major control on the compatibility of an element, owing largely to the increased lattice strain resulting from the substitution of a cation whose size is different from the major substitutive cation. The shift in the valence state of PGEs in silicate melts in response to a reduction in fO_2 may result in changes in their ionic radius to render them as incompatible in spinel group minerals.

The focus of this thesis was to obtain chromite/silicate-melt partitioning data for PGEs and Re in order to assess the role of chromite in concentrating, and potentially fractionating the PGEs, and Re in igneous systems. Experiments were conducted at both 1 atm and 1 GPa at 1350-1330 °C at an oxygen fugacity of $\sim10^{-8.5}$ to $10^{-9.7}$. In these experiments, the fO_2 was defined using gas mixtures of CO, and CO_2 in a sealed vertical tube furnace for low-pressure experiments and coexisting CO, CO_2, and graphite (CCO) for high-pressure runs. Analyses of the run products for PGEs was performed using laser ablation inductively coupled mass spectrometry (LA-ICP-MS) which is an *in situ* analytical technique that combines micron-scale spatial resolution with high element sensitivity. In these experiments, PGEs and Re were introduced using doped sulphide melt or an alloy mixture. In addition to constraints on chromite/silicate-melt partitioning, we have also provided the first validation of sulphide/silicate melt PGE partition coefficients using an *in situ* analytical technique.

CHAPTER II: EXPERIMENTAL AND ANALYTICAL TECHNIQUES

2.1 Experimental techniques

In this investigation of the partitioning of PGEs among chromite, sulphide and/ or alloy and silicate melt, we sought to satisfy several criteria. First, chromite must be grown at an oxygen fugacity that is controlled and relevant to basalt genesis, and at a value where the oxidation state of PGEs are reasonably well documented. Second, the PGEs must be present at high enough levels in the melt and chromite in order for their concentrations to be above the detection limits of the LA-ICPMS (10-100 ppb). Third, crystal-melt equilibrium must be approached as closely as possible. Fourth, the size of the crystals grown during experiments must be large enough for adequate sampling with the laser ablation technique, since the minimum detection limit improves with increasing spot size. As a final point, the crystallised chromites must be inclusion-free to ensure that analyses are obtained from a pure phase. The experimental techniques outlined below were designed to satisfy the above requisites.

2.1.1 Preparation of samples

The silicate melt composition employed in our experiments is the synthetic equivalent of a mafic dyke, located at the intersection between HWY 401 east and route 15 north (Ontario, Canada). This composition is well documented in terms of the chromite saturation surface in temperature-oxygen fugacity space as documented by Hill and Roeder (1974), Roeder and Reynolds (1991) and Murck and Campbell (1986). This starting composition was synthesized from a mixture of high purity oxides and carbonates that were weighed and then thoroughly mixed under ethanol in an agate mortar. The mixture was dried, then heated slowly to 1100 °C to ensure complete decarbonation. This was accomplished by placing the starting material in a Pt-crucible inside a box furnace and increasing the temperature at a rate of 3 °C per minute. This step also assured preliminary chemical interaction among reagents. Following this process, the starting material was equilibrated at the magnetite-hematite solid buffer assemblage at 815 °C (± 5), to further ensure a high initial ferric/ferrous ratio (Fe^{+3} / Fe^{2+}) of the starting material.

In these experiments PGEs were added in three different ways: a) PGE-bearing Ni-Fe sulphide liquids (at various levels from 500 ppm to 5 wt %), b) as pure alloys, c) as PGE-bearing solutions. The exact content of the PGE and Re for each experiment and the proportions of the sulphide melt or alloys to silicate melt employed in each run are summarized in Table A2-a. For sulphide saturated runs (IPRe4; PGE1,2 b; PGE1,2 c; PGE 1d; PGE1e; PGE5a), the sulphide melt consisted of a mixture of pure Fe, Ni, S powder in a 50:20:30 ratio which was doped with high purity Re and PGE metal in the amounts summarized in Table A2-a. The alloy composition for PGECo and PGECoS samples was prepared using a mixture of pure cobalt metal powder and 5 wt % of each PGEs and Re. Cobalt was added to these experiments with the initial intent of using it as a reference element for LA-ICP-MS analysis, due to its high solubility in silicate melt and compatibility in spinel (D_{Co} 4.7-8.3, Horn et al., 1994). In the sulphur poor experiment (PGECoS), sulphur was added as a dilute Na_2SO_3 solution for a total of 0.01 wt % sulphur to the charge. For the sulphide-free PGE-undersaturated runs (PGE8a and PGE8b), samples were spiked with AA standard solutions of Os, Ru, Rh, Pd in 20 wt% HCl. The stock solutions were diluted using a HCl solution (~ 37 wt%) by a factor of eight in order to add PGEs at ppb levels to the charges (Table A2-a). The solution was added to the charge and placed under a heating lamp for one hour to dry. Figure 3.1 is a schematic representation of the graphite-lined Pt capsule configuration employed in high- pressure runs. For all piston cylinder experiments charges were prepared as follows. Graphite capsules with accompanying lids were manufactured in house utilizing high purity graphite rods of 99.99% C. Graphite rods were drilled and cut into sizes of 8 x 3 and 8 x 5 mm. The graphite capsules and their lids were cleaned in acetone and stored in a drying oven at 110 °C. Platinum tubing of 0.127" wall thickness and diameters of 3.5 and 5 mm were cut to lengths of 1.2 cm, annealed, then welded on one end. Approximately 10 (± 0.1) mg of basalt glass was mixed thoroughly with 0.6 (±0.1) mg of Fe-Ni sulphide or PGE alloy mix using a clean razor blade and loaded into the graphite capsule. A lid was inserted on top of the capsule, and the entire assembly was then placed inside an outer Pt-capsule of an appropriate size and sealed using an arc welder. The starting material for the PGE1d, PGE1e and PGE5a run products were loaded into a 5 mm diameter graphite capsule, but run without an outer Pt-capsule. This configuration was employed to avoid the Pt-contamination encountered in some of the sulphide-saturated experiments (PGE1,2 b; PGE1,2 c, and IPRe4). Preliminary experiments showed that applying a 1:20 ratio of sulphide to silicate melt produced several sulphide globules of 100-250 μm in diameter in the run products. This ratio was employed for all of the sulphide-saturated runs.

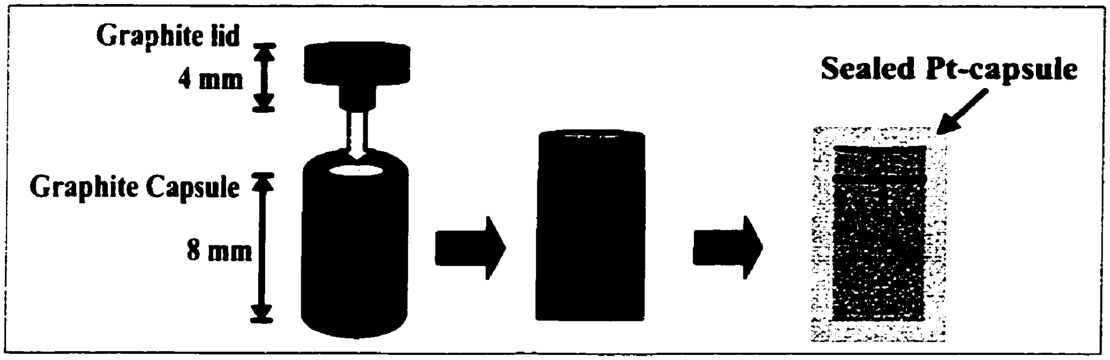

Figure 3. Schematic diagram showing the graphite-lined Pt capsule configuration for high pressure experiments.

2.1.2 Control of oxygen fugacity

Oxygen fugacities in our experiments were controlled in two ways that will be discussed individually below. For the experiments carried out at 1 GPa, the fO_2's were constrained by the Fe^{3+}/Fe^{2+} ratio in the starting material, and the final concentration of dissolved CO_2 in the melt (Holloway et al., 1992). A constant fO_2 was achieved using a graphite capsule, which not only prevents iron loss to the Pt-capsule, but also reacts with the ferric iron of the melt to produce dissolved CO_2 and FeO. The following equations express the way that the CO-CO_2-graphite system acts to buffer the fO_2 of a closed system at high pressure (Holloway et al., 1992).

$$C_{(graphite)} + O_2 \Leftrightarrow CO_{2\,(melt)} \qquad (2\text{-}1)$$

$$CO_{2\,(melt)} + O^{2-}_{(melt)} \Leftrightarrow CO_3^{\;2-}\,(\text{dissolved}) \qquad (2\text{-}2)$$

$$2Fe_2O_{3\,(melt)} \Leftrightarrow 4FeO_{(melt)} + O_2 \qquad (2\text{-}3)$$

$$C_{(graphite)} + O^{2-}_{(melt)} + 2\,Fe_2O_{3\,(melt)} \Leftrightarrow CO_3^{2-}{}_{(melt)} + 4\,FeO_{(melt)} \qquad (2\text{-}4)$$

Thus, the initial Fe^{3+}/Fe^{2+} ratio together with the dissolved CO_2 content of the glass, constrain the final oxygen fugacity of a closed system at fixed pressure and temperature. This fO_2 corresponds to the point at which the fO_2 calculated based on the ferric/ferrous ratio in the melt (equation 3) and the fO_2 values calculated from dissolved CO_2 (equations 2-1 and 2-2) are equal. The maximum fO_2 that can be achieved by this technique corresponds to vapour saturation (i.e. the CCO buffer). Figure 4 portrays the relationship between the fO_2, initial Fe^{3+}/ Fe^{2+} ratio and the dissolved CO_2 of the melt and serves to illustrate the evolution of fO_2 in our experimental system. We could not calculate the final fO_2 of the system a priori due to a lack of information on the initial Fe^{3+}/Fe^{2+} ratio of the system. Instead, we imposed a high initial ratio (by pre-oxidation of melt at MH solid buffer assemblage at 815 °C), and then estimated the final fO_2 of the sample using chromium solubility systematics.

The oxygen fugacity of 1 atm experiments was controlled using a mixture of CO and CO_2 gases in a sealed vertical tube furnace. The fO_2's were calculated using the "COSHmix" program (courtesy of Dr. Victor Kress) which utilizes a RAND free energy minimization algorithm to calculate equilibrium gas speciation based on data from JANAF thermodynamic tables (Kress 1997). The CO and CO_2 gas flow rates were controlled using calibrated flow meters, and the accuracy of the furnace fO_2 was checked against the nickel-nickel oxide (Ni-NiO) buffer (Huebner and Sato, 1970).

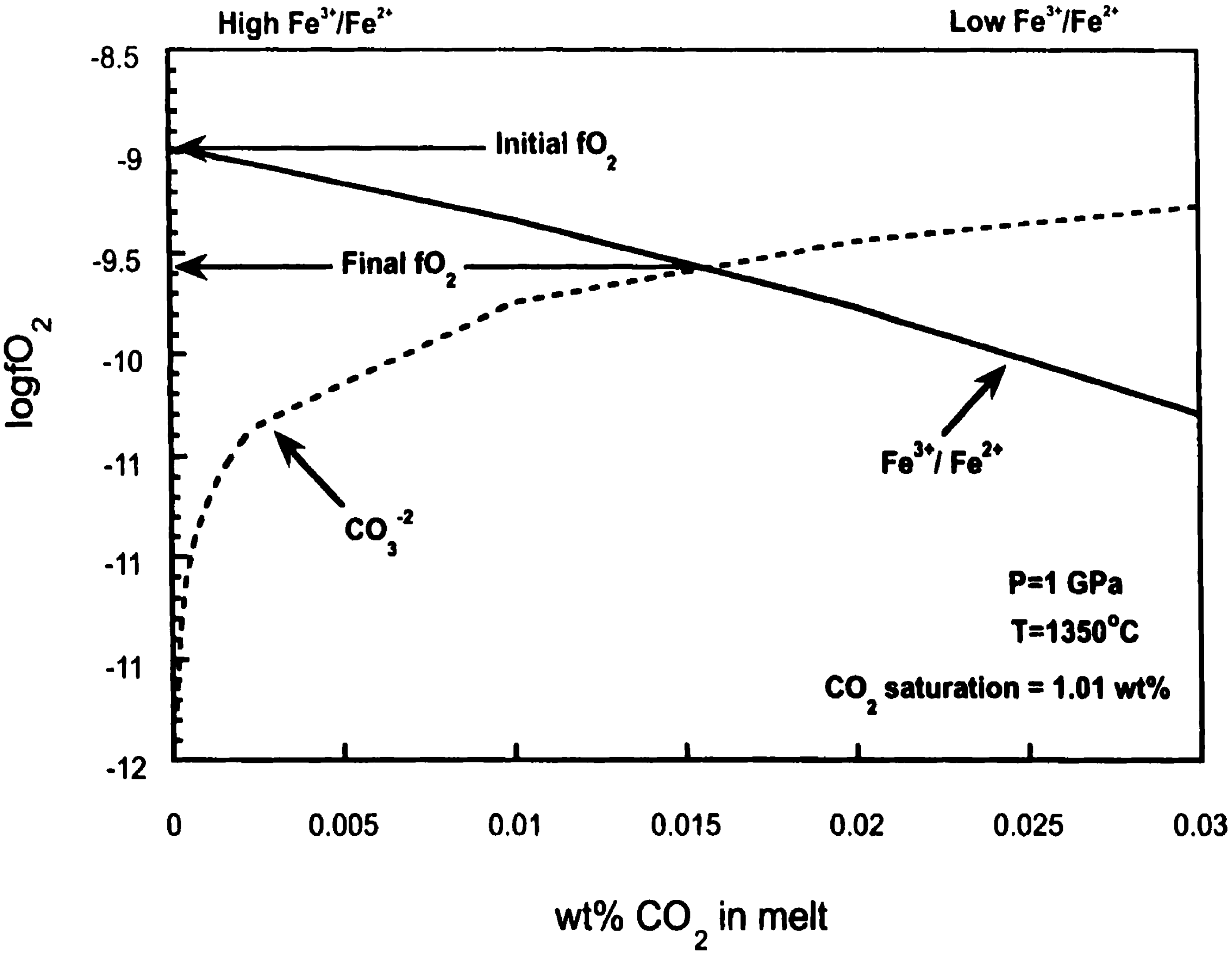

Figure 4. Plot of oxygen fugacity as a function of dissolved CO_2 and Fe^{3+}/Fe^{2+} ratio in the melt. This plot illustrates the evolution of fO_2 during oxidation of graphite after Holloway et al., (1992). The solid curve determines the fO_2 using Fe^{3+}/Fe^{2+}, where as the dashed line calculates it based on the dissolved CO_2 in the silicate melt. The point of intersection of the two curves defines the equilibrium or the final fO_2 of the system, which is the maximum fO_2 that the system can reach.

2.1.3 Description of the piston cylinder apparatus

All the experiments at 1 GPa were performed using the end loaded, piston cylinder apparatus located in the High Pressure Laboratory in the Department of Geology. This apparatus is based on the Boyd and England (1960) design and generates pressure by compressing a sample assembly with a ¾" diameter piston. Figure 5.1a and 5.1b represent the schematic diagrams of the sample configuration inside the pressure vessel and the piston cylinder apparatus. The sample assembly consists of a graphite tube furnace, encased in sleeves of pyrex glass and compressed NaCl (Fig 5.1a). The NaCl sleeve acts as a medium for converting the uniaxial load from the WC piston to a hydrostatic load around the sample. The pyrex sleeve serves to electrically insulate the inner graphite furnace from the vessel wall. The pyrex glass and the NaCl sleeves were kept in a drying oven at 110 °C to eliminate any moisture. The sample was placed inside a ceramic sample holder made of crushable magnesium oxide (MgO) ceramic. This holder was then centered within the furnace using an additional MgO spacer. Any void space inside the sample holder was eliminated by packing extra powdered MgO around the sample. On top of the sample holder, a ceramic disk, of 1 mm in thickness, is used to isolate the thermocouple (T/C) from the sample material. Above this disk, there is a single bore ceramic spacer designed to grab the thermocouple and to prevent its extrusion. The final component of the sample assembly is a stainless steel base plug with a centered hole through which the T/C passes. The base plug is insulated from the pressure vessel by a pyrophyllite sleeve. During sample pressurization, the base plug deforms and holds the T/C to prevent it from extrusion. The sample assembly is wrapped in Pb-foil and placed inside the pressure vessel whose inner bore is coated with an MoS_2-based lubricant. Both the Pb-foil and lubricant reduce the friction at the interface between the sample assembly and the vessel wall. During an experiment, the pressure vessel is kept cool by providing continuous flow of cold water through the cooling plates placed above and below. Corrosion of the pressure vessel, the cooling plate and the bridge, as a result of being in contact with water, is reduced by application of a layer of a high temperature resistant silver paint to the exposed areas. Lastly, all experiments were performed using the hot "piston out" method where the pressure was initially raised to 10 % above the pressure of interest and held there while the sample was brought to the run temperature, and then slowly backed out.

2.1.4 Temperature control of the piston cylinder apparatus

Temperatures in the piston cylinder were controlled using a Eurotherm system consisting of a programmable controller linked to a silicon controlled rectifier. Using this system, temperatures can be maintained to within 1 °C and samples could be heated or cooled as slowly as 1 °C/hr. Experiments were quenched by shutting off the power to the furnace, which resulted in an initial quench rate of ~100 °C/s. The temperature of the sample inside the pressure vessel assembly is monitored using a 0.01" diameter tungsten-rhenium ($W_{95}Re_5$-$W_{74}Re_{26}$) thermocouple. The thermocouple (T/C) wires are supplied with a NIST-traceable calibration. Reported temperatures are not corrected for the pressure effect on output emf. In some experiments, oxidation of the thermocouple wires as a result of penetration of air through the MgO ceramic T/C holder was reduced by continuous flow of Ar-1% H_2 gas around the top of the thermocouple insulator.

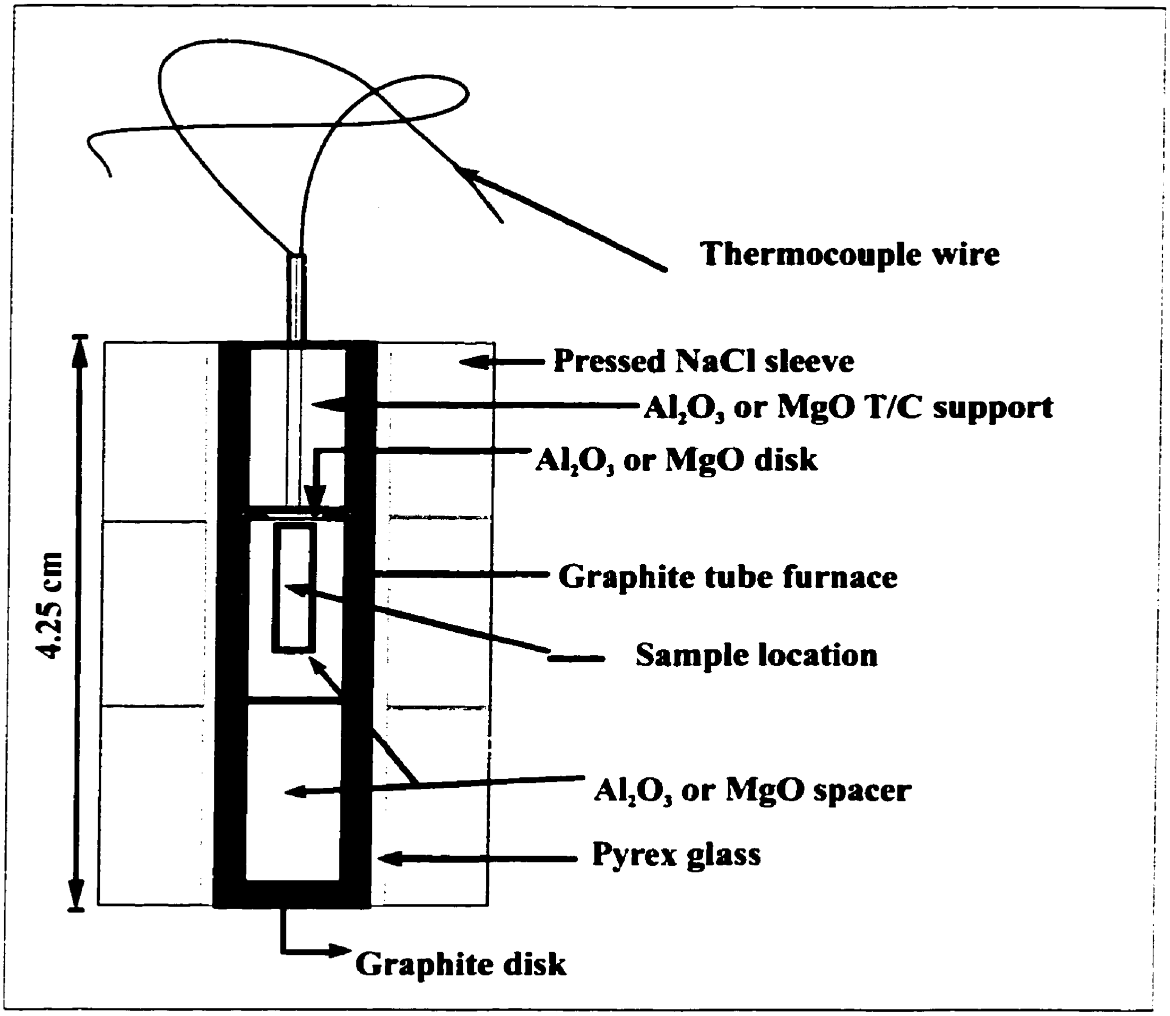

Figure 5.1a. Schematic representation of the sample assembly employed in the piston cylinder apparatus for high-pressure runs.

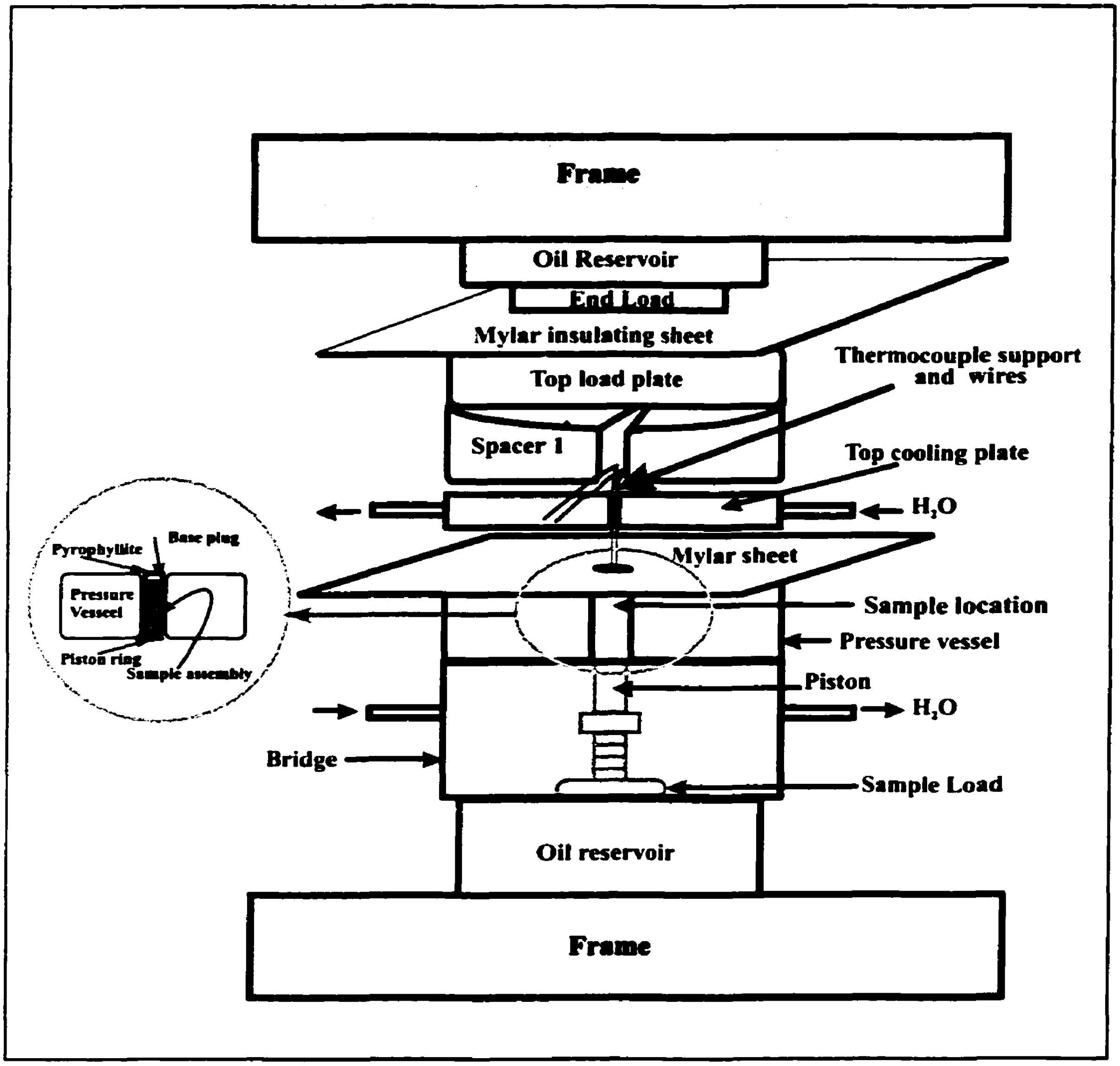

Figure 5.1b. Schematic representation of the end loaded piston cylinder apparatus used in this study. The major components shown here are not drawn to scale.

2.1.5 Liquidus temperature determination

In order to reduce the nucleation density and thereby grow a few, large chromite crystals, precise determination of the chromite liquidus temperature was required. This determination was carried out through a series of trail and error experiments in the piston cylinder apparatus at 1 GPa using a mixture of 401 basalt and immiscible Fe-Ni-sulphide melt sealed in graphite-lined Pt capsules. These experiments were initially super heated to 1460 °C for two hours, then temperature was reduced to the plausible liquidus temperature where the system sat for 2 hours and finally quenched to room temperature. A summary of these experiments is provided in Table A2-b, which were carried out at temperature increments of 10 °C from 1300 to 1400 °C. Using this approach, the liquidus temperature of our synthetic 401 basalt was determined to be at 1350 (± 5) °C.

2.1.6 Growth of chromite crystals from basaltic melt

Our goal of producing large chromite crystals in high pressure partitioning experiments was achieved by adding water to experiments and employing a specific time-temperature protocol. In comparison of both water-bearing and dry experiments we found that the presence of water promoted the growth of chromite crystals, as only a few relatively large (25-50 μm) chromites were produced in the "wet" runs, as opposed to numerous small crystals in the dry experiments. We added small amounts of water to these experiments as brucite ($Mg(OH)_2$) which was synthesized from high purity MgO and distilled water at 1.2 GPa and 700 °C for 24 hours. This synthesis procedure resulted in crystallisation of snowflake textured brucite crystals whose identity was confirmed by X-ray powder diffraction in the Department of Geology. The synthetic brucite was added to the basalt starting material to yield 1 wt % total water in the melt upon decomposition at run conditions.

In addition to the presence of water, the employment of a specific time-temperature protocol, as portrayed in Figure 6, enhanced the growth of large crystals. Each experiment consisted of four separate stages. First, samples were subject to an initial super-liquidus step at 1460 °C lasting 2 hrs (for 1 GPa experiments) to 72 hrs (for 1 atm experiments) to allow the silicate and sulphide melt or alloy mixture to interact with each other and homogenize. Samples were then rapidly cooled (50 °C/min) to the predetermined liquidus (1350 °C) to allow for nucleation of chromite crystals. The nucleation step lasted for an hour and half, after which samples were subjected to slow cooling (1 °C/hr) to promote growth of chromite. An isothermal soak step of varying duration (20 to 60 hrs) followed the growth step. Finally, samples were quenched by shutting the power to the furnace.

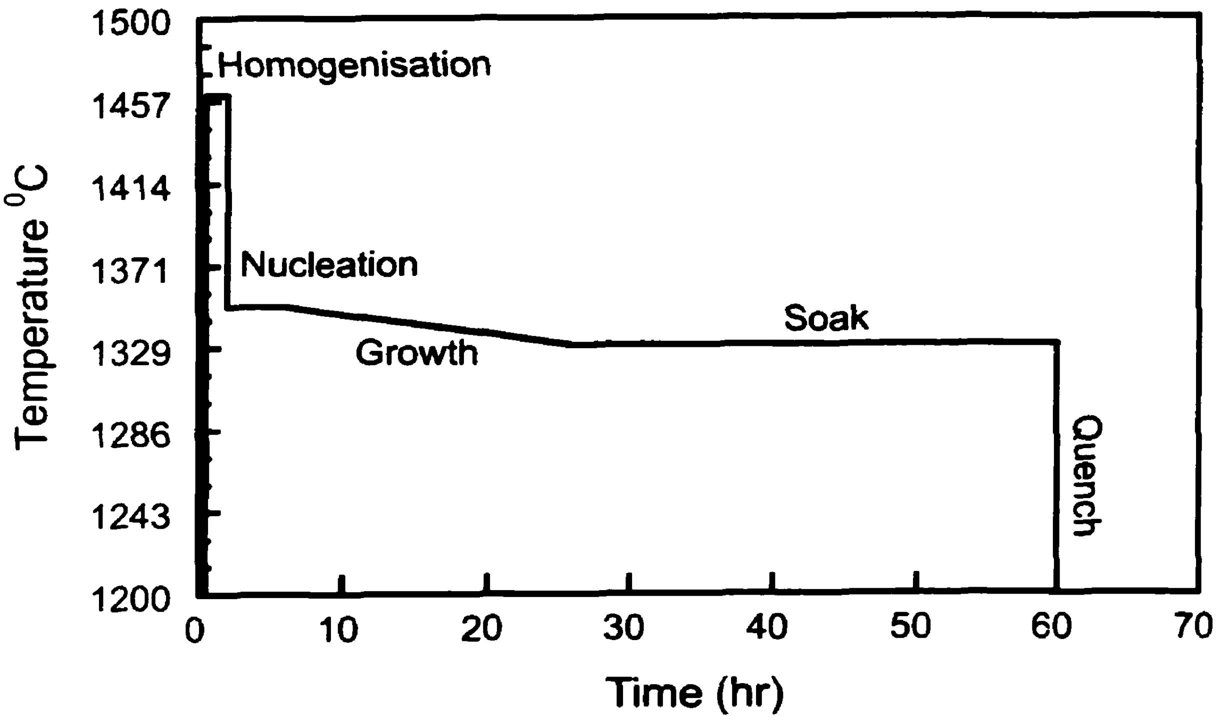

Figure 6. Time-temperature history employed for partitioning experiments (note that the duration of some steps varied somewhat between experiments). Each experiment included four steps: 1) an initial super-liquidus step to homogenise the melt, 2) a nucleation step at the predetermined chromite liquidus temperature (1350°C), 3) a growth step consisting of a 1°C/hr ramp from 1350 to 1330 °C, 4) an isothermal soak of different durations (20-60 hrs), followed by quenching.

2.1.7 Low pressure experimental protocol

Experiments at 1 atm were performed in a gas sealed vertical tube furnace utilizing the same melt composition and similar time temperature profile as employed in the high pressure runs. The temperature for these runs was monitored using a 0.015" Pt_{100}-$Pt_{90}Rh_{10}$ thermocouple that was calibrated against the melting point of gold. The super-liquidus stage for the PGE8a and PGE8b experiments were selected to be 72 hrs to promote equilibration between the silicate melt and the PGE-spike. The doped starting material was loaded into a San Carlos olivine capsule with dimensions of 7 x 4 mm and an inner diameter of 3 mm. The charges were then placed inside a ceramic sample holder suspended from the hook of a silica rod. First the sample is placed in the cool end of the vertical tube furnace. Half an hour after starting the flow of CO and CO_2 gases, the sample was gradually lowered at 5 cm every 15 minutes to ensure slow heating of the sample. The time-temperature protocol was engaged when the sample reached the predetermined hot spot. Finally, quenching of the sample was achieved by plunging the sample into a container of ice and water at the bottom of the furnace, while the gases were still flowing. Since the temperature was changing during the run (i.e. from 1460 °C to 1350 °C, and 1330 °C), the CO and CO_2 gas flows were adjusted to maintain a constant fO_2 during different stages of the experiment.

2.2 Analytical Techniques

The major and trace element compositions of the phases in run products were characterized by the electron microprobe (EMP) and LA-ICP-MS, respectively. Samples were initially sectioned by grinding with 400 and 600 grit paper, after exposing an appropriate amount of surface, samples were mounted in epoxy resin media and left under a heat lamp for 6 hrs to cure. The mounted samples were then ground with 400 and 600 grit and polished with 1 and 0.3 μm alumina powder. Samples were carbon coated since electron microprobe analysis requires a conductive surface. A carbon coat of 20 μm is optimal to prevent a charge build up due to electron bombardment (this carbon coat was removed for LA-ICP-MS analysis). Samples were also examined using a JEOL 840 scanning electron microscope (SEM), together with an energy dispersive spectrometer (EDS) in the Department of Geology, to characterize various phases in the samples, such as chromite, olivine, alloys, and sulphide globules. Backscattered electron (BSE) images from the SEM, together with reflected light digitized photomicrographs were used to identify phases and map their distribution.

2.2.1 Electron microprobe analysis

Major element analyses of run product phases were obtained using a Cameca SX 50 electron microprobe housed in the Department of Geology. All phases were analysed quantitatively by wavelength dispersive spectroscopy (WDS- analysis). In this technique, the intensities of characteristic X-ray lines produced during electron bombardment of the specimen are compared to that produced from a suitable standard using similar instrumental conditions (accelerating voltage, beam current). Table A3 (1-6) summarizes the details of the analytical conditions used in this study for each phase in the run products. Absolute concentrations are calculated from the ratios of the X-ray intensities in the unknown to that in the standard and the known concentration of element in the standard, by the following expression:

$[C]_{sample} = \{(I_x)_{sample}/(I_x)_{std}\}[C]_{std}$, I = intensity (cps), C = wt % of element, (Reed, 1996)

Background count rate contributions to peak intensities were determined at wavelength offsets from the peak position. A "PAP" correction program was used for the calculation of true concentrations which is a modified $\Phi(\rho z)$ polynomial (a depth distribution function to correct for absorption) used in the standard ZAF matrix correction algorithm, which includes corrections for atomic number (Z), absorption (A), and fluorescence (F) (Reed, 1996; Cameca SX 50 manual). To reduce the aforementioned corrections, standards were selected based on matrix similarity. For data processing, in all the phases except alloys and sulphides, points with totals higher than 101 and less than 98 wt% were discarded. Minimum detection limits were defined, where the peak minus background count rates were less than either two or three times the square root of background count rates. In some cases two analytical conditions were employed, the first at lower beam currents for major element analysis, and the second at higher current and different counting times for minor elements. This technique was used in order to ensure that the maximum count rates were within the linear range for the X-ray detectors. In addition, an overlap correction was applied for analysis of PGE alloys, since the Lα line of Rh partially interferes with Lβ line of Ru and Lα of Pd with Lβ of Rh. In this procedure, the contribution of the interfering element is measured on the pure phase and subtracted from the peak intensity of the element of interest in proportion to the abundance of interfering element in the unknown. Glass analyses were carried out with extra care, because of the migration of alkalis (Na) during electron bombardment. For this reason, the following precautions were applied: a) use of a low beam current (10 nA), b) application of a defocussed beam of 15 μm in diameter, and c) movement of the beam during the analysis of the sample and standard. Due to textural inhomogeneity of the quenched sulphide liquids, this phase was also analysed with a defocussed beam of 15 μm in diameter. Chemical homogeneity of phases in the run products was determined by multiple analyses with line scans consisting of up to 10 points in chromite and olivines along the diagonal axes of the exposed crystals and a total of 20 points on glasses along the horizontal and vertical length of the samples.

2.2.2 Trace element analysis

Trace element analyses were obtained by laser ablation microprobe-inductively coupled plasma-mass spectrometry (LA-ICP-MS) at the Department of Earth and Planetary Sciences, Harvard University. This work was carried out in collaboration with Dr. W. F. McDonough and Dr. I. Horn. The laser ablation setup has been described in detail by Horn et al. 2000. The system consists of an argon fluoride excimer laser (Compex 110, Lambda Physiks, Germany) operating at a wavelength of 193 nm. The initial rectangular laser beam is modified to produce round ablation craters by means of a set of cylindrical and spherical lenses in conjunction with aperture imaging. This produces a homogenous beam profile at the site of ablation (Horn et al., 2000). The system was designed in such a way that the optical path of the petrographic microscope used for sample imaging, is separated from the laser beam path. By this method, the sample can be viewed by either transmitted or reflected light during the ablation process. The laser pulse energies of ~ 0.1 to 2.5 mJ create spot sizes of 15->500 microns. The laser beam is focussed through a silica window onto the sample contained in an airlocked plexiglass sample cell, which operates under continuous flow of helium. The helium flow results in more efficient transmission of the ablated material from the sample cell into the inductively coupled plasma torch.

For calibration purposes, a silicate reference glass, NIST 610, doped with 61 trace elements at a level of approximately 450 ppm and Re with 49 ppm, and a Ni-sulphide in house standard (PGE76) containing ~76 ppm of all PGEs and trace levels of Re (~ 6 ppb) were selected. The standards were analysed four times, twice before and after analysis of 16 points on each sample. ICP-MS measurements were carried out using a VG plasmaquad 2 quadrupole mass spectrometer, and time resolved data acquisition achieved using factory supplied software (VG Elemental, Winsford, England), where each spot analysis consisted of a two minute acquisition time consisting of 60 s of background measurement (gas blank) followed by 60 s of sample ablation. The intensity for each element was calculated as the mean count rate during the ablation period corrected for differences in the ablation yield using a known internal standard element. ^{55}Mn, ^{49}Ti, and ^{43}Ca were used as internal standards to correct for ablation yield differences, since their concentrations in the glass, chromite, olivine and the NIST 610 standard are known. ^{59}Co and ^{61}Ni were used as internal standards to monitor the PGE concentrations using the PGE76 NiS standard. In run products containing sulphides, the Ni content of the glass was lower than the detection limits of the electron probe, thus, the calculated Ni concentrations were measured by LA-ICP-MS using NIST 610 glass as standard, which were then used to correct for ablation yield differences and calculate the PGE contents of phases using the PGE76 standard. In this study, PGE isotopes measured in glass, chromite and sulphide consist of the following: ^{61}Ni, ^{99}Ru, ^{101}Ru, ^{102} Ru, ^{103}Rh, ^{105}Pd, ^{185}Re, ^{190}Os, ^{192}Os, ^{191}Ir, ^{193}Ir, ^{195}Pt. By using the time resolved spectra, it was possible to observe the presence of any heterogeneities as expressed by intensity variations during the actual analysis. The most common heterogeneity encountered were high concentration "spikes" in PGE concentrations corresponding to micro-inclusions within various phases. Therefore, in order to determine PGE contents of inclusion-free material, each spectrum was examined individually and only areas of spectra that were more homogenous (areas with least heterogeneous domains) were integrated to calculate the trace element concentrations. The precision and detection limits of the LAM-ICP-MS are discussed in detail in Jackson et al., (1992) and Jenner et al., (1993). Table A4 presents the detection limits of PGEs and Re (ppm) for each run analysis in NIST 610 glass obtained over the course of this study. In this case, the minimum detection limit is determined based on count rates that are 2σ above background. It is important to point out that this detection limit is not constant and varies with the ablation efficiency and the pit size. The ablation yield is a measure of how a particular phase ablates in comparison to the NIST 610 glass or PGE 76 standard. This yield is dependent upon the ablation pit size and the nature of the material ablated, and thus, it will be less for the smaller pit sizes used to ablate run product phases than those used for standard analysis. Detection limits are generally lower in glass and sulphide standards since large ablation craters were produced during those measurements (85-180 μm). In contrast, the detection limits in chromites were high because of the small ablation spots, which were in the range of 15 to 20 μm.

CHAPTER III: RESULTS OF EXPERIMENTS

3.1 Textural observation of run products

Samples from run products were examined with reflected light and scanning electron microscopy (SEM). All phases were characterized and their distribution mapped using either backscattered electron images or digitized reflected light photomicrographs. Table A2.d provides a summary of the phases present in each run product. Textural relationships between phases in experiments for 1 GPa and 1 atm conditions are described separately in the following section.

3.1.1 Run products at 1 GPa

Experimental run products consisted of some combination of chromite, quenched basaltic melt, sulphide liquid and alloys. Figure 7.a portrays representative phases and their ablation pits in experiment PGE2b, which are also common to the other high and low-pressure runs. The chromites are subhedral and range from 20 to 60 μm in diameter. Chromite crystallisation is the result of heterogeneous nucleation as this phase frequently used the wall of the graphite capsule or the sulphide-silicate liquid interface to nucleate (Fig. 7.b-7.d). Although in some cases chromite nucleation density was high, the equant shapes of the crystals suggest that growth was controlled by interface processes, which is a consequence of the slow growth rate established by a cooling rate of 1 °C/hr from temperatures of 1350 to 1320 °C. Chromite crystals frequently contain inclusions of sulphide-melt and alloys (Fig. 7.a and 7.c), which is a consequence of entrapment of these phases during chromite crystallisation. Run product-glasses are free of quenched crystals, but do contain dilation cracks produced during sample decompression (Fig.7.a, c and d). Quenched sulphide liquids form circular globules ranging from 80 to 300 µm in diameter and commonly they adhere to the wall of the graphite capsule (Fig. 7.a, e and f), and/or to chromite crystals. Sulphide globules display a fine to coarse heterogeneous texture defined by the presence of quenched mono-sulphide solid solution (mss), and pentlandite. Fe-PGE alloys are dispersed throughout the sulphide globules, which indicate their late exsolution as the sulphide liquid crystallised (Fig. 7.e). In IPRe4 and PGE5a, stable Fe-Re-Ir alloy phases were present as a consequence of the high Re and Ir concentrations in the initial sulphide melt (>1 wt %) (Fig. 7.f). In experiments PGECo and PGECoS, Re-PGE-Fe-Co alloys are present and consist of clusters of rectangular crystals and aggregates immersed in anhedral crystals of Fe-Co alloy (Fig. 7.g).

3.1.2 Run products at 1 atm

Run products from 1 atm experiments consisted of chromite, basaltic glass, and newly crystallised olivine. In comparison to high-pressure runs, chromites seem to develop perfect euhedral habits, which suggest ideal conditions for their growth. In addition, the chromite crystals display sharp edges in 1 atm runs (Fig. 7.h) in comparison with the observed rounded edges in samples produced at 1 GPa. Chromites produced at 1 atm ranged from 40 to 70 microns in diameter. Since olivine capsules were utilized in these experiments, new olivines precipitated from the capsule and ranged in size from 50 to 180 µm as shown in Fig. 7.i. Basaltic glasses were texturally uniform and showed no evidence for quench crystallisation (Fig. 7.i).

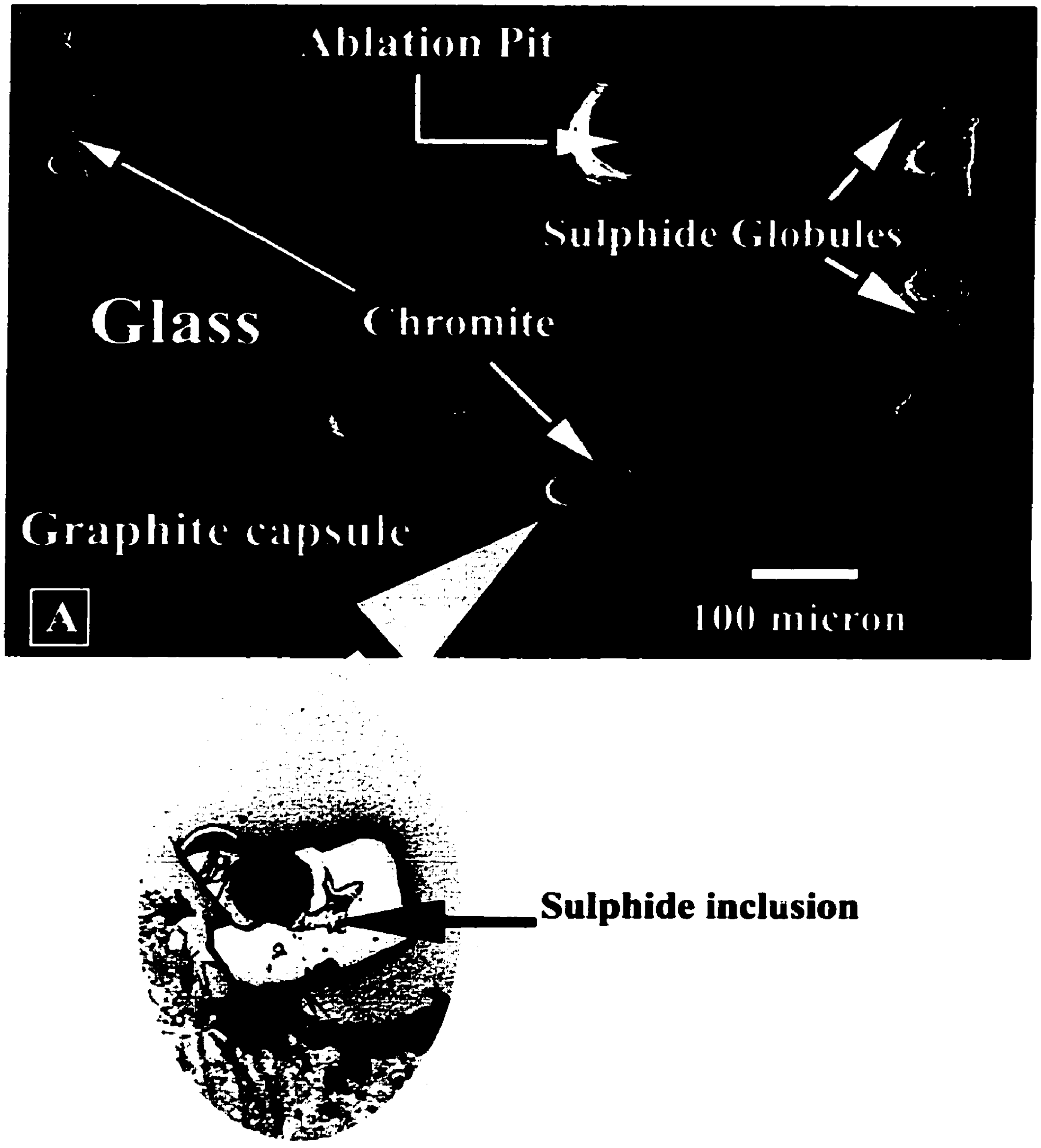

Figure 7.a. Backscattered electron (BSE) image of the run product from experiment PGE2b showing all the phases produced at 1 GPa and 1330°C. Subhedral chromite crystals consist of sulphide inclusions as shown. The sulphide globules adhered to the wall of the graphite capsule. This microphotograph also displays the ablation pits as a result of LA-ICP-MS analysis in all the phases produced.

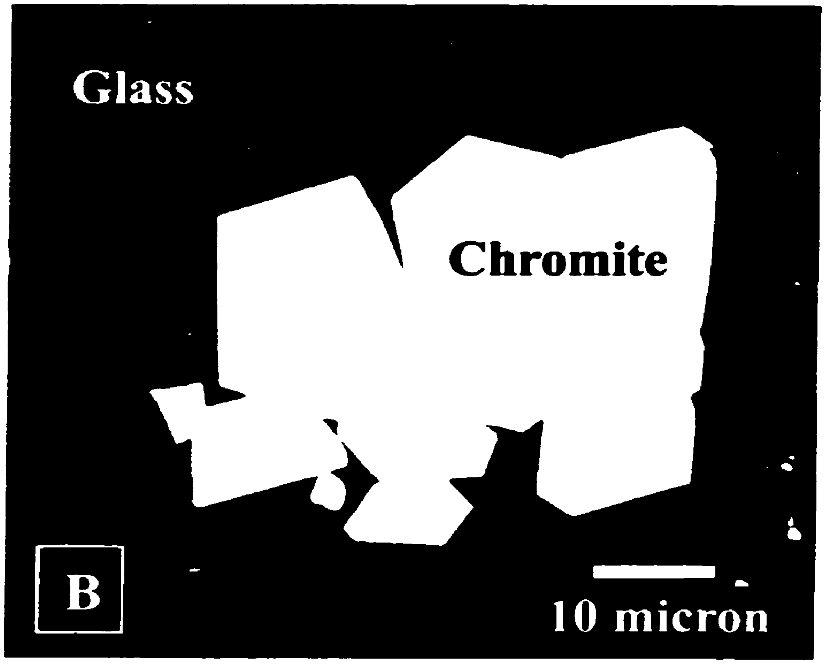

Figure 7.1b. BSE image of a subhedral chromite crystal in the run product of PGECo-experiment, which was saturated in Re-PGEs-Co alloy.

Figure 7.1c. Digitized reflected light photomicrograph of a subhedral chromite that has nucleated around a sulphide liquid globule (experiment PGE2b). The starting sulphide melt composition was doped with 1000 ppm Re, and PGEs.

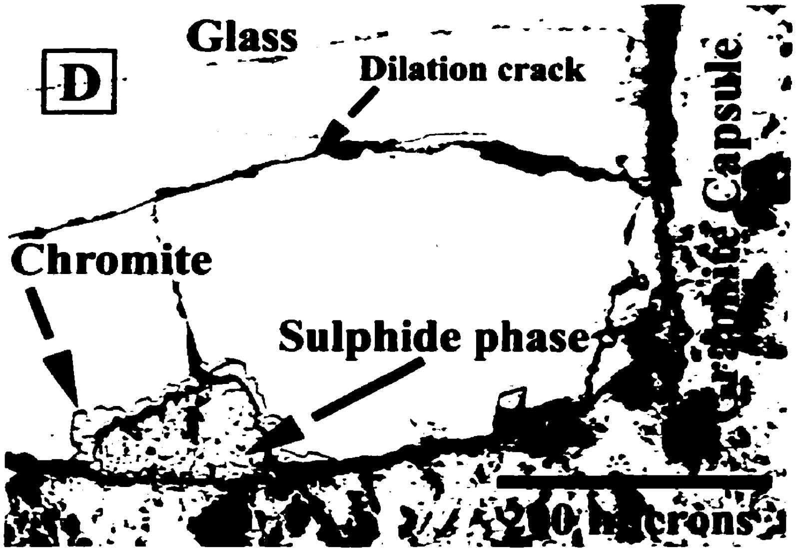

Figure 7.1d. Digitized reflected light photomicrograph of the run product from PGE1d (not sealed in Pt-capsule). The sulphide liquid in this run was initially doped with 500 ppm of Re and PGEs. As it is shown, the chromite grains display preferred nucleation at the sulfide/silicate melt interface.

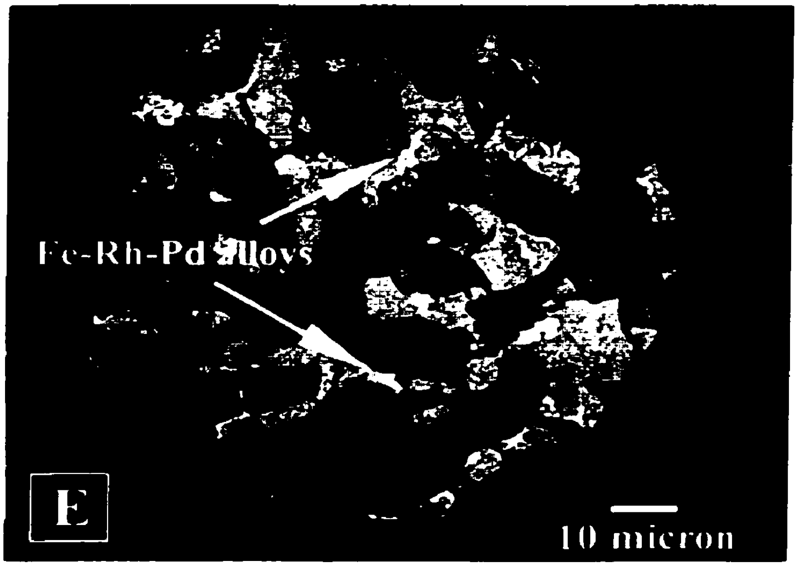

Figure 7.1e. BSE image of a sulphide globule in the PGE1d experiment showing the quench texture observed in this phase. It also displays the presence of scattered Fe-PGE alloys in sulphide liquid.

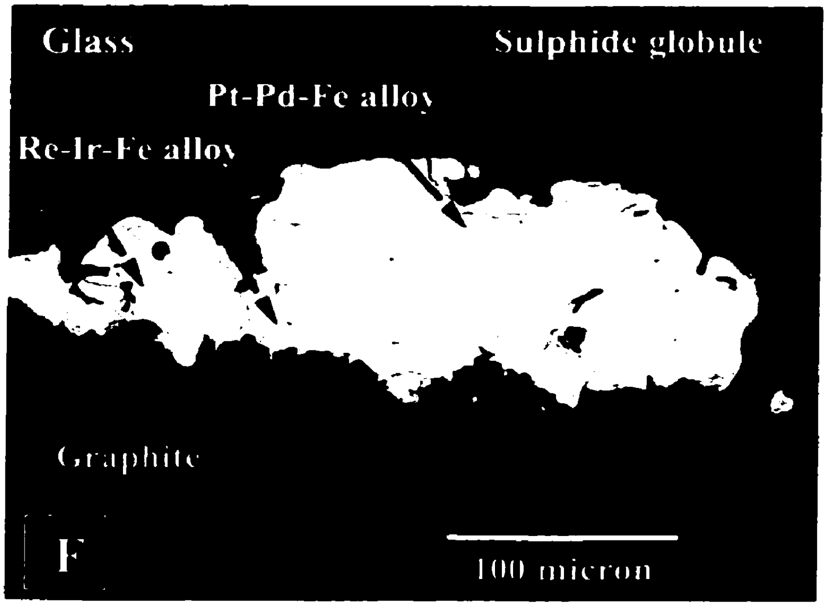

Figure 7.f. BSE image of the run product from experiment PGE5a displaying the sulphide liquid globule that adhered to the all of the graphite capsule. The sulphide melt was initially doped with 5 wt% of Re, Pd and Ir, which resulted in the formation of stable Fe-PGEs alloys as shown above.

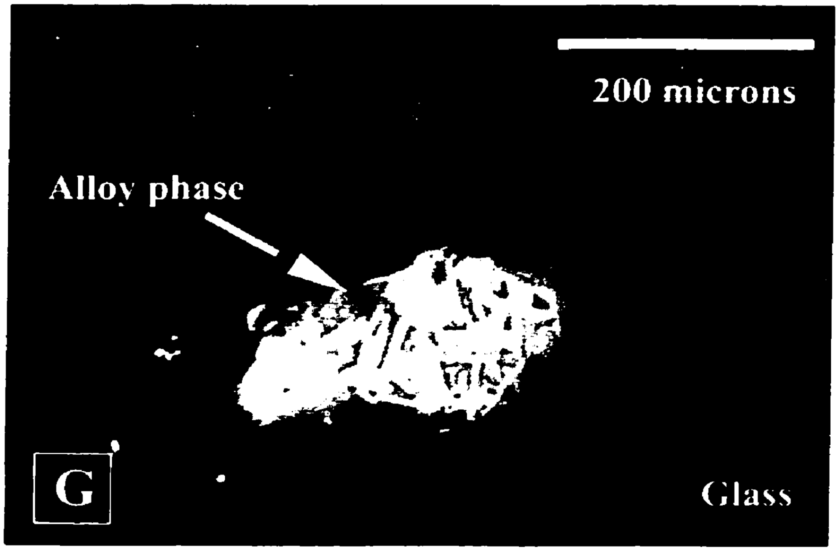

Figure 7.g. Digitized reflected light photomicrograph of the alloy phase from experiment PGECo, which was analysed by EMP (Table A5.6). Two distinct habits of Re-PGE bearing alloy, the euhedral crystals, which are rich in Re and PGEs and an anhedral alloy mass that contains higher Co, Fe and Rh than the euhedral grains.

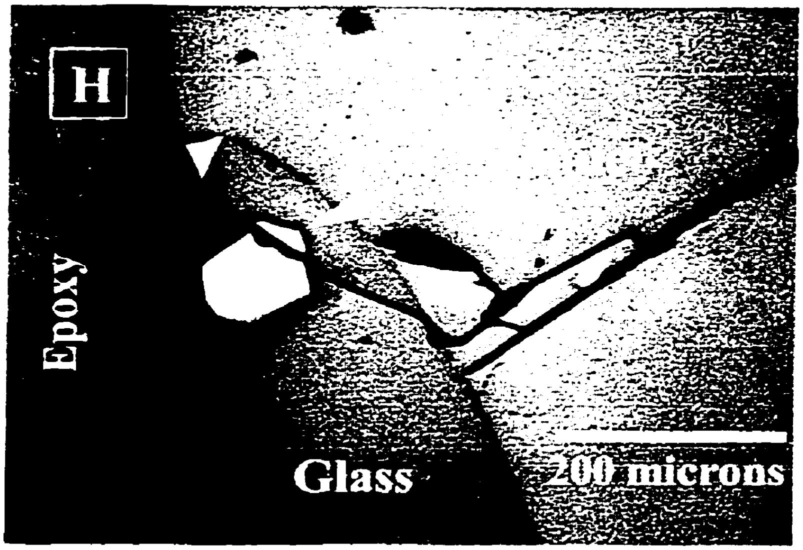

Figure 7.h. Digitized reflected light photomicrograph of a euhedral chromite grain, that crystallised at 1 atm, and 1330 °C in experiment PGE8a, which was doped with a stock solution consisting of ppb levels of Rh, Pd, and Os (Table A2-a). The perfect habit of the chromites in this run suggests a suitable conditions for their growth in the absence of sulphide/alloy phases.

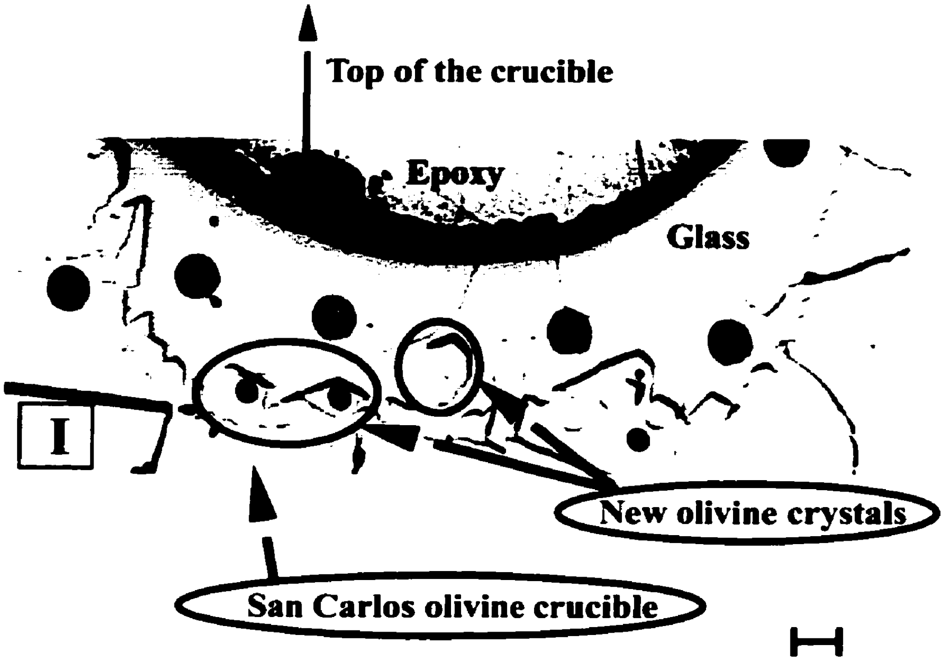

Figure 7.i. Digitized reflected light photomicrograph of a cross section of the charge from the PGE8a-experiment portraying the new sub-euhedral olivine crystals, basaltic glass, and the ablation pits of LA-ICP-MS. The ablation pits are about 170 μm for glass, and 60-85 μm for olivines.

3.2 Major element compositions

3.2.1 Estimation of oxygen fugacity based on Cr solubility in melt

The final oxygen fugacity of the sample is estimated from the Cr-solubility in the basaltic melt, since the solubility of Cr is sensitive to oxygen fugacity and temperature of the system (Roeder and Reynolds, 1991; Murck and Campbell, 1986). The amount of chromium dissolved in a chromite-saturated silicate melt decreases in response to increased fO_2 and decreased temperature. Therefore, in this study, due to the lack of information regarding the final Fe^{+3}/Fe^{2+} ratio of the melt, the fO_2 is calibrated based on a compilation of Cr solubility of 401 basalt (similar to melt composition used by Roeder and Reynolds, 1991 and Murck and Campbell, 1986) at different fO_2 and temperature. Figure 8 portrays the compilation of total Cr solubility as Cr_2O_3 wt% in 401-melt against oxygen fugacity at different temperatures. Only the run product from PGE5a-experiment shows an anomalously high fO_2, which may be a result of low temperature caused by thermocouple (T/C) contamination as evidenced by low output power and the presence of clino-pyroxene in the run product.

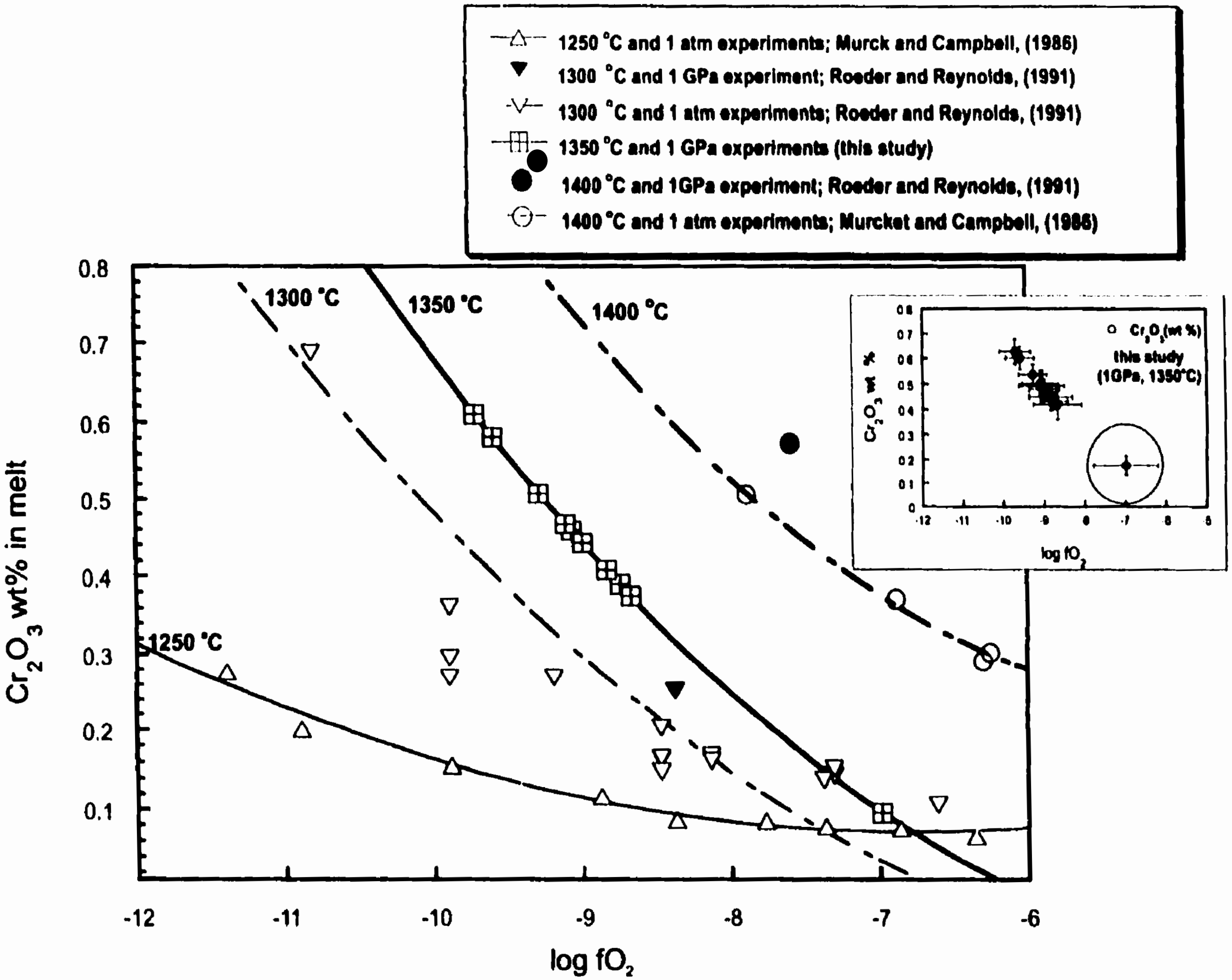

Figure 8. Plot of estimated fO_2 based on the Cr-solubility in basaltic melt, showing the variation in Cr concentration in response to changes in fO_2 and temperature. The result of calibrated fO_2 in this study is explicitly shown on the top right corner, where the error bars indicate 1 σ error of the multiple point analyses. The point shown in open circle displays the run where the low dissolved Cr is suspected to be the result of lowered temperature (i.e. T/C contamination).

3.2.2 Major element chemistry of the run product phases

The major element compositions of the phases produced in partitioning experiments are summarized in Table A5.1-A5.6. Chromites crystallised in these experiments are rich in Cr, with Cr-number [100Cr/(Cr+Al+Fe^{3+})] ranging from 64 to 72 and Mg-number [100Mg/(Mg + Fe)] ranging from 49 to 54. Recalculation of chromite analyses, assuming an ideal spinel stoichiometry, AB_2O_4. is provided in appendix Table AI-a. Figure 9 depicts the major element compositions of naturally occurring chromites in comparison to the chromite of our study. Our synthetic chromites fall within the range of compositions from different igneous settings such as ophiolites, alpine peridotites, and layered intrusions. The chromites in this study show no major element zonation from rim to core and Figure 10 portrays a representative concentration profile measured by EMPA of a 60 µm chromite grain from experiment PGECo, in which the homogeneity of chromite is confirmed. Figure 11 presents the variation of major oxides in chromites as a function of oxygen fugacity. The Fe^{3+} content of chromites is sensitive to variation in fO_2, where it decreases under reducing conditions at the expense of Cr^{3+} in chromite structure, which is consistent with work of Roeder and Reynolds (1991).

Clino-pyroxene was crystallised in the run product from the experiment PGE5a due to a probable decrease in temperature as a result of possible T/C contamination. The clino-pyroxene analyses did not show zoning across the grain in terms of major elements.

Olivines were only produced in experiments PGE8a and PGE8b, since San Carlos olivine crucibles were used to encapsulate those samples. The Mg number of these crystals is 88 and the recalculation of their analyses is summarized in appendix Table AII-b.

Olivine-basalt melt equilibrium can be examined by two methods: a) the molar FeO to MgO ratio for coexisting olivine and melt which should be 0.3 (± 0.02) and is a temperature independent quantity (Roeder and Emslie, 1970), and b) calcium partitioning between olivine and silicate melt, which is a function of $(CaO)_{melt}$ and the amount of ferrous iron in the olivine crystal (Jurewicz and Watson, 1988). The molar ratio of FeO (assuming all Fe as FeO_{melt} in the calculation) to MgO for coexisting olivine and silicate melt, in our experiments is ~ 0.274-0.28, which is consistent with the reported K_d of 0.3 (Roeder and Emslie, 1970). For the second criteria, an empirical expression was employed which describes the K_d for Ca and the forsterite content of the olivine crystal: $K_d^{CaO}{}_{(normalised)} = \{K_d - 0.0008\ (\%Fo - 90)\}$, where $K_d^{CaO}{}_{(normalised)}$ is the weight ratio partition coefficient of a standard olivine containing 90 mole% forsterite (Jurewicz and Watson, 1988). The normalised measured K_d's of Ca for olivines in PGE8a and PGE8b are in the range of 0.025 (±0.001) which is in agreement with the best fit value of 0.021 reported by Jurewicz and Watson (1988) for melts with less than 8 wt% CaO.

In the sulphide bearing runs, all glasses were sulphide-saturated inasmuch as, they contained at least 2-4 exposed sulphide globules. Figure 12 portrays the sulphide liquid compositions synthesized in this study in terms of atomic percentages of sulphur + oxygen, iron and nickel in comparison to those determined in other studies (note that copper is also present in natural sulphide liquids, which was added to Ni in this compilation). The sulphur content of sulphide melts ranged from 27 to 34 wt%, whereas the starting material contained 30 wt % sulphur owing to the loss of metal (Fe, Ni, and PGEs) to silicate or chromite and thus increasing the mass of sulphur. Final liquid compositions have metal/anion ratios that project along the trend exhibited by the natural sulphide liquids.

The alloy produced in PGECO experiment consisted of a mixture of what appears to be euhedral alloys immersed in an anhedral alloy and the composition of each was determined by EMPA, which are provided in Table A5-6. The euhedral phases contain higher concentrations of Ru, Pd, Re, Os and Ir than the anhedral phases, which are richer in Fe, Co, and Rh contents.

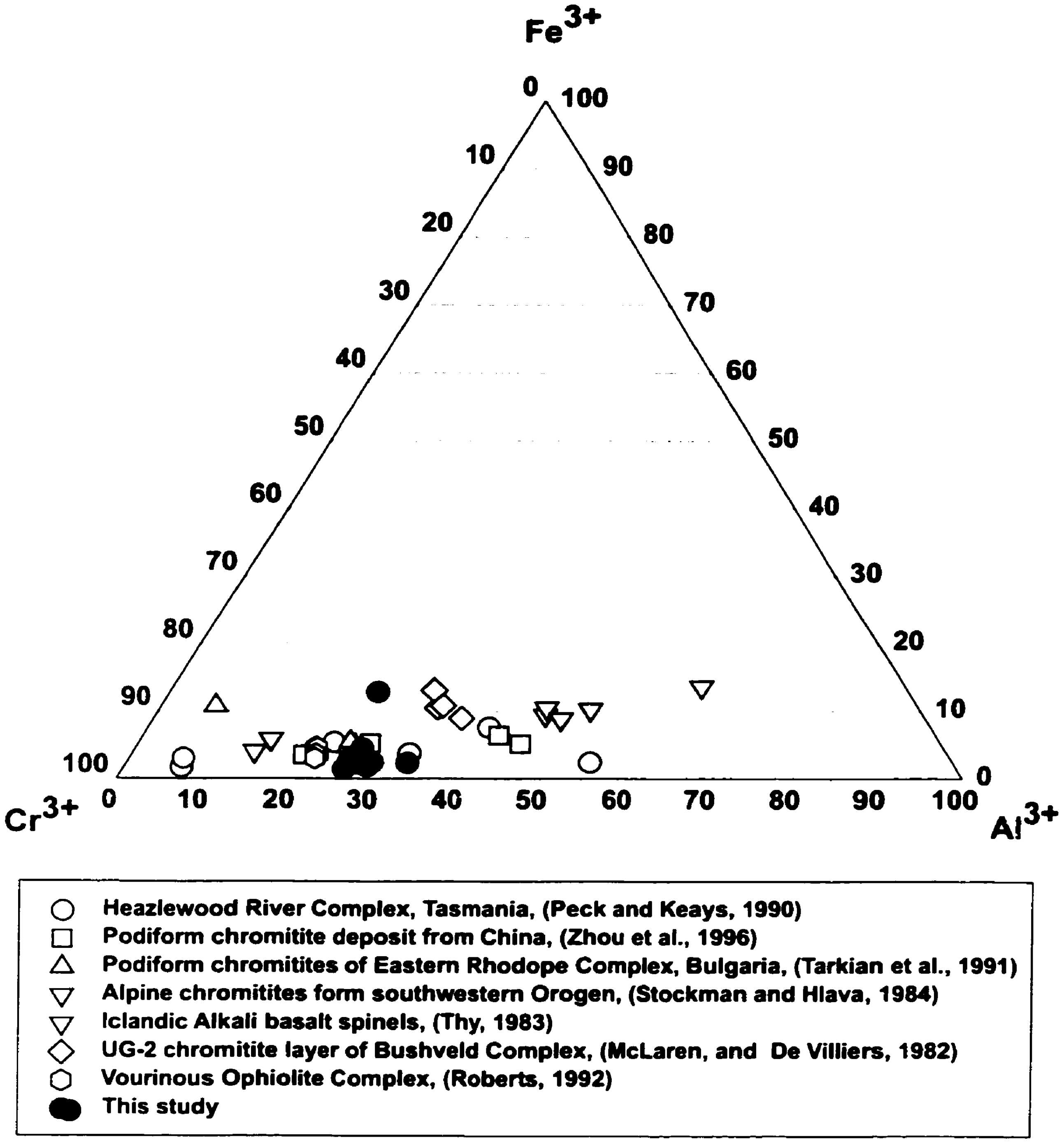

Figure 9. Ternary plot depicting the chromite compositions synthesized in this study in comparison to naturally occurring chromite from different geological settings.

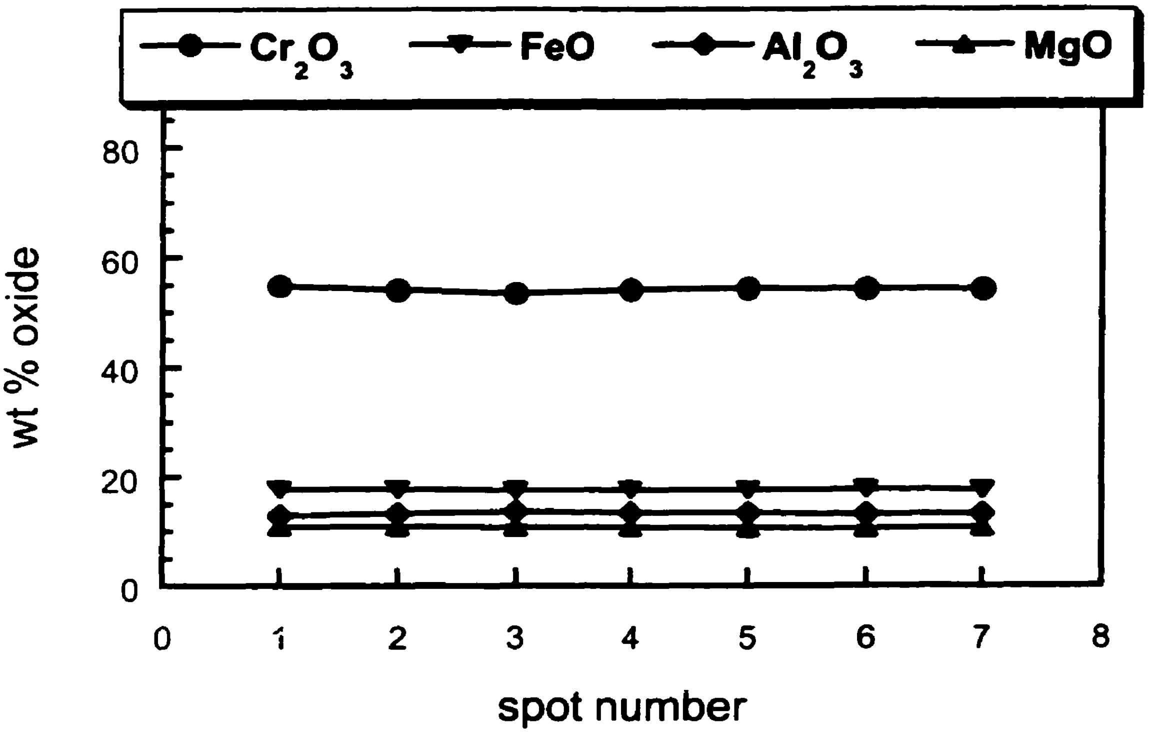

Figure 10. Major element concentration profile measured by EMPA across a 60 micron diameter chromite from PGECo run product. The points are approximately equally spaced. There is no zonation across the grain in terms of major elements, consistent with chromite/melt equilibrium.

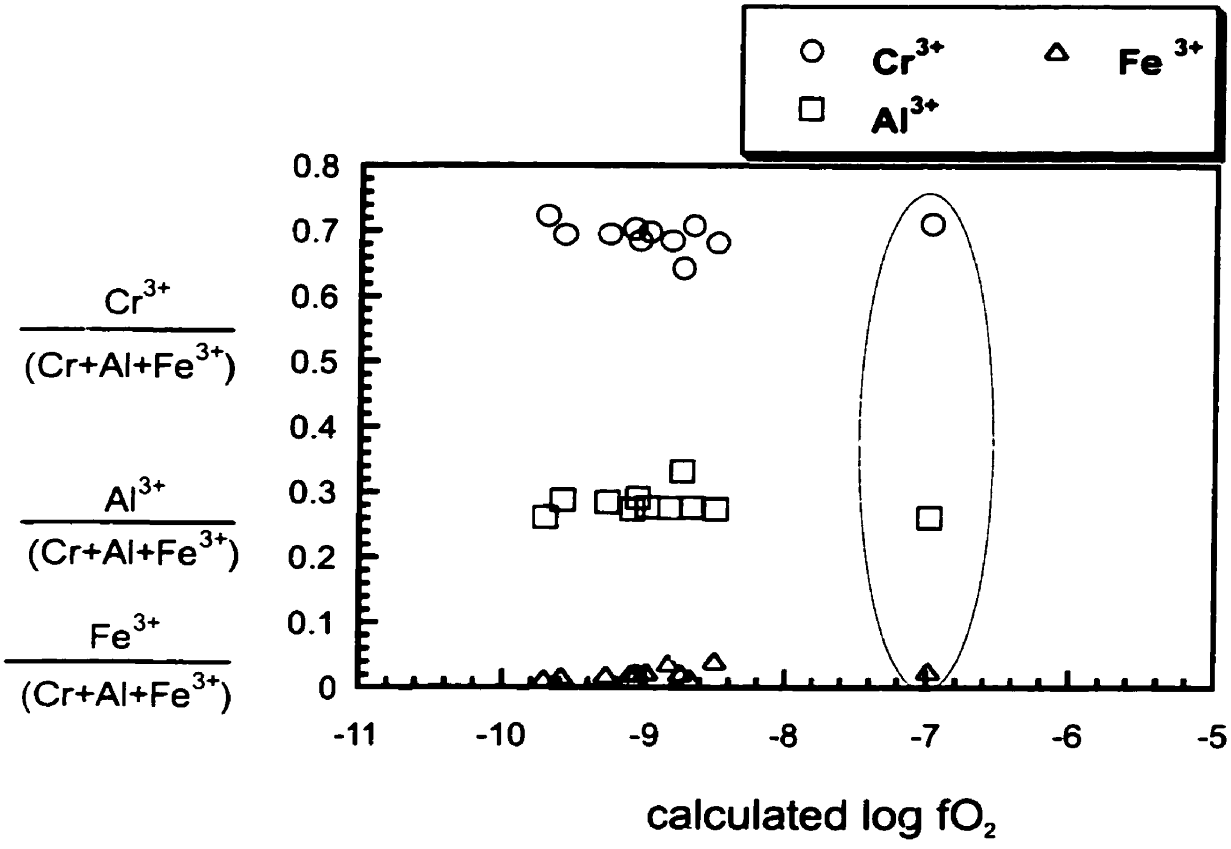

Figure 11. Plot of $Cr^{3+}/(Cr^{3+}+Fe^{3+}+Al^{3+})$, $Al^{3+}/(Cr^{3+}+Fe^{3+}+Al^{3+})$,and $Fe^{3+}/(Cr^{3+}+Fe^{3+}+Al^{3+})$ in run product chromites vs. Calculated oxygen fugacity. The Fe^{3+} content of the chromite increases at the expense of Cr^{3+} with increasing oxygen fugacity , which is consistent with the work of Roeder et al., (1991). The data points in the open ellipse are from PGE5a experiment that had possible T/C contamination.

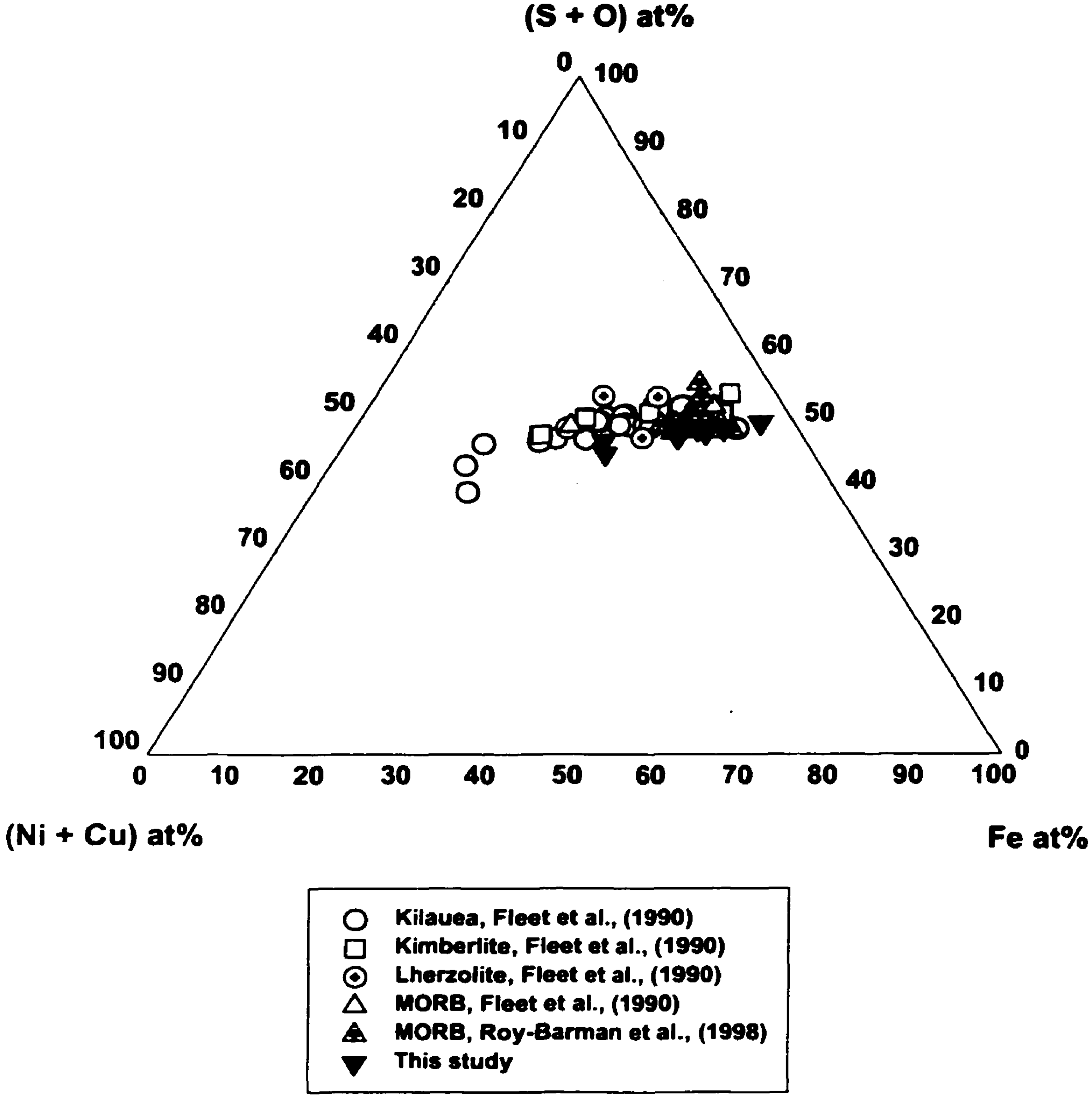

Figure 12. Ternary plot depicting natural sulphide melt composition in comparison with the synthetic sulphide melts of this study. The final sulphide melt compositions in this study show a similar range of compositions as that exhibited by naturally occurring sulphide liquids.

3.3 Trace element chemistry

3.3.1 Trace element analyses of phases produced in the run products

Table A6 (1-3) summarizes the trace element composition of the phases produced in partitioning experiments. For glass analysis, a minimum of 3 points were collected as shown in Table 6.1-6.4. The concentrations in the glass are the average of several points with the cleanest spectra and the errors are 1σ standard deviations from the mean. The minimum detection levels vary among runs since ablation pit sizes ranged from 170- 180 μm and also run products were analysed over the course of time and thus, the detection efficiency of the ICP-MS varied somewhat. Among all the trace elements, Ni and Re were the only ones with consistently high concentrations in the glass of run products with or with out sulphide melt. All PGEs are less than minimum detection limit in glass (Table A6-1) except in the runs containing PGE-Co alloy phases (PGECo, PGECoS) where Ru, Rh, Pd, and Os and iPRe4 run product where Pd, and Ir were detectable. For this reason, we plotted only Re against our calibrated fO_2 based on Cr solubility in the melt as shown in Figure.13, in order to compare run products with each other. In this plot, the Re concentration in melt clearly distinguishes the runs in presence of a sulphide phase from those in absence of sulphide liquid. All glasses from 1 atm experiments (PGE8a, PGE8b) resulted in concentrations below detection limits of LA-ICP-MS (Table A6.1). The low levels of Os, Ru, Rh, and Pd species in glasses from PGE8a and PGE8b, may be due to high backgrounds during analysis, or possible evaporation of these species over the course of the experiment, as they are known to be somewhat volatile.

The quantity and quality of the chromite analyses was limited by their relatively small sizes (25 to 60 μm), their nucleation preference for the graphite capsule wall or alloy/sulphide phases and the presence of inclusions. Thus, with these limitations, the ablation pit sizes ranged from 15 to 25 μm in diameter depending on the size of the chromite of interest, which in turn resulted in higher minimum detection limits (Table A6.2) for chromite than glass as described in the analytical section. Among these few points, only portions of spectra showing the least contamination (i.e. inclusion phases) were employed in the determination of the Re and PGE concentrations.

Olivines in PGE8a and PGE8b experiments were also analysed with ablation pit sizes ranging from 85 to 100 μm in diameter, and all PGEs and Re were below minimum detection limits (Table A6.2).

In sulphides, all elements were above detection limits. Ablation pit sizes of 85 to 100 μm in diameter were chosen since the sulphide globules varied from 85 to 300 microns in size. Those areas of sulphides that consisted of alloy crystals were avoided during the analysis in order to achieve the trace metal contents of the sulphide phase itself. As shown in Table A6.3, Pt concentrations in sulphide phases ranged from 46 to 821 ppm, where the high values are the result of contamination from the outer Pt-crucible in the high pressure runs (as a consequence of the vapour transfer through the graphite or diking). Thus, those experiments with Pt concentrations above 500 ppm in sulphide phases were not included in the database of this study. All reported concentrations are the average of 3 to 6 points and the errors represent 1 σ standard deviation of the mean.

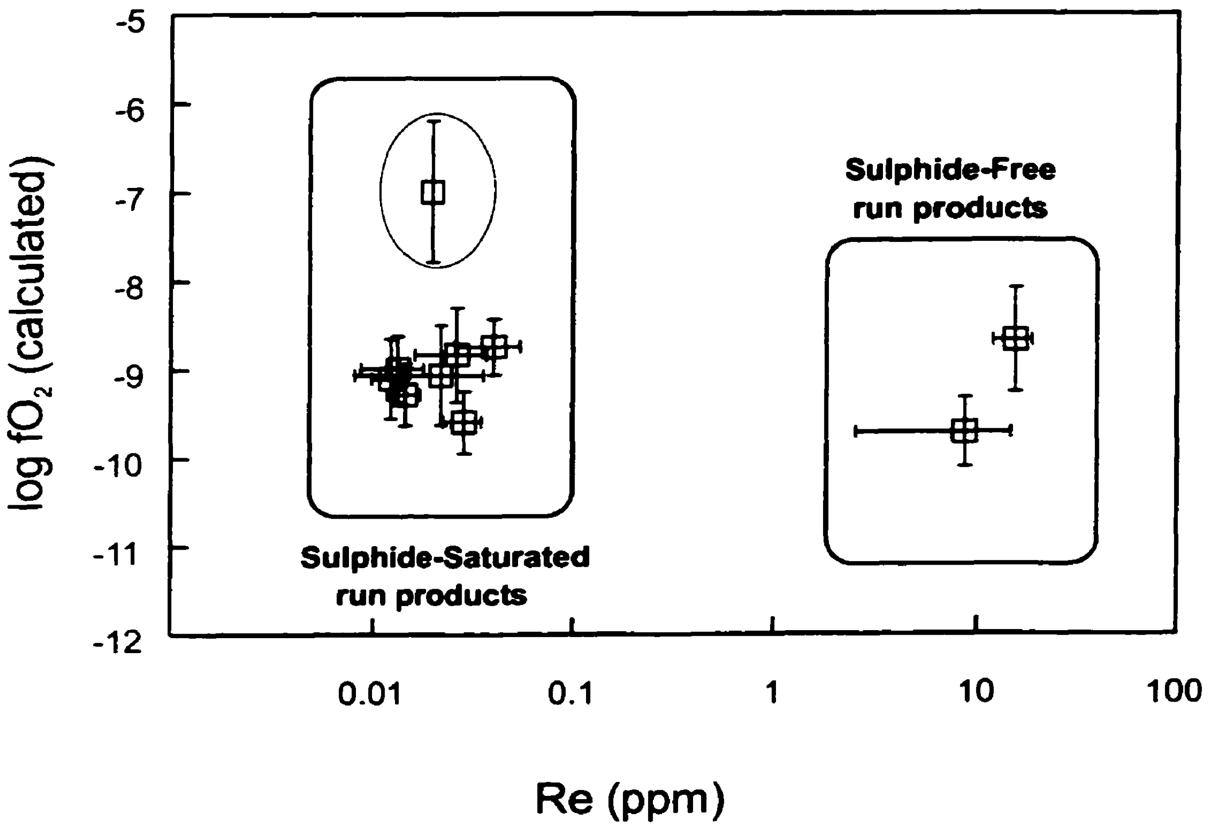

Figure 13. Plot of calculated fO_2 based on the Cr solubility in the melt against the Re abundance in the glass run products from all the high-pressure experiments. This plot portrays the variation in Re concentrations in the glasses of both sulphide bearing and sulphide-free systems, where both are alloy saturated. The open circle shows the Re concentration from the PGE5a-experiment that is lower than detection limit. In this run, the anomalous calculated fO_2 is probably the result of T/C contamination during the experiment.

3.3.2 Trace element heterogeneity in analysed phases

By employing the LA-ICP-MS analytical technique, it is possible to distinguish two levels of trace element heterogeneity in run product phases: from the macro-scale in between points in the whole charge to the micro-scale levels as observed during a single laser pulse using the time resolved analysis data acquisition software. Each case is dealt with separately below. Figure 14 (1-4) presents plots of intensities against time spectra for chromite, olivine, and glass phases, which display micro-scale heterogeneity of these elements. Figure 14.1 presents the spectra in a chromite grain in the run product from PGECo for Re and Rh as representative elements. Small inclusions are detected by spikes (ie. sudden surges) in the intensities as shown for ^{103}Rh and ^{185}Re. Only, the first 15 seconds of the spectra is employed in the calculation of PGEs and Re concentrations, since the laser beam drilled through the glass phase as evidenced by decreased intensity in the ^{49}Ti isotope. Figure 14.2 represents the spectra for olivine in PGE8a. This experiment contained 0.314 wt% Ni and 100-500 ppb PGEs (i.e. Rh, Pd, Os) in the starting material. The ^{61}Ni isotope shows a constant intensity (in terms of any spikes) indicating homogeneous Ni in the olivine whereas PGEs exhibit heterogeneous intensities at background levels. The PGE concentrations are measured to be less than minimum detection limits for this point, which are 100 ppb for Rh, 870 ppb for Pd and 40 ppb for Os.

Figure 14.3 and 14.4 portray the spectra for a glass from experiment PGECo for two points close to each other in the charge. The analysis of the point in Figure 14.3 yielded 6 ppm Re, 2 ppm Rh, and less than 20 ppb Ir, whereas the point shown in Fig. 14.4, resulted in 21 ppm Re, 6 ppm Rh, and 800 ppb Ir, illustrating heterogeneity on a macroscopic scale. This heterogeneity over the entire sample is portrayed in Figure 15 (1-3), which represents plots of the trace element contents of glasses coexisting with sulphide and alloy (IPRe4, PGECo, PGECoS). The experimental conditions for these run products are similar (1 GPa, and final temperature of 1330 °C) with the exception of run duration, which varied from 20 hrs for PGECo and PGECoS to 48 hours in IPRe4 (Table A2-c). Further more, the IPRe4 experiment was sulphide saturated whereas the other two were sulphur poor and sulphide-free, respectively. The range in concentration is more apparent in the PGECo experiment owing to the numerous analysed points and also the generally higher detectable trace element concentrations in this sample. Comparison of the three trace element concentration "profiles" indicates similar Pd levels in both sulphide-bearing and sulphide free run products, but higher Rh, and Re concentrations in sulphide-free experiments by a factor of 10^3, which clearly shows the main influence of immiscible sulphide melt for these elements. The micro-scale heterogeneity may be the result of the presence of minute inclusions "nuggets" in the glasses and crystals, whereas the macro-scale heterogeneity may be the consequence of slow equilibration between the silicate melt and alloys. This observed heterogeneity is in good agreement with the work of Ertel and coworkers (1999), whose results showed the variable levels of Rh and Pt in haplobasaltic glasses at fO_2's of less than 10^{-5}, 1300 °C and 1 atm.

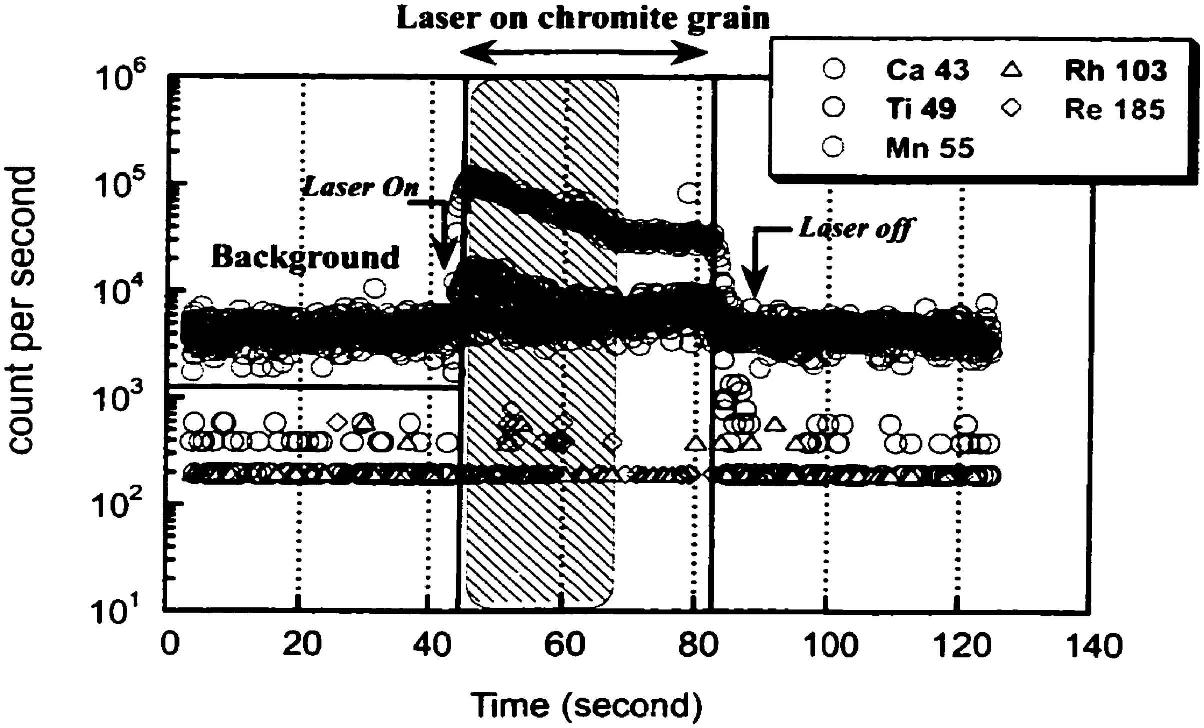

Figure 14.1. Intensity vs. time spectrum for a chromite from experiment PGECo. The shaded area is used for calculation of trace element concentrations. After 15 seconds of analysis, the laser beam drilled through the glass phase, as the signals for Ca, Mn, and Ti abruptly change. Also note that there are minute inclusions in the chromite as represented by spikes in the Re spectrum, which otherwise is close to background levels.

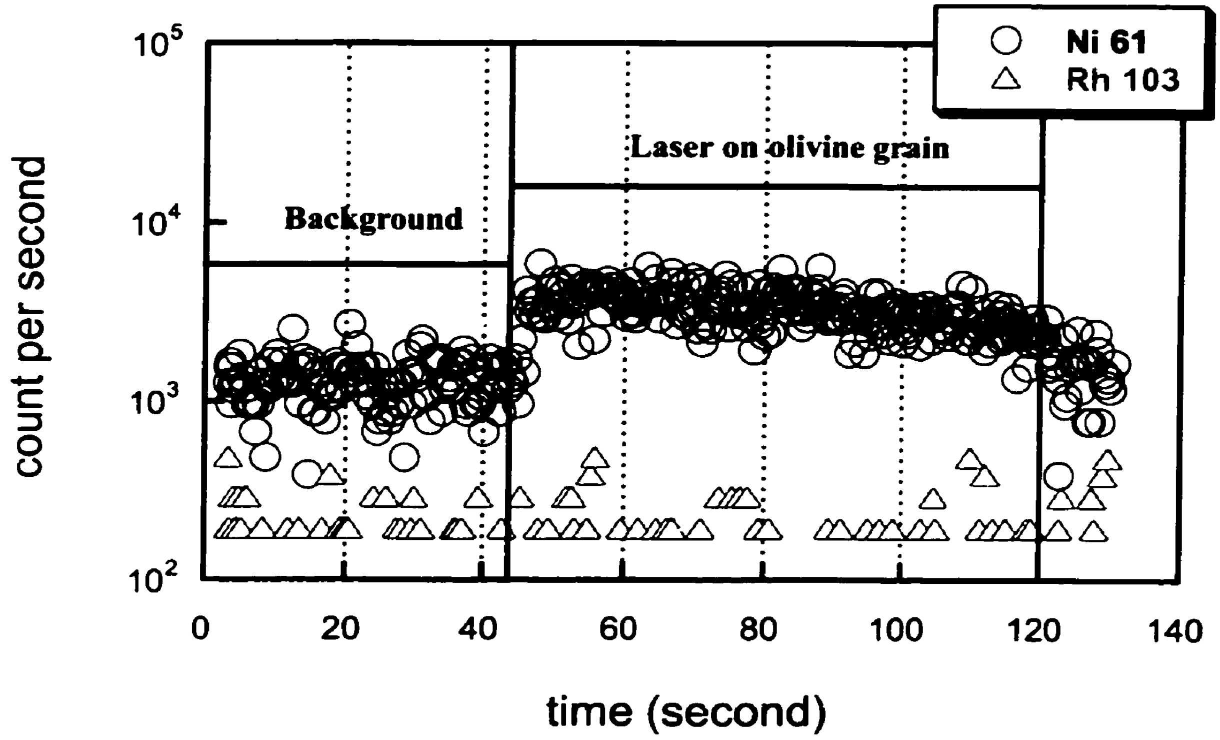

Figure 14. 2. Intensity vs. time spectrum from experiment PGE8a. Rh is at background levels and is thus below detection. Ni is present at 0.3 wt% and shows a homogeneous profile during the ablation process.

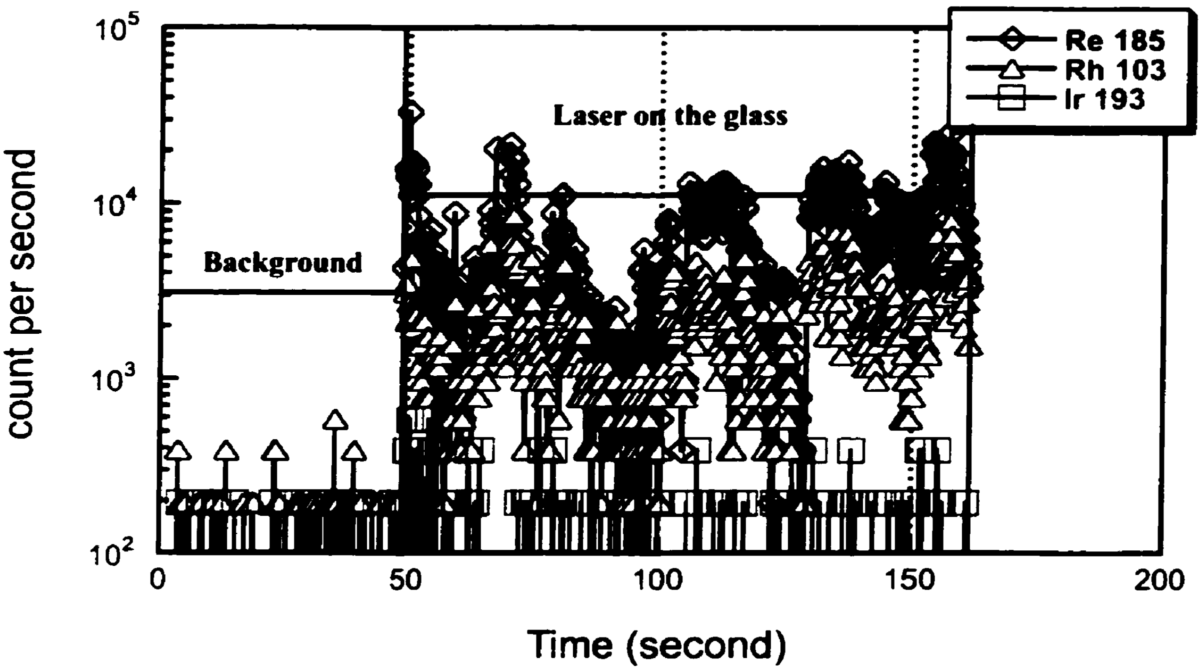

Figure 14.3. Intensity vs. time spectrum from experiment PGECo. The spectrum depicts heterogeneities in Rh, Re, and Ir concentrations during the ablation using a spot size of 170 micron in diameter over 60 seconds. Re and Rh in this analysis are at 6 and 2 ppm, respectively and Ir is less than the minimum detection limit of 20 ppb.

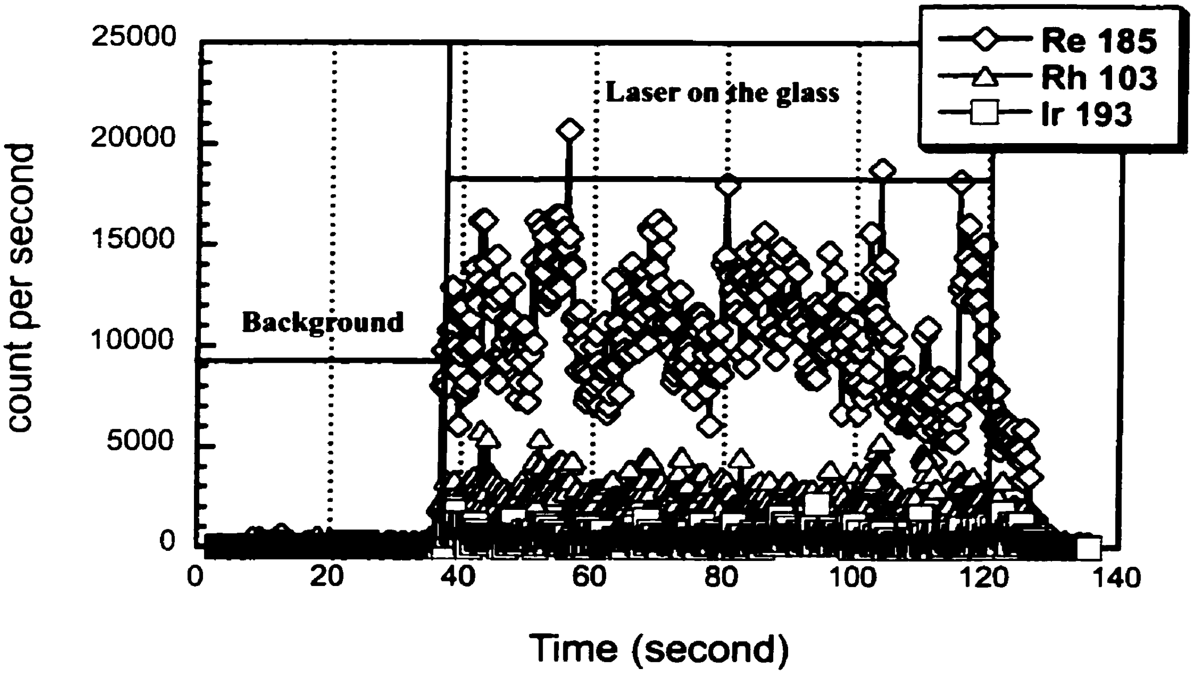

Figure 14.4. Intensity vs. time spectrum from experiment PGECo. The spectra shows a more homogeneous level of Rh, Re and Ir during the ablation process with Re and Rh at 21 and 6 ppm, respectively and Ir at 800 ppb.

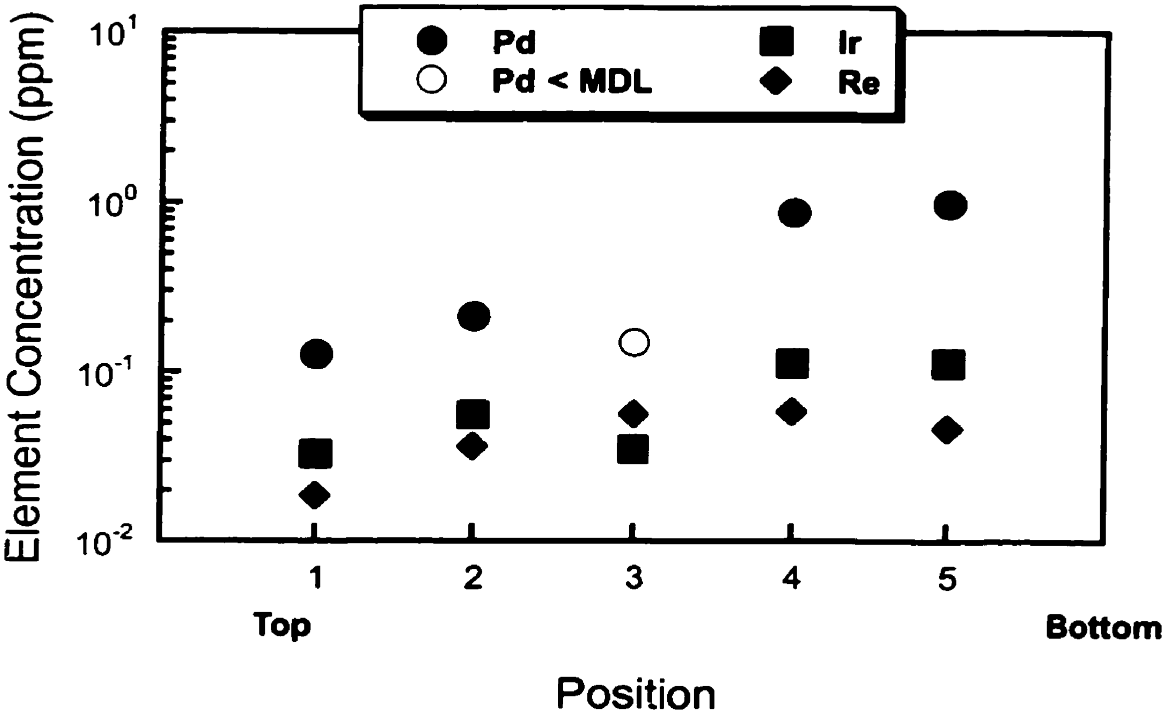

Figure 15.1. Plot of the trace element concentration variation in the glass from experiment IPRe4. The solid symbols represent the absolute concentrations of PGEs and Re, where as the open symbols denote levels below the minimum detection. The experiment was performed at 1 GPa, 1330 °C (final temperature), and for 48 hours. The sample was initially doped with a Fe-Ni sulfide melt containing 1 wt% Pd, Re, and Ir, which resulted in alloy saturation. This profile indicates low levels of Pd, Re and Ir close to sulfide globules and chromite crystals (points 1, 2, 3) and elevated concentrations away from those phases (points 4, 5).

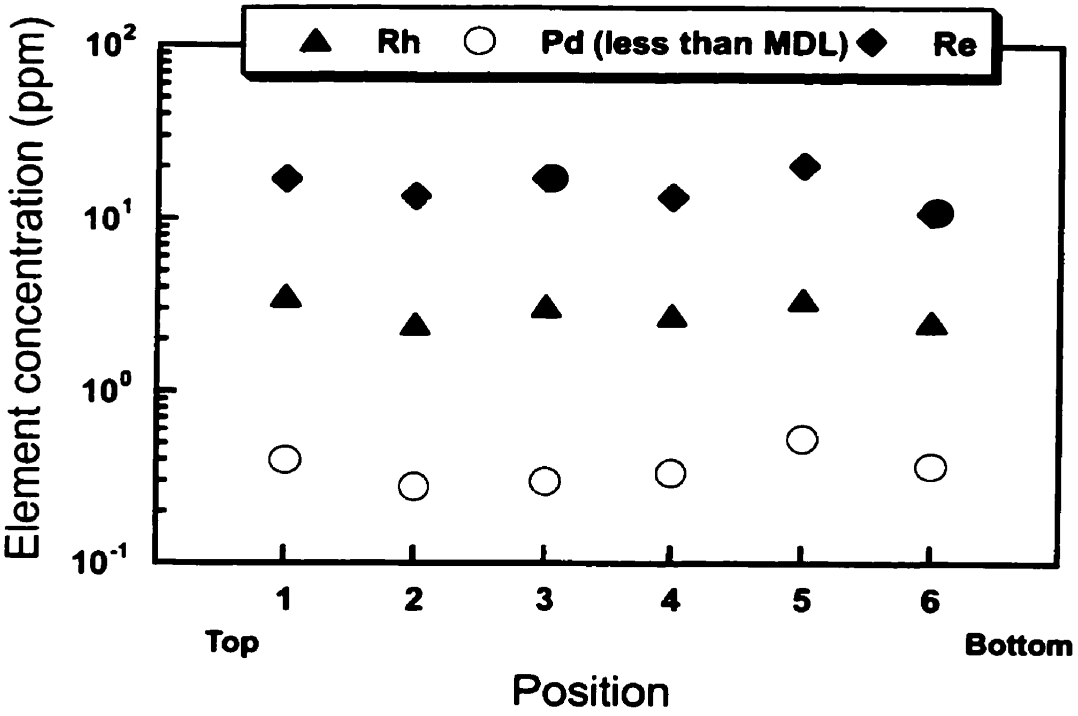

Figure 15.2. Plot of the trace element variation in glass from PGECoS. This run was saturated in a Re-PGE-Co alloy. The experiment was carried out at 1 GPa, 1330 °C (final temperature), and duration of 20 hours. In this sample, Re and Rh seem to be dispersed homogeneously throughout the silicate melt.

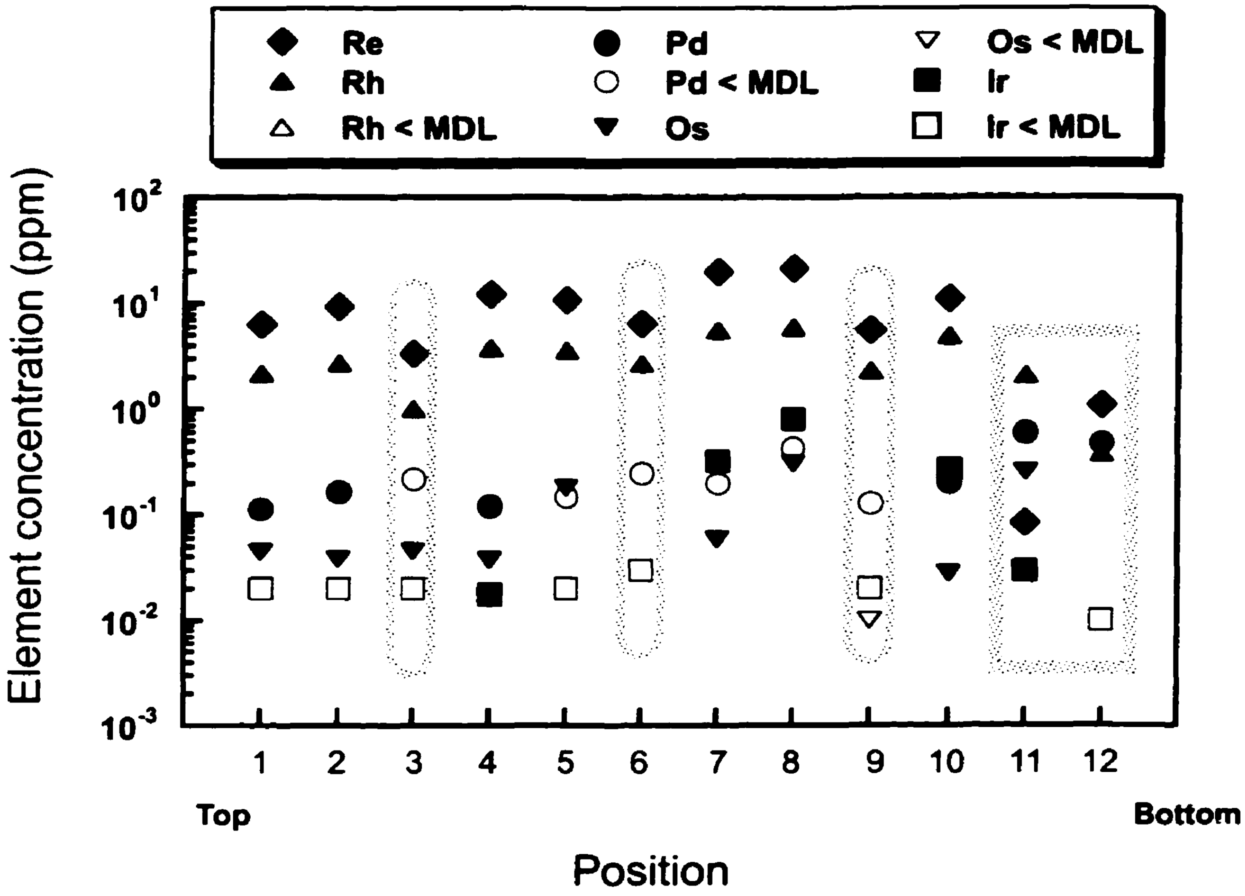

Figure 15.3. Plot of the trace element variation in glass from experiment PGECo. This experiment was performed at 1 GPa, 1330 °C for 20 hours, in the presence of PGE-Re-Co alloy. The solid symbols stand for absolute values and open symbols represent concentrations below minimum detection limits. The ellipsoids show analyses around the chromite grains for locations 3, 6 and 9. The square represents analyses close to the alloy phases. Rh and Re are the elements showing consistently high concentrations, yet they demonstrate macro-scale heterogeneity in terms of concentration in the glass.

3.3.3 Sulphide melt/silicate melt partition coefficients

Table A7.1 summarizes the sulphide-silicate liquid partition coefficients for Re and PGEs in all runs cast as Nerst distribution coefficients [(wt% $\text{metal}_{\text{sulphide}}$)/(wt% $\text{metal}_{\text{silicate-melt}}$). A minimum D-value for sulphide/silicate melt partitioning was calculated for those elements with concentrations below the minimum detection limits in the silicate melt (Table A6-1), as opposed to elements with detectable concentrations in glass such as Pd, Re, and Ir where absolute D-values were calculated. In terms of assessing sulphide and silicate melt equilibrium, we monitored the D-values for Ni and Re among runs of different duration, and results are presented in Figure 16, which depicts the variation of sulphide-silicate melt D-values for Re and Ni as a function of time. The D_{Ni} is very reproducible with an average value of 1087 (± 253), which is consistent with the reported value of D_{Ni} ranging from 1048-1155 in a silicate melt consisting of 8-9 wt% FeO, at an oxygen fugacity of $\sim 10^{-8.5}$, temperature of 1450 °C and pressure of 0.81 GPa reported by Peach and Mathez (1993). D_{Re} ranges from 0.188 (± 0.12) x 10^{4} to 1.83 (± 0.78) x 10^{4}, which is considerably higher than the D_{Re} of 43 measured from a natural MORB sample (Roy-Barman et al., 1998). The plot also distinguishes D_{Ni} and D_{Re} for the experiments where the sample was sealed in an outer Pt capsule from those in graphite capsules only, in order to monitor the effect of Pt contamination in the determination of D-values. D_{Ni} is not affected by the presence of the Pt-capsule, whereas D_{Re} shows a slight variability, most likely owing to the Re loss in the experiments containing a Pt-capsule. As a final point both D_{Ni} and D_{Re} are relatively invariant with time, consistent with the approach to sulphide/silicate melt equilibrium.

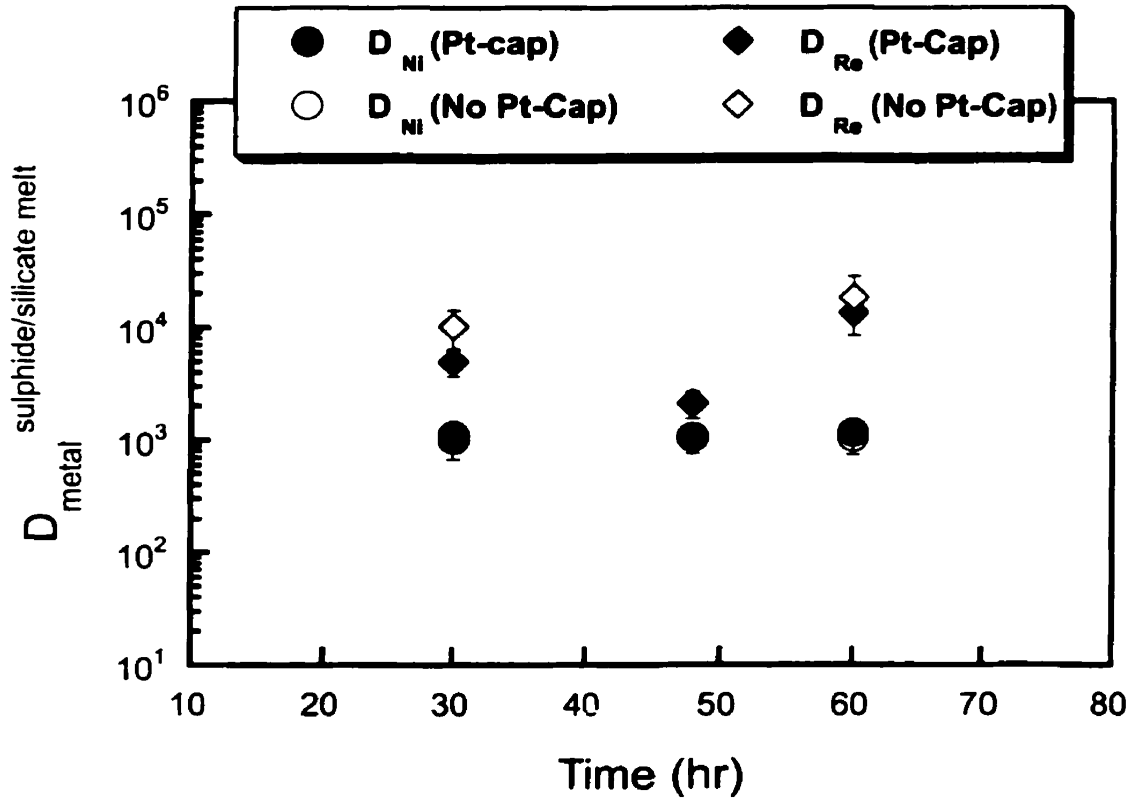

Figure 16. Variation of sulphide-melt/silicate-melt partition coefficients for Ni and Re in high pressure experiments as a function of time. This plot also provides a comparison between runs sealed in graphite-lined Pt capsules and those in graphite capsules only. D_{Ni} is very constant in all runs at ~1087 (253), where as D_{Re} is varies slightly [0.2-1.8 x 10^4 (0.5)].

3.3.4 Chromite/Silicate melt partition coefficients

Chromite/silicate melt partition coefficients for Ni, Co, Re and PGEs were also cast as Nerst distribution coefficients (wt% $\text{metal}_{\text{chromite}}$)/(wt% $\text{metal}_{\text{silicate- melt}}$), that are summarized in Table A7.2.

Figure 17 shows the measured chromite-silicate melt partition coefficient for Ni from all the sulphide bearing runs. The $D_{Ni}^{\text{chromite/melt}}$ values do not show significant variation with Ni abundance in the silicate melt or run durations (30 to 60 hrs), which is consistent with Henry's Law behaviour and suggests chromite-melt equilibrium was approached. In PGE-Co-bearing run products (PGECo and PGECoS) the chromite-silicate melt partition coefficient for Co is 4.93 (±0.62), which is in agreement with the $D_{Co}^{\text{spinel/melt}}$ of 5.3 (± 0.49) over the temperature range of 1235 to 1255 °C and fO_2 of $10^{-4.9}-10^{-5.5}$ reported by Horn et al., (1994).

As for Re and the PGEs, chromite/silicate-melt partition coefficients were calculated using glass analyses proximal to chromite in order to achieve the best sample of the glass-environment that the chromite was growing from (despite macro-scale melt heterogeneity). Such partition coefficients were calculated as either maximum or absolute values. The maximum values in this case corresponds to those analyses where the Re and PGE concentrations in the chromite were lower than the minimum detection limits of LA-ICP-MS. Re is the only element with detectable concentrations in some of the chromites in our study as shown in Table A6-2, which were analysed at pit sizes of 15-25 microns. Table A7-2 lists individual chromite-melt partition coefficients showing absolute values of 0.044-0.15 for Re, and maximum estimated D-values for PGEs in decreasing order: Ru<10.2, Os<4.3, Ir<1.2, Pd<0.23, Rh <0.13.

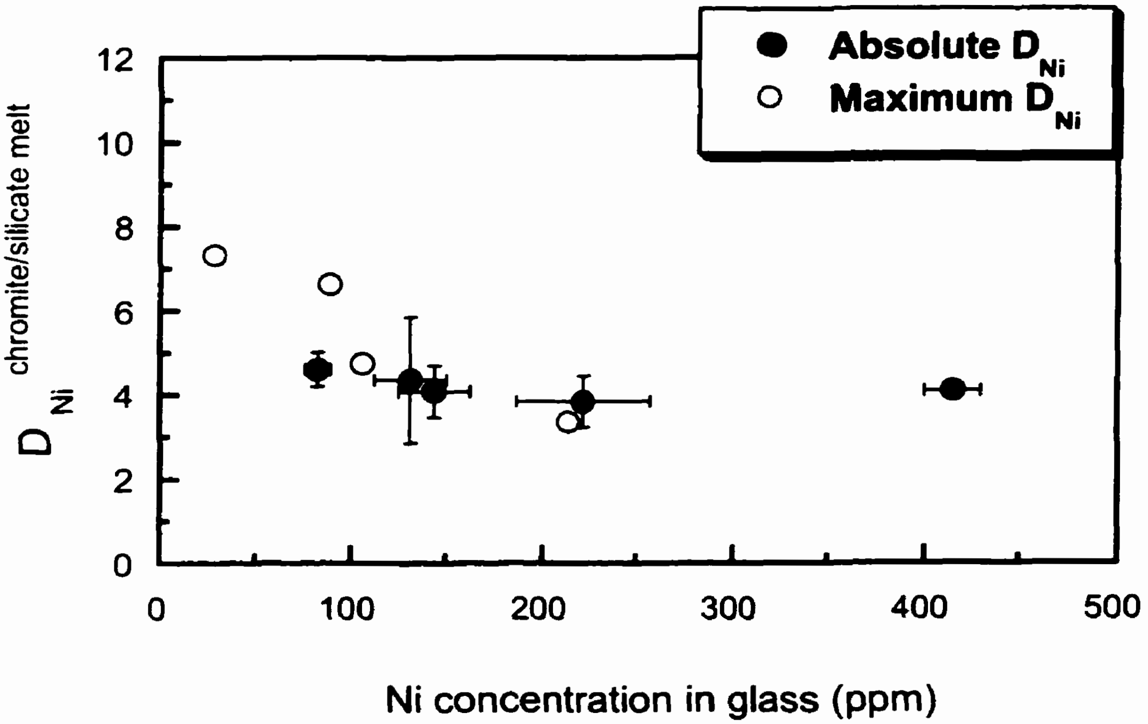

Figure 17. Plot of Ni abundance in the silicate melt vs. the chromite-melt partition coefficient. $D_{Ni}^{chromite/silicate\text{-}melt}$ is determined using LA-ICPMS for all sulfide bearing runs of different duration (i.e. from 30 to 60 hrs as shown in table 2-c). Solid symbols represent the absolute values of D_{Ni} and open circlesfor Maximum D_{Ni} based on values lower than the minimum detection limit for Ni in chromites. Error bars are determined based on the 1σ error for Ni concentrations in glass and chromites. D_{Ni} does not show any dependence on either the Ni content of glass, or the duration of the runs (not shown). Thus, D-values show consistent reproducibility among chromites, which indicates the approach to chromite-melt equilibrium and the adherence to Henry's Law.

CHAPTER IV: DISCUSSION OF RESULTS

4.1 Comparison of $D_{metals}^{sulphide\text{-}melt/silicate\text{-}melt}$ with other studies

Figure 18 portrays the sulphide-silicate liquid partition coefficients measured in this study in comparison to previous determinations. Values of D_{Ir} and D_{Pd} (Table A7.a) are in close agreement with the reported D-values of 3.5 $x10^4$, and 3.4 $x10^4$, respectively measured by Peach and coworkers (1994) in natural MORB samples with sulphide-silicate ratios of 5:95 at 1450 °C, 0.8 GPa and oxygen fugacity of $\sim 10^{-8.4}$. Fleet et al., (1996) and Crocket et al., (1997) also reported similar Os, Ru, Ir, Pd D-values in their recent work on sulphide bearing basaltic glasses at 1200-1250 °C, 1 atm where the PGEs in the glass were analysed using Instrumental Neutron Activation Analysis (INAA). Roy-Barman et al., (1998), estimated sulphide/silicate D's for Os and Re from natural MORB, and obtained values of 4.8 x 10^4 (Os) and 43 (Re). The concentrations of Re and Os in silicate and sulphide phases were determined by negative thermal ionization mass spectrometry (NTIMS), after magnetic separation of minerals, their digestion in HBr and HF solutions and extraction through ion exchange columns. Although our minimum D-values for Os are in fair agreement with the latter values, our D-values for Re range from 513 to 18323, which are distinctively higher than that determined by Roy-Barman et al., (1998). The reason for this difference may trace back to the sample preparation, and analytical techniques. In our *in situ* studies, as described earlier, only those glass analyses with the least heterogeneous domains (i.e. least inclusions) were employed in determining Re and PGE concentrations, whereas Roy-Barman and coworkers determined Re contents of glass using mineral separation, digestion of silicate melt and final NTIMS, where they still pointed out that their glass samples contained some sulphides. Even a small amount of sulphide contamination can have a profound influence on measured D-values. For example, addition of only 0.1% sulphide melt to our glass compositions would reduce our measured D-values by a factor of 1000, thus possibly accounting for the low D's measured by Roy-Barman. Bezmen et al., (1994) in their investigation of sulphide-silicate melt partitioning reported high D-values for Ru, Rh, Pd, and Ir for a system consisting of H-O-C-S fluid at 1200-1300 °C and 0.1-0.4 GPa using a Pt-capsule, which are approximately consistent with our results, except for Os. They attributed their high partition coefficients to the presence of fluid in the system where hydrogen may contribute to increased activity of Fe in sulphides and thus, enhancing the levels of dissolved PGEs. They also reported the presence of Os-sulphide crystallised in the sulphide and silicate melt that interfered with analysis of pure Os in different phases that could count for their unusually low D_{Os} in comparison with ours and other studies, as shown in Figure 18.

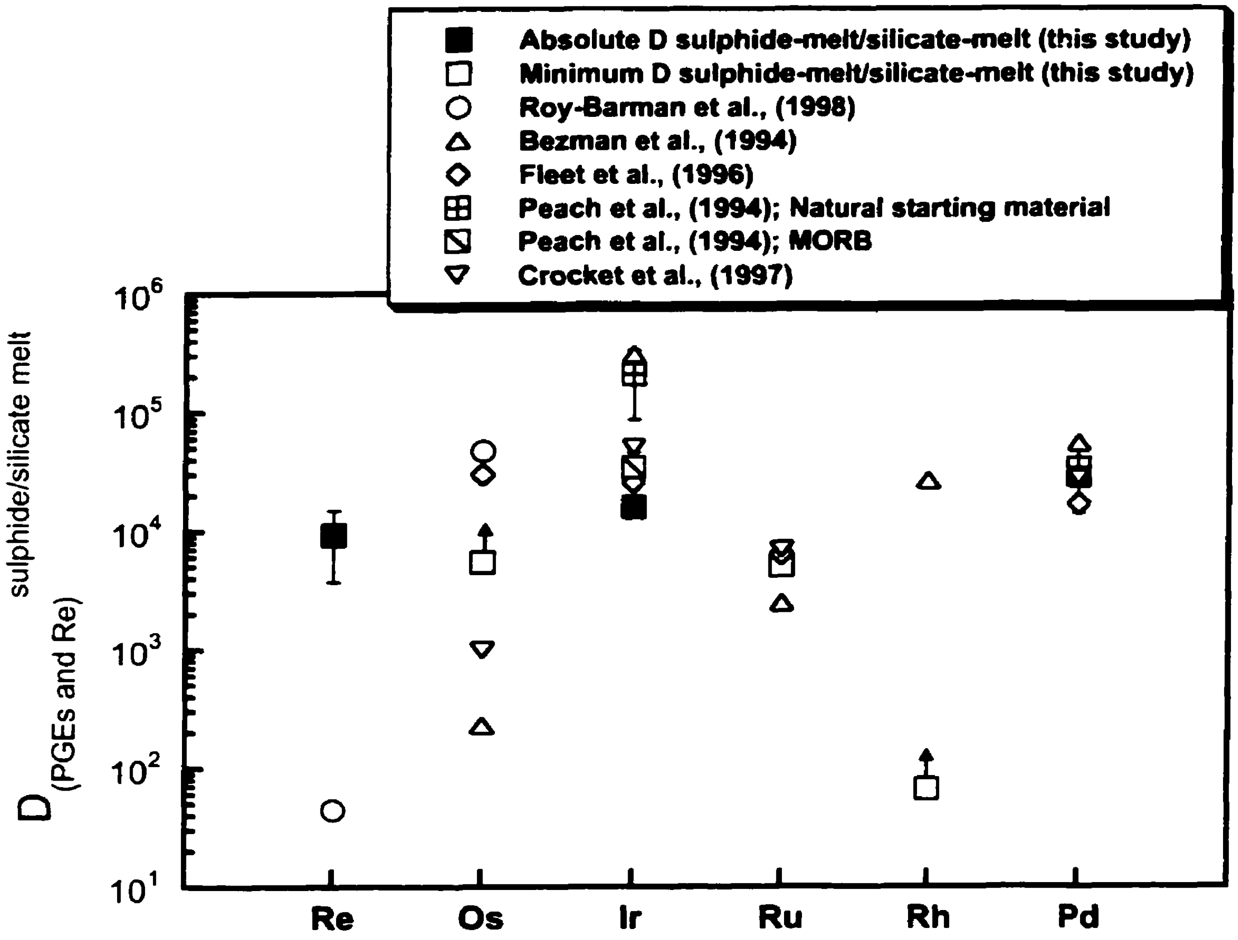

Figure 18. Comparison of absolute and minimum two liquid partition coefficients (sulphide and silicate) of this study for PGEs and Re with previous determinations. Minimum values are calculated D's in which the glass metal content was less than the minimum detection limit. The error bars correspond to 1 σ standard deviation of the mean.

4.2 Comparison of $D_{metal}^{mineral/silicate-melt}$ with other studies

Figure 19 shows the chromite-silicate melt partition coefficients for Re and PGEs measured in this study in comparison to previous estimates based on experiments or phase separation in natural samples. Capobianco et al., (1994) reported partition coefficients between Cr bearing-magnetite and haplobasalt of 110 (± 70), 430 (± 140), and 0.6 (± 0.3) for Ru, Rh and Pd, respectively. In their investigation, samples were synthesized in a sulphide free environment in the presence of pure Ru, Rh, Pd metals at 1 atm, 1275 °C, and fO_2 of $10^{-3.6}$. Glasses were analysed using both secondary ion mass spectrometry (SIMS) for Ru, and Rh, and electron microprobe for Pd. Cr-bearing magnetites were analysed by EMP using long counting times (180-300 seconds) and beam currents of 100-150 nA for Pd, and 20-30 nA for Ru, and Rh. The Ru contents of run product glasses where estimated using Ru solubilities determined for Cr-free compositions synthesized at similar conditions. The high magnetite-melt partition coefficients are attributed to high oxygen fugacity in that the PGEs are present as oxidised species that readily substitute for Fe^{3+}. Capobianco et al., (1994) also found that the magnitude of magnetite-melt D-values for Ru are reduced 4-fold in response to the addition of 3-6 wt% Cr to the magnetite composition, which suggests there is competition between Ru and Cr for octahedral sites in the spinel structure. Our $D^{chromite/melt}$ values are systematically lower than the values reported by Capobianco et al., (1994), which is most likely a result of differences in spinel composition (chromite vs. Cr-bearing magnetite) and the more reducing conditions (fO_2 $10^{-8.5}$ – $10^{-9.7}$) in our experiments. In contrast, our results compare well with the estimated chromite-melt partition coefficients from Peck et al., (1992) and the Cr- spinel/melt values from Hart and Ravizza (1996), which were both based on analyses of pure phase separates. Our D-values show that Re and some

PGEs (Pd, Rh, and Ir) are clearly incompatible in chromite, yet for other PGEs (Ru, Os) further work is required to fully assess the role of chromite in controlling the behaviour of these elements during melting processes. A more detail discussion of the crystal-chemical controls on chromite-melt partitioning of Re and the PGEs is provided in the subsequent section.

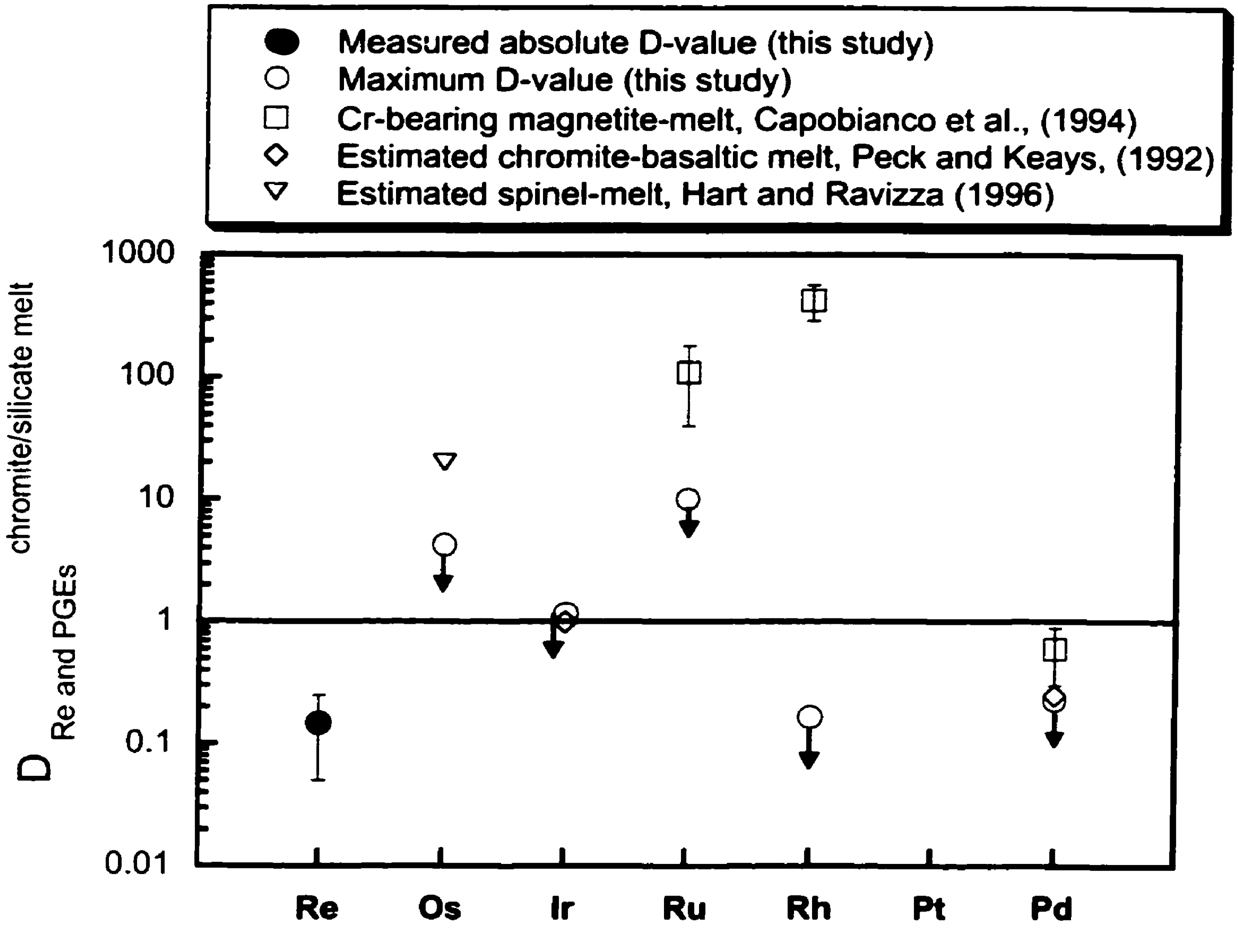

Figure 19. Plot of chromite-silicate melt partition coefficients for Re and the PGEs portraying the results of this study in comparison to previous work. The open circles with arrows present the maximum D-values for PGEs (Os, Ru, Rh, and Ir), where as the filled circle shows the absolute value for Re. The maximum values are the calculated D-values in which the metal concentrations were below detection limits in glass.

4.3 Control of the spinel structure on Re and PGE partitioning

The crystal chemistry of minerals exerts a major influence on trace element partitioning in mineral-melt systems. Specifically, the partitioning of trace elements may be controlled by factors such as: ionic radius and charges, size and coordination number of the crystal lattice site on which the substitution take place (octahedral, tetrahedral or interstitial) and crystal field effects (Onuma et al., 1968; Jensen, 1973; Henderson, 1982). Plots of partition coefficients against ionic radius for cations of the same charge (ie. Onuma plots) have clearly demonstrated the control of the ionic radius and charge of the substituting ions (Onuma et al., 1968; Jensen, 1973). These plots display a smooth parabola whose apex corresponds to the optimal ionic radius for element substitution. Deviations from the parabola indicate the influence of factors other than ionic radii and charge, such as crystal field effects. Crystal field effects (CFE) are exhibited by the transition metals and lanthanides whose bonding involves d and/or f atomic orbitals (Henderson 1982). Owing to the electronic configuration of these elements, a high degree of stability is achieved if bonding occurs in octahedral (sometimes teterahedral) coordination. Details of the electron configurations, orbital orientations and determination of octahedral and/or tetrahedral field energies are provided in Henderson (1982). Here, it is sufficient to point out that the distribution of transition elements is influenced by the octahedral or tetrahedral site preferences as a consequence of the aforementioned electron configurations.

In previous studies involving magnetite/melt partitioning, Re and the PGEs were assumed to be comparable in charge and ionic radius to Fe^{3+} (Righter et al., 1998; Capobianco et al., 1994; Capobianco and Drake, 1990) and their high partition coefficients were explained using Onuma plots. Comparison of the octahedral site preference energy (OSPE; a measure of the cation stability in octahedral coordination) for 3+ transition metal cations shows that Cr^{3+} has the highest OSPE of the trivalent transition metals (Fe^{3+}, V^{3+}), although each has similar ionic radius. Thus, for chromite, the partitioning behaviour of Cr^{3+} cannot be used to predict the relationship between ionic radii and partition coefficient as described in detail below.

Blundy and Wood (1994), and Beattie (1994) derived a predictive model for crystal-melt partitioning in terms of the strain energy associated with a cation substituting into a crystal lattice whose ionic radius differs from the optimal radius of that site. They used the following expression, which relates the partition coefficient of a cation to the elasticity of the substitution site, the ionic radius of the cation and the optimal radius of the site:

$$D_i(P, T, x) = D_o(P, T, x) \exp\left[\frac{-4\pi E N_A}{RT}\left\{\frac{r_o}{2}(r_i - r_o)^2 + \frac{1}{3}(r_i - r_o)^3\right\}\right] \qquad \text{(Equation 4-1)}$$

where:

E = Young's modulus of host mineral
N = Avogadro's number
r_o = optimal site radius
r_i = ionic radius of dopant
R = Gas constant
T = Temperature (K)
D_o (P, T, x) = partition coefficient corresponding to the optimal radius at particular P, T and mineral composition
D_i (P, T, x) = partition coefficient of the dopant cation

In this model, a plot of partition coefficient against ionic radius for cations of like charge yields a parabola whose apex defines the partition coefficient corresponding to the optimal radius for that site. This approach allows us to predict the partitioning behaviour of major or trace elements in different sites of the crystal lattice. Using this method, experimentally determined magnetite-silicate melt partition coefficients for trace elements (Horn et al., 1994) were fit using equation 4-1, assuming a normal spinel structural formula of AB_2O_4, where divalent cations (i.e. Co, Mg, Mn, Ni, Zn) substitute on the A (tetrahedral) site, and tri/tetra-valent cations (i.e. Al, Cr, Fe, and Ti) substitute on B (octahedral) site. Figure 20 portrays the A and B-site partitioning patterns derived from this analysis. The difficulty in assessing the partitioning pattern of Re and PGEs results from the lack of information on the ionic radius of these elements in tetrahedral and or octahedral coordination and the uncertainties regarding their oxidation states. Thus, in plotting our maximum and absolute chromite-melt partition coefficients, we assumed the following valence states for PGEs based on the available database: Ir^{2+}, Re^{2+} (O'Neill et al., 1995), Re^{3+} (Righter et al., 1998), Ru^{3+} and Rh^{3+} (Capobianco et al., 1994, Capobianco and Drake, 1990), Pd^{2+} (Ertel et al., 1999). The ionic radii for Os^{3+}, Ir^{3+}, Ru^{3+}, Re^{3+} were estimated by assuming a linear relationship between the charge and the radius of these elements. As shown in Fig. 20, the increase in Cr content of the magnetite towards chromite composition, produces a small decrease in the partition coefficients of di- and trivalent trace elements. Most importantly, this type of analysis indicates that partition coefficients for Re and PGEs are likely to be less than one, which is in general agreement with the findings of this study. Of course, this type of analysis is subject to some uncertainty since the true valence state of PGEs is not well constrained and predictions are based on octahedral coordination (ionic radii in tetrahedral coordination is smaller than octahedral coordination).

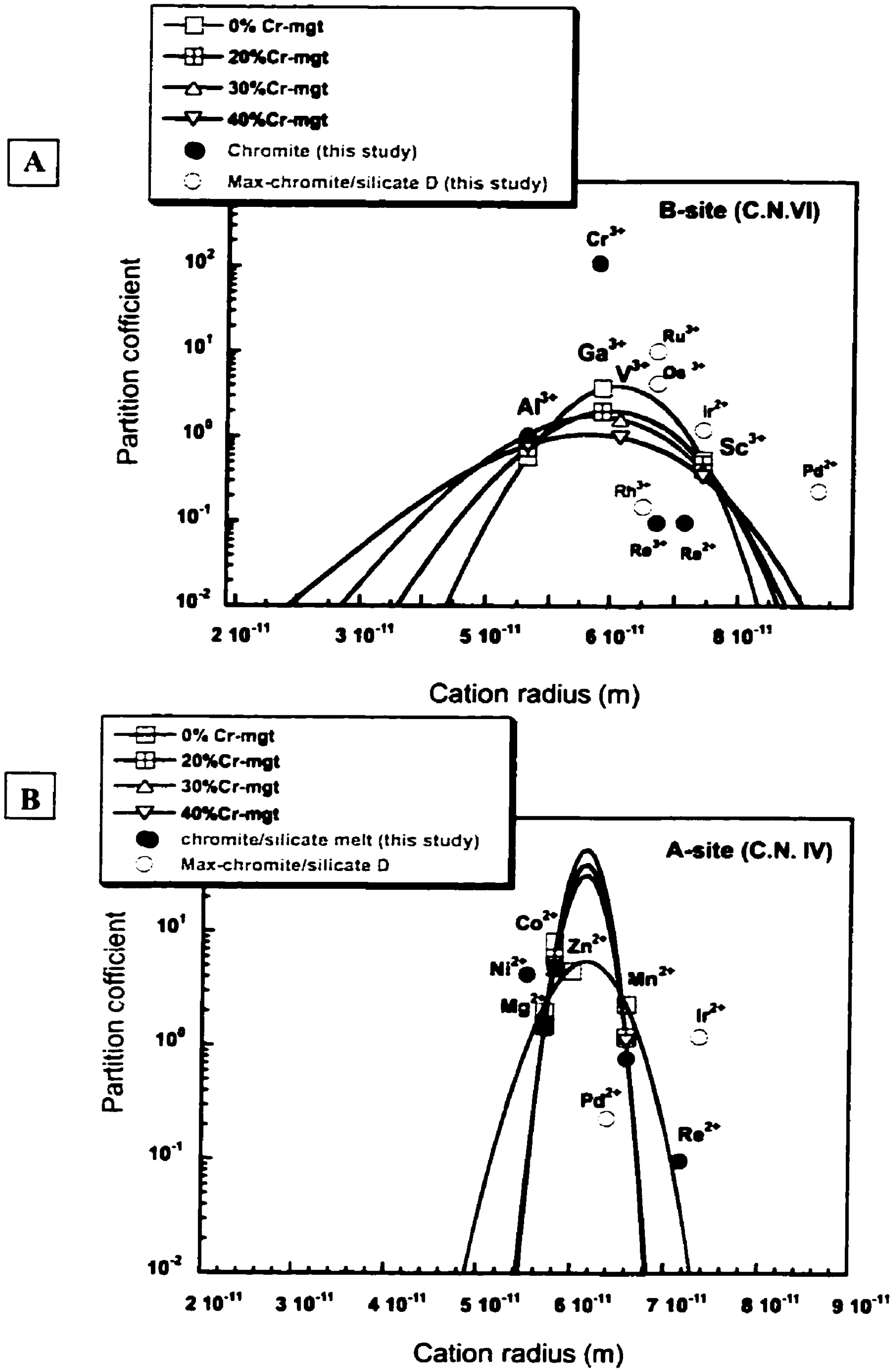

Figure 20. Plot of Magnetite-Chromite/melt partition coefficients (Horn et al., 1994) as a function of ionic radius used to predict chromite-melt partition coefficients for Re and PGEs (after Blundy and Wood, 1994). Coordination of A and B-sites of spinel are tetrahedral (4-fold) and octahedral (8-fold), respectively. Due to the lack of data on valence states for Re and PGEs in different coordinations, ionic radius of 6-fold species were employed in estimating the radius for divalent or trivalent cations of these elements. Parabolas describing the D-values are curves fit to equation 4-1 using non-linear least squares regression.

4.4 Implications for the behaviour of Re in basalts and Re/Os fractionation

Hauri and Hart (1997) showed that during chromite crystallisation in MORB and OIB, Re is more incompatible than Cr, based on observed increases in melt Re contents with decreasing Cr abundances. These observations are consistent with the low chromite-melt partition coefficients for Re measured in this study. In contrast to the incompatibility of Re in chromite, Righter et al., (1998) have shown the extreme compatibility of Re in magnetite (D= 20-50). In addition, Righter and Hauri (1998) have demonstrated the possible role of garnet as a host for Re rather than spinel in the upper mantle, based on partitioning experiments conducted at 1250-1350 °C, 1.5-2 GPa, and fO_2 of $10^{-8.4} - 10^{-10}$, in which the average garnet-melt partition coefficient for Re was found to be ~2.7. These results suggest that the behaviour of Re in igneous systems will be sensitive to the identity of the crystallising oxide phase and whether melting occurs in the spinel or garnet facies.

As for Os, it has been shown that it is more compatible than Re during mantle melting processes (Martin et al., 1994), as evidenced by the low Re/Os ratio of MORB samples. Understanding the origin of the differing compatibility of Re and Os during melting would serve to provide constraints on the osmium isotopic evolution of the crust and the upper mantle. Our maximum chromite-silicate melt partition coefficient for Os ($D_{Os}<$ 4.3) and low absolute D_{Re} (0.044-0.15) suggest that melting in the presence of chromian spinel could contribute to producing the low Re/Os ratio observed in basaltic rocks. However, owing to the low abundance of spinel in mantle rocks, the observed Re/Os fractionation requires bulk partition coefficients greater >1, which cannot be produced by spinel alone. The exact role of other mantle phases in this regard awaits a more precise determination of their Os partition coefficients.

4.5 Chromite as a PGE collector

Here, an alternative to PGE concentration by solid solution in chromite is proposed, based on textural relationships observed among phases in run products from our experiments. As shown in Figure 7, chromites synthesized in our experiments frequently contained alloy or sulphide inclusions. These inclusions vary in size from micron size particles as observed by trace element heterogeneities during time-resolved analysis (Fig 14.1) to 30-70 microns as observed in the exposed surfaces of chromites (Fig 7.1a, 7.1c). These textural relationships suggest that chromite nucleation occurs preferentially at sulphide liquid/silicate melt or alloy/silicate melt interfaces. Thus, other means of explaining the association of PGEs and chromitites would be the precipitation of PGE phases during the early stages of chromite crystallisation and their subsequent collection and accumulation by chromite settling (Hiemstra, 1979). This idea is also supported by textural observations on chromites from both the layered intrusions (Talkington and Lipin, 1986; Peck and Keays 1990; Peck et al., 1992; Merkle, 1992; Maier et al., 1999) and ophiolite complexes (Stockman and Hlava, 1984; Legendre and Ague, 1986; Auge 1985, 1988; McElduff and Stumpfl, 1990; Torres-Ruiz et al., 1996; Nakagawa and Franco, 1997; Garuti et al., 1999) in which both laurite (RuS_2), and Ru-Os-Ir alloy are commonly reported inclusion phases. Finally, the last line of evidence comes from the experimental work of Brenan and Andrews (2000) who showed that laurite and Ru-Ir-Os alloy could be stable on the chromite liquidus temperature, thus confirming the magmatic origin for these minerals as inclusions in chromite.

CHAPTER V: CONCLUSIONS

In this investigation, the partitioning behaviour of Re and PGEs in a chromite-saturated melt, at both 1 GPa and 1 atm, 1330 °C (final T), and fO_2 of $10^{-8.5}$-$10^{-9.7}$, was examined to assess the role of this mineral in concentrating Re and PGEs. In this study, LA-ICP-MS was the choice of trace element analysis owing to it being an situ analytical technique with low minimum detection limits and high spatial resolution which allowed us to observe and avoid the presence of any heterogeneities at the macro to micro-scale levels in different phases. Here, we report the first validation of sulphide liquid/silicate liquid partition coefficients using an *in situ* technique and values compare well with previously determined D-values using phase separation and bulk sample analysis. Absolute sulphide/silicate melt Ds were found to be (in decreasing order): Pd (29289 ± 2000)> Ir (16136 ± 3000) >> Re (9431 ± 5650), and minimum: Os (5479) > Ru (3978) > Rh (67). In addition, we have determined the first chromite-silicate melt partition coefficients for Re (0.044-0.15) and have better constrained the upper limits of $D^{\text{chromite-melt}}$ for PGEs in the following order; Ru <10.26, Os <4.3, Ir <1, Pd <0.23, and Rh <0.17. Our results indicate that Re and some PGEs (Pd, and Rh) are incompatible in chromite, and that the compatibility of other PGEs (Ru, Os, and Ir) is less than that estimated previously. Textural observations support the notion that entrapment of PGE rich phases during initial crystallisation of chromite is a possible means of explaining the PGE-chromite association.

REFERENCES

Auge, T., 1985. Platinum-group mineral inclusions in ophiolitic chromite from the Vourinos Complex, Greece, Canadian Mineralogist 23, 163-171.

Auge, T., 1988. Platinum-group minerals in the Tiebaghi and Vourinos ophiolitic complexes: Genetic implications, Canadian Mineralogist 26, 177-192.

Allegre, CJ, and Luck, J., 1980. Osmium isotopes as petrogenetic and geological tracers, Earth and Planetary Science Letters 48, 148-154.

Andrews, D., and Brenan, J.M., 2000. High temperature stability of laurite and Ru-Os-Ir alloy and their possible role in IPGE/PPGE fractionation in magmatic systems, (abstract), American Geophysical Union Spring Meeting.

Barnes, S.J., Maier W.D., 1999. Platinum-Group elements in silicate rocks of the Lower, Critical and Main Zones at Union Section, Western Bushveld Complex, J. of Petrology 40, 1647-1671.

Barnes, S-J., Naldrett, A.J., and Gorton, M.P., 1985. The origin of the fractionation of platinum-group elements in terrestrial magmas, Chemical Geology 53, 303-323.

Barnes, S-J, and Picard, C.P., 1993. The behaviour of platinum-group elements during partial melting, crystal fractionation, and sulphide segregation: an example from the Cape smith Fold Belt, northern Quebec, Geochim. et. Cosmochim. Acta 57, 70-87.

Beattie, P. 1994. Systematics and energetics of trace element partitioning between olivine and silicate melts: implications for the nature of mineral/melt partitioning, Chemical Geology, 117, 57-71.

Bezmen, N.I., Asif, M., Brugmann, G.E., Romanenko, I.M., Naldrett, A.J., 1994. Distribution of Pd, Rh, Ru, Ir, Os, and Au between sulphide and silicate metals, Geochim. et. Cosmochim. Acta 58, 1251-1260.

Blundy, J.D., and Wood, B.J., 1994. Prediction of crystal-melt partition coefficients from elastic moduli, Nature, 372, 452-454.

Borisov, A., Palme, H., and Spettel, B., 1994. Solubility of palladium in silicate melts: implications for core formation in the earth, Geochim. et. Cosmochim. Acta 58, 705-716.

Boudreau, A.E., and McCallum, I.S., 1986. Investigations of the Stillwater Complex: III. The picket Pin Pt/Pd deposit, Economic Geology, 81, 1953-1975.

Boudreau, A.E., and McCallum, I.S., 1992. Concentration of platinum-group elements by magmatic fluids in layered intrusions. Economic Geology 87, 1830-1848.

Boyd, J.R., and England, J.L., 1960. Apparatus for phase equilibrium measurements of pressures up to 50 kilobars and temperatures up to 1750 °C, J. Geophys. Res. 65, 741-748.

Brenan, J.M., and Caciagli, N.C., 2000. Fe-Ni exchange between olivine and sulphide melt: Implications for oxygen barometry in sulphide-saturated magmas, Geochim. et. Cosmochim. Acta 64, 307-320.

Brenan, J.M, and Andrews, D., 2000. High temperature stability of laurite and Ru-Os-Ir alloy and their role in PGE fractionation in mafic magmas, Submitted to Canadian Mineralogist.

Brugmann, A.E., Arndt, N.T., Hofmann, A.W., and Tobschall, H.J., 1987. Noble metal abundances in komatiite suites from Alexo, Ontario and Gorgona Island, Colombia: Geochim. et. Cosmochim. Acta 51, 2159-2169.

Capobianco, C.H., and Drake, M., 1990. Partitioning of ruthenium, rhodium, and palladium between spinel and silicate melt and implications for platinum-group element fractionation trends, Geochim. et. Cosmochim. Acta 54, 869-874.

Capobianco, C.H., Hervig, R.L., and Drake, M., 1994. Experiments on crystal/liquid partitioning of Ru, Rh and Pd for magnetite and hematite solid solutions crystallised from silicate melt, Chemical Geology 113, 23-43.

Christie, D.M., Carmichael, I.S.E., and Langmuir, C.H., 1986. Oxidation states of mid-ocean ridge basalt glasses, Earth Planetary Science Letters 79, 397-411.

Cousins, C.A., and Vermaak, C.E., 1976. The Contribution of Southern African ore deposits to the geochemistry of the platinum group metals. Economic Geology 71, 1308-1223.

Crocket, J.H., 1979. Platinum-group elements in mafic and ultramafic rocks: A survey. Canadian Mineralogist 17, 391-402.

Crocket, J.H., and MacRae, W.R., 1986. Platinum-group element distribution in komatiitic and tholeiitic volcanic rocks from Munro Township, Ontario, Economic Geology 81, 1242-1251.

Crocket, J.H., Fleet, M.E., and Stone, W.E., 1992. Experimental partitioning of osmium, iridium and gold between basalt melt and sulphide liquid at 1300 °C, Australian Journal of Earth Sciences 39, 427-432.

Crocket, J.H., Fleet, M.E., and Stone, W.E., 1997. Implications of composition for experimental partitioning of platinum-group elements and gold between sulphide liquid and basalt melt: The significance of nickel content, Geochim. et. Cosmochim. Acta 61, 4139-4149.

Ertel, W., O'Neill, H.St.C., Sylvester, P.J., and Dingwell, D.B., 1999. Solubilities of Pt and Rh in a haplobasaltic silicate melt at 1300 °C, Geochim. et. Cosmochim. Acta 63, 2439-2449.

Fleet, M.E., and Stone, W.E., 1991. Partitioning of platinum-group elements in the Fe-Ni-S system and their fractionation in nature, Geochim. et. Cosmochim. Acta 55, 245-253.

Fleet, M.E., and Wu, T-W., 1993. Volatile transport of platinum-group elements in sulphide-chloride assemblages at 1000 °C, Geochim. et. Cosmochim. Acta 57, 3519-3551.

Fleet, M.E., Crocket, J.H., and Stone, W.E., 1996. Partitioning of platinum-group elements (Os, Ir, Ru, Pt, Pd) and gold between sulphide liquid and basalt melt, Geochim. et Cosmochim. Acta 60, 2397-2412.

Gaetani, G.A., and Grove, T.L., 1997. Partitioning of moderately siderophile elements among olivine, silicate melt, and sulphide melt: Constraints on core formation in the Earth and Mars, Geochim. et. Cosmochim. Acta 61, 1829-1846.

Gaturi, G., Zaccarini, M., and Economou-Eliopoulos, M., 1999. Paragenesis and composition of laurite from chromitites of Othrys (Greece): implications for Os-Ru fractionation in ophiolitic upper mantle of the Balkan Peninsula, Mineralium Deposita 34, 312-319.

Hart, S.R., and Ravizza, G.E., 1996. Os Partitioning between phases in lherzolite and basalt, Geophysical Monograph 95, 123-134.

Hauri, E.H., and Hart S.R., 1997. Rhenium abundances and systematics in oceanic basalts, Chemical Geology 139, 185-205.

Henderson, P., 1979. Irregularities in patterns of element partition. Mineral. Mag. 43, 399-404.

Henderson. P. 1982. Structural controls of element distribution, In: Inorganic Geochemistry, Pergamon, Oxford, 102-155.

Hiemstra, S. A., 1979. The role of collectors in the formation of the platinum deposits in the Bushveld Complex, Canadian Mineralogist 17, 469-482.

Hill, R., and Roeder, P.L. 1974. The crystallisation of spinel from basaltic liquid as a function of oxygen fugacity, Journal of Geology 82, 709-729.

Hiemstra, S.A., 1986. The distribution of chalcophile and platinum-group elements in the UG-2 chromitite layer of the Bushveld Complex, Economic Geology 81, 1080-1086.

Hofmann, A.W., 1988. Chemical differentiation of the Earth: the relationship between mantle, continental crust, and oceanic crust, Earth. Planet. Sci. Lett. 90, 297-314.

Holloway, J.R., Pan, V., and Gudmundsson, G., 1992. High-pressure fluid-absent melting experiments in the presence of graphite: oxygen fugacity, ferric/ferrous ratio and dissolved CO_2, Eur. J. Mineral 4, 105-114.

Horn, I., Foley, S.F., Jackson, S.E., and Jenner, G.A., 1994. Experimentally determined partitioning of high field strength- and selected transition elements between spinel and basalt melt, Chemical Geology 117, 193-218.

Jackson, S.E., Longerich, H.P., Dunning, G.R., and Fryer, B. J., 1992. The application of laser ablation microprobe-inductively coupled plasma- mass spectrometry (LAM-ICP-MS) to in situ trace element determinations in minerals. Cand. Mineral. 30, 1049-1064.

Jenner, G.A., Foley, S.F., Jackson, S.E., Green, T.H., Gryer, B.J. and Longerich, H.P., 1993. Determination of partition coefficients for trace elements in high pressure-temperature experimental run products by laser ablation microprobe-inductively coupled plasma-mass spectrometry (LAM-ICP-MS), Geochim. et. Cosmochim. Acta 57, 5099-5103.

Jensen, B.B., 1973. Patterns of element partitioning. Geochim. et. Cosmochim. Acta. 37, 2227-2242.

Jurewicz, A. J.G., and Watson, E.B., 1988. Cations in olivine, Part 1: Calcium partitioning and calcium-magnesium distribution between olivines and coexisting melts, with petrologic applications, Contribution to mineralogy and petrology 99, 176-185.

Kress, V., 1997. Thermochemistry of sulphide liquids. I. The system O-S-Fe at 1 bar. Contribution to Mineralogy and Petrology 127, 176-186.

Legendre, O., and Ague, T., 1986. Mineralogy of Platinum-group mineral inclusions in chromitites from different ophiolitic complexes, In: Gallagher MJ. Ixer RA, Neary CR, Prichard HM (eds) Metallogeny of the basic and ultrabasic rocks. The institute of Mining and Metallurgy, London, 361-375.

Lorand, J.P., Pattou, L., and Gros M., 1998. Fractionation of platinum-group elements and gold in the upper mantle: a detailed study in Pyrenean Orogenic Lherzolites, Journal of Petrology 40, 957-980.

Maier, W.D., and Barnes, S-J., 1999. Platinum-group elements in silicate rocks of the Lower, Critical and Main zones at Union Section, Western Bushveld Complex, Journal of petrology 40, 1647-1671.

Maier, W.D., Prichard, H.M., Barnes, S-J., and Fisher, P.C., 1999. Compositional variation of Laurite at union section in the Western Bushveld Complex, S. Afr. Geol. 102, 286-292.

Martin, C.E., Carlson, R.W., Shirey, S.B., Frey, F.A., and Chen, C.-Y., 1994. OS isotopic variation in basalts from Haleakala Volcano, Maui, Hawaii: a record of magmatic processes in oceanic mantle and crust, Earth. Planet. Sci. Lett. 128. 287-301.

Merkle, R.K.W., 1992. Platinum-group elements in the middle group of chromitite layers at Marikana, western Bushveld Complex: indications for collection mechanisms and postmagmatic modification, Canadian Journal of Earth Sciences 29, 209-21.

McElduff, B., Stumpfl, E.F., 1990. Platinum-group minerals from the Troodos Ophiolite, Cyprus, Mineralogy and Petrology 42, 211-232.

McLaren, C.H., and De Villiers, J.P.R., 1982. The platinum-group chemistry and mineralogy of the UG-2 chromitite layer of the Bushveld Complex, Economic Geology 77, 1348-1365.

Mitchell, R.H., and Keays, R.R., 1981. Abundance and distribution of gold, palladium and iridium in some spinel and garnet lherzolites: implications for the nature and origin of precious metal-rich intergranular components in the upper mantle, Geochim. et. Cosmochim. Acta 45, 2425-2442.

Morgan, J.W., Wandless, G.A., Petrie R.K., and Irving A.J., 1981. Composition of the earth's mantle-1. Siderophile trace elements in ultramafic nodules, Tectonophysics, 75, 47-67.

Murck, B.W., and Campbell, I.H., 1986. The effect of temperature, oxygen fugacity and melt composition on the behaviour of chromium in basic and ultrabasic melts, Geochim. et. Cosmochim. Acta 50, 1871-1887.

Naldrett, A.J., Hoffman, E.L., Green, A.H., Chou, C.-L., and Naldrett, S. R., 1979. The composition of Ni Sulphide ores, with particular reference to their content of PGE and Au. Canadian Mineralogist 17, 403-415.

Naldrett, A.J., 1981. Platinum-group element deposits. A review; in Cabri, L. J. (ed), Platinum-group elements: mineralogy, geology, recovery: Canadian Institute of Mining and Metallurgy, Spec vol. 23. 197-231.

Nakagawa, M., and Franco, H., 1997. Placer Os-Ir-Ru alloys and sulfides: Indicators of sulfur fugacity in an ophiolite?, Canadian Mineralogist 35, 1441-1452.

O'Neill, H.St.C.O., Dingwell, D.B., Borisov, A., Spettel, B., and Palme, H., 1995. Experimental petrochemistry of some high siderophile elements at high temperatures, and some implication s for core formation and the mantle's early history, Chemical Geology 120, 255-273.

Onuma, N., Higuchi, H., Wakita, H., and Nagasawa, H. 1968. Trace element partitioning between two pyroxenes and host lava, Earth and Planetary Science Letters 5, 47-51.

Oshin, I.O., and Crocket, J.H. 1982. Noble metals in Thet-ford Mines ophiolites, Quebec, Canada. Part 1: Distribution of gold, iridium, platinum, and palladium in the ultramafic and gabbroic rocks. Economic Geology 77, 1556-1570.

Page, N.J., Rowe, J., and Haffty, J., 1976. Platinum metals in the Stillwater Complex, Montana, Economic Geology 71, 1352-1363.

Page, N.J., Cassard, D., and Haffty, J., 1982. Palladium, platinum, rhodium, and iridium in chromitites from the Massif du Sud and Tiebaghi Massif, New Caledonia, Economic Geology 77, 1571-1577.

Peach, C.L., and Mathez, E.A., Keays, R.R., 1990. Sulphide melt-silicate melt distribution coefficients for noble metals and other chalcophile elements as deduced from MORB: implications for partial melting, Geochim. Et. Cosmochim. Acta 54, 3379-3389.

Peach, C.L., and Mathez, E.A., 1993. Sulphide melt-silicate distribution coefficients for nickel and iron and implications for the distribution of other chalcophile elements, Geochim. et. Cosmochim. Acta 57, 3013-3021.

Peach, C.L., and Mathez, E.A., Keays, R. R., and Reeves, S. J., 1994. Experimentally determined sulphide melt-silicate melt partition coefficients for Iridium and palladium, Chemical Geology 117, 361-377.

Peach, C.L., and Mathez, E.A., 1996. Constraints on the formation of platinum-group element deposits in igneous rocks. Economic Geology 91, 439-450.

Peck, D.C., Keays, R.R., Ford, R.J., 1992. Direct crystallisation of refractory platinum-group element alloys from boninitic magmas: Evidence from western Tasmania, Australian Journal of Earth Sciences 39, 373-387.

Peck, D.C., and Keays, R.R. 1990. Geology, geochemistry, and origin of platinum-group element-chromite occurrences in the Heazlewood River Complex, Tasmania, Economic Geology 85, 765-793.

Reed, S.J.B., 1996. Electron microprobe analysis and scanning electron microscopy in geology, University of Cambridge, New York, 210 pp.

Rehkamper, M., Halliday, A.N., Fitton, J.G., Lee, D.-C, Wieneke, and Arndt, N.T., 1999. Ir, Ru, Pt, and Pd in basalts and komatiites: new constraints for the geochemical behaviour of the platinum-group elements in the mantle, Geochim. et. Cosmochim. Acta 63, no 22, 39915-3934.

Righter, K., and Hauri, E.H., 1998. Compatibility of rhenium in garnet during mantle melting and magma genesis, Science 280, 1737-1741.

Righter, K., Chesley, J.T., Geist, D., and Ruiz, J., 1998. Behaviour of Re during Magma fractionation: an example from Volcan Alcedo, Galapagos. Journal of Petrology 39, 785-795.

Roeder, P.L., and Emslie, R.F., 1970. Olivine-liquid equilibrium, Contribution to Mineralogy and Petrology 29, 275-289.

Roeder, P.L., Reynolds, I., 1991. Crystallisation of chromite and chromium solubility in basaltic melts, J. of Petrology 32, 909-934.

Roeder, P.L., Jamieson, H.E., 1992. Composition of chromite and co-existing Pt-Fe alloy at magmatic temperatures, Australian Journal of Earth Sciences 39, 419-426.

Roberts, S., 1992. Ophiolites and their Modern Oceanic Analogues. In: Geological Society Special Publication 60, 203-217.

Rollinson, H., 1993. Platinum group element plots. In; Using geochemical data: evaluation, presentation, interpretation, Wiley, New York, 150-154.

Roy-Barman, M., Wasserburg, G.J., Papanastassiou, D.A., Chaussidon, M., 1998. Osmium isotopic compositions and Re-Os concentrations in sulphide globules from basaltic glasses, Earth and Planetary Science Letters 154, 331-37.

Shannon, R.D., and Prewitt, C.T., 1969. Effective Ionic Radii in oxides and Fluorides. Acta. Cryst. B25. 925-946.

Stockman, H.W., and Hlava, P.F., 1984. Platinum-group minerals in Alpine chromitites from Southwestern Oregon, Economic Geology 79, 491-508.

Reed, S.J.B., 1996. Electron microprobe analysis and scanning electron microscopy in geology, University of Cambridge, New York., 210 pp.

Rehkamper, M., Halliday, A.N., Fitton, J.G., Lee, D.-C, Wienekc, and Arndt, N.T., 1999. Ir, Ru, Pt, and Pd in basalts and komatiites: new constraints for the geochemical behaviour of the platinum-group elements in the mantle, Geochim. et. Cosmochim. Acta 63, no 22, 39915-3934.

Righter, K., and Hauri, E.H., 1998. Compatibility of rhenium in garnet during mantle melting and magma genesis, Science 280, 1737-1741.

Righter, K., Chesley, J.T., Geist, D., and Ruiz, J., 1998. Behaviour of Re during Magma fractionation: an example from Volcan Alcedo, Galapagos. Journal of Petrology 39, 785-795.

Roeder, P.L., and Emslie, R.F., 1970. Olivine-liquid equilibrium, Contribution to Mineralogy and Petrology 29, 275-289.

Roeder, P.L., Reynolds, I., 1991. Crystallisation of chromite and chromium solubility in basaltic melts, J. of Petrology 32, 909-934.

Roeder, P.L., Jamieson, H.E., 1992. Composition of chromite and co-existing Pt-Fe alloy at magmatic temperatures, Australian Journal of Earth Sciences 39, 419-426.

Roberts, S., 1992. Ophiolites and their Modern Oceanic Analogues. In: Geological Society Special Publication 60, 203-217.

Rollinson, H., 1993. Platinum group element plots. In; Using geochemical data: evaluation, presentation, interpretation, Wiley, New York, 150-154.

Roy-Barman, M., Wasserburg, G.J., Papanastassiou, D.A., Chaussidon, M., 1998. Osmium isotopic compositions and Re-Os concentrations in sulphide globules from basaltic glasses, Earth and Planetary Science Letters 154, 331-37.

Shannon, R.D., and Prewitt, C.T., 1969. Effective Ionic Radii in oxides and Fluorides. Acta. Cryst. B25. 925-946.

Stockman, H.W., and Hlava, P.F., 1984. Platinum-group minerals in Alpine chromitites from Southwestern Oregon, Economic Geology 79, 491-508.

Sun, S.S., 1982. Chemical composition and origin of the earth's primitive upper mantle, Geochim. et. Cosmochim. Acta 46, 179-192.

Talkington, R.W., and Lipin, B.R., 1986. Platinum-group minerals in chromite seams of the Stillwater Complex, Montana: Economic Geology, 81, 1179-1186.

Tarkian, M., Naidenova, E., and Zhelyaskova-Panayotova, M., 1991. Platinum-group minerals in chromitites from the Eastern Rhodope ultramafic Complex, Bulgaria, Mineralogy and Petrology 44, 73-87.

Thy, P., 1983. Spinel minerals in transitional and alkali basaltic glasses from Iceland, Contributions to Mineralogy and Petrology 83, 141-149.

Torres-Ruiz, J., Garuti, G.,Gazzotti, M., Gervilla, F. and Fenoll Hach-Ali, P., 1996. Platinum-group minerals in chromitites from the Ojen lherzolite massif (Serrania de Ronda, Betic Cordillera, Southern Spain), Mineralogy and Petrology 56, 25-50.

Von Gruenewaldt, G., Hatton, C.J., Merkle, R.K.W., 1986. Platinum-group element-chromite associations in the Bushveld Complex. Economic Geology 81, 1067-1079.

Von Gruenewaldt, G., and Merkle, R.K.W., 1995. Platinum-group element proportions in chromitites of the Bushveld Complex: Implications for fractionation and magma mixing models, Journal of African Earth Sciences 21, 615-632.

Wood, S.A., 1987. Thermodynamic calculations of the volatility of the platinum group elements (PGE): The PGE content of fluids at magmatic temperature, Geochim. et. Cosmochim. Acta 51, 3041-3050.

Zhou, M.-F., Robinson, P. T., Malpas, J., and Li, Z., 1996. Podiform chromitites in the Luobusa ophiolite (Southern Tibet): Implications for melt-rock interaction and chromite segregation in the upper mantle, J. Petrol. 37, 3-21.

Zhou, Mei-Fu, Sun Min, Keays, R.R, and Kerrich R.W., 1998. Controls on platinum-group elemental distributions of podiform chromitites: A case study of high-Cr and high-Al chromitites from Chinese orogenic belts, Geochim. Et. Cosmochim. Acta 62, 677-688.

Table A1. Summary of platinum group element contents (ppb) in mantle rocks in mafic and ultramafic rock types

	Mantle Nodules							Ophiolite Chromitites					
	gt-lhrz	gt-lhrz	gt-lhrz	sp-lhrz	sp-lhrz	lhrz	estimate of mantle	Kef	Oman	Josephine	New Caledonia	Thetford	Luobusa
Os	5.08			3.29			4.02						39.7
Ir	5.35	7	18	3.67	2.95	2.764	4.15	35	50	100	177	30	114
Ru						5.71		80	150	250	235		148
Rh						0.878		7.2	6	14	15		10.4
Pt						5.7	6.74	9.5	13.5	27	17	1.5	2.63
Pd	3.97	5.1	3.7	4.47	4.1	5.29	4.49	2.7	8.4	5	3.2	0.33	2.08
Re	0.19			0.11									
Ref.	*1*	*2*	*3*	*1*	*2*	*4*	*5*	*6*	*6*	*6*	*6*	*7*	*8*
Rock / C1-Chondrite Normalized Values													
Os	0.0099			0.0064			0.0078						0.0772
Ir	0.0099	0.0130	0.0333	0.0068	0.0055	0.0051	0.0077	0.0648	0.0926	0.1852	0.3278	0.0556	0.2111
Ru						0.0083		0.1159	0.2174	0.3623	0.3406		0.2145
Rh						0.0044		0.0360	0.0300	0.0700	0.0750		0.0520
Pt						0.0056	0.0066	0.0093	0.0132	0.0265	0.0167	0.0015	0.0026
Pd	0.0073	0.0094	0.0068	0.0082	0.0075	0.0097	0.0082	0.0050	0.0154	0.0092	0.0059	0.0006	0.0038
Re	0.0054			0.0031									

References

1 = Morgan et al., (1981)
2 = Mitchell and Keays (1981)
3 = sited in Barnes et al., (1985)
4 = Lorand et al., (1998)
5 = Sun (1982)
6 = Page et al., (1982)
7 = Oshin and Crocket (1982)
8 = Zhou et al., (1996)

Table A1. Continued;

	Layered Intrusion chromitites			Basaltic rocks			Ultramafic rocks		C1-Chondrite
	Heazlewood River Complex	UG-2	Stillwater	MORB	Tholeiite	Alkali Basalt	Komatiite Gorgona Island	Alexo flow	
Os	20	108			0.03		1.9556	2.2444	514
Ir	40	415	66	0.0322	0.1325	0.0446	1.8222	2.2222	540
Ru	160	1100	230	0.1130	0.2675	0.1146	3.0667	2.8111	690
Rh	25	834	160						200
Pt	43	2385	535	0.8936	5.2175	0.3692			1020
Pd	7	2395	960	2.0468	7.3570	0.2292	13.1889	8.4556	545
Re				0.927	0.3500				35
***Ref.**	*9*	*10*	*11*	*12, 13*	*12, 13,15*	*12*	*14*	*14*	*15, 16*

Rock / C1-Chondrite Normalized Values

Os	0.0389	0.2101			0.00006		0.0038	0.0044
Ir	0.0741	0.7685	0.1222	0.0001	0.0002	0.0001	0.0034	0.0041
Ru	0.2319	1.5942	0.3333	0.0002	0.0004	0.0002	0.0044	0.0041
Rh		4.1700	0.8000					
Pt	0.0422	2.3382	0.5245	0.0009	0.0051	0.0004		
Pd	0.0128	4.3945	1.7615	0.0038	0.0135	0.0004	0.0242	0.0155
Re				0.0265	0.0100			

References

9 = Peck and Keays (1990)
10 = Von Gruenwaldt and Merkle (1995)
11 = Page et al., (1976)
12 = Hauri and Stanley (1997); Re concnetration in MORB and OIB
13 = Rehkamper et, al., (1999),: PGE concentration in MORB, Tholeiite Basalt,
14 = Brugmann et, al., (1987)
15 = Allegre and Luck (1980); Re concentration in C1-chondrite, Os (ppb) for tholeiite
16 = Naldrett et al., (1981); PGE concentrations C1-chondrite

Table A2. Experimental details

a. Starting material

Experiment I.D.	Silicate to sulphide or alloy (wt%)	Sulphide comp. Fe: Ni: S (wt %)	PGE & Re doped	Sulphur Doped wt%	Graphite-Lined-Pt Capsule	Graphite Capsule	Olivine Capsule
IPRe4	95: 5	50:20:30	1 wt% of Ir, Rh, Pd	N/A	yes		
PGE1b	95: 5	50:20:30	500 ppm of PGEs, Re	N/A	yes		
PGE2b	95: 5	50:20:30	1000 ppm of PGEs, Re	N/A	yes		
PGE1c	95: 5	50:20:30	500 ppm of PGEs, Re	N/A	yes		
PGE2c	95: 5	50:20:30	1000 ppm of PGEs, Re	N/A	yes		
PGE1d	95: 5	50:20:30	500 ppm of PGEs, Re	N/A		yes	
PGE1e	95: 5	50:20:30	500 ppm of PGEs, Re	N/A		yes	
PGE5a	95: 5	50:20:30	5 wt% of PGEs, Re	N/A		yes	
PGECo	95:5		5 wt% of PGEs, Re	N/A	yes		
PGECoS	95:5		5 wt% of PGEs, Re	0.01	yes		
PGE8a	100:00:00		(100 Os, 200 Pd, 500 Rh) ppb	N/A			yes
PGE8b	100:00:00		100 ppb Ru	N/A			yes

b. Summary of liquidus determination experiments[1]

Temperature (°C)	Time (hr)	Present Phases
1400	1.5	Basaltic glass, Sulphide
1360	1.5	Basaltic glass, Sulphide
1300	1.5	Basaltic glass, Chromite, Sulphide
1310	1.5	Basaltic glass, Chromite, Sulphide
1320	1.5	Basaltic glass, Chromite, Sulphide
1330	1.5	Basaltic glass, Chromite, Sulphide
1340	1.5	Basaltic glass, Chromite, Sulphide
1350	1.5	Basaltic glass, Chromite, Sulphide
1355	1.5	Basaltic glass, Sulphide

Notes:

[1] All experiments were performed in a piston cylinder apparatus at 1 GPa, where the charges were first taken to 1460 °C (super-liquidus) and held for 1.5 hrs.

Table A2. Continued;

c. Run conditions for partitioning experiments

Runs #	Super-liquidus T (°C)	Duration (hr)	Liquidus T (°C)	Duration (hr)	Sub-liquidus T (°C)	Duration (hr)	log fO_2 [1]	Std dev.
IPRe4e	1460	1.5	1350	4	1330	48	-8.76	(0.32)
PGE1b	1460	1.5	1350	4	1330	60	-9.28	(0.35)
PGE2b	1460	1.5	1350	4	1330	60	-9.59	(0.56)
PGE1c	1460	1.5	1350	4	1330	30	-8.83	(0.56)
PGE2c	1460	1.5	1350	4	1330	30	-9.06	(0.53)
PGE1d	1460	1.5	1350	4	1330	30	-10.03	(0.37)
PGE1e	1460	1.5	1350	4	1330	60	-9.09	(0.45)
PGE5a	1460	1.5	1350	4	1330	39	-6.99	(0.79)
PGECo	1460	1.5	1350	4	1330	20	-9.71	(0.39)
PGECoS	1460	1.5	1350	4	1330	20	-8.67	(0.59)
PGE8a[2]	1380	72	1350	6	1327	30	-8.5	(0.7)
PGE8b[2]	1380	72	1350	6	1327	30	-8.5	(0.7)

Notes:

[1] Oxygen fugacities were calculated based on Cr-solubility in basaltic melt after Roeder and Reynolds (1991) except for 1 atm runs.

[2] Experiments were performed at 1 atm in gas mixing sealed vertical tube furnace.

Table A2. Continued;

d. Summary of all the phases produced in each experiment

Experiment I.D.	Duration (hrs)	Chromite	Sulphide liquid	Alloy phase
IPRe4[1]	48	x	x	Fe-Re-Ir & Fe-Pt-Pd
PGE1b	60	x	x	Fe-Pt-Rh-Pd
PGE2b	60	x	x	Fe-Pt-Rh-Pd
PGE1c	30	x	x	Fe-Pt-Rh-Pd
PGE2c	30	x	x	Fe-Pt-Rh-Pd
PGE1d	30	x	x	Fe-Pt-Pd-Rh
PGE1e	60	x	x	Fe-Pt-Pd-Rh
PGE5a[1]	39	x	x	Fe-Re-Ir & Fe-Pt-Pd
PGECo	20	x	-	Fe-Co-Re-PGEs
PGECoS	20	x	-	Fe-Co-Re-PGE
PGE8a [2]	30	x	-	-
PGE8b[2]	30	Low nucleation density	-	-

Notes:

[1] The sulphide saturated experiments that were initially doped with greater than 1 wt% PGEs and Re.

[2] Those experiments that were performed at 1 atm with 72 hrs of super-liquidus stage.

Table 3. Operating conditions employed for EMP analysis of run products

3.1. Basaltic glass[1]

Element	Standard	Line	Crystal	Spect.	Time (s) on standard	Time (s) on sample
Na	Albite	Ka	TAP	1	10	10
Si	Basalt[2]	Ka	PET / TAP	3 / 1	10	10
Al	Basalt	Ka	TAP	1	10	10
Mg	Basalt	Ka	TAP	1	10	10
Fe	Basalt	Ka	LIF	2	10	10
Co[3]	CoO	Ka	LIF	2	20	20
Ni[3]	Pentlandite	Ka	LIF	2	20	20
Mn	Bustamite	Ka	LIF	2	10	10
Cr	Chromite	Ka	LIF	2	10	10
Ti	TiO_2	Ka	LIF	2	20	20
Ca	Basalt	Ka	PET	3	10	10
S	Pentlandite	Ka	PET	3	20	20

Notes:

[1] The calibration and analyses were carried out at 15 kV accelerating voltage, a 15 micron diameter defocussed beam of 10 nA. The counting times for background were half the peak counting times.

[2] Juan de Fuca Ridge VG2 glass was used as standard for the basalt analysis.

[3] Ni and Co were analysed using a second condition at 15 kV and a 50 nA beam current.

Table 3. Continued;

3.2. *Chromite*[1]

Element	Standard	Line	Crystal	Spect.	Time (s) on standard	Time (s) on sample
Si	Bustamite	Ka	TAP	3 / 1	10	30
Al	Gahnite	Ka	TAP	1	10	30
Mg	Chromite	Ka	TAP	1	30	30
Fe	Chromite	Ka	LIF	2	40	40
Co	CoO	Ka	LIF	2	30	30
Ni	Pentlandite	Ka	LIF	2	30	30
Mn	Bustamite	Ka	LIF	2	30	30
Cr	Chromite	Ka	PET	2	10	30
Ti	TiO_2	Ka	PET	2	10	30
Ca	Bustamite	Ka	PET	3	20	40
S	Pentlandite	Ka	PET	3	20	20

Notes:

[1] All calibration and analyses were conducted using an accelerating voltage of 20 kV, a focussed beam current of 35 nA, except for calibration of Si, Ca, Mn, Ni, Co, which were at 25 nA, and Ti at 10 nA.

3.3. *Olivine*[1]

Element	Standard	Line	Crystal	Spect.	Time (s) on standard	Time (s) on sample
Mg	Forsterite 85	Ka	TAP	1	10	30
Fe	Forsterite 85	Ka	LIF	2	30	30
Mn	Bustamite	Ka	LIF	2	20	20
Si	Forsterite 85	Ka	PET	3	10	30
Cr	Chromite	Ka	PET	3	10	30
Ca	Bustamite	Ka	PET	3	20	20
Ni[2]	Pentlandite	Ka	LIF	2	10	30

Notes:

[1] All analyses were conducted using an accelerating voltage of 20 kV, a focussed beam current of 30 nA.

[2] Ni was analysed with a beam current of 100 nA using a second condition.

Table A3. Continued;

3.4. clino-pyroxene[1]

Element	Standard	Line	Crystal	Spect.	Time (s) on standard	Time (s) on sample
Na[2]	albite	Ka	TAP	1	10	30
Al	pxTiAl	Ka	TAP	1	20	20
Mg	enstatite	Ka	TAP	1	10	25
Si	Kakaugite	Ka	TAP	1	10	20
Ni	Pentlandite	Ka	LIF	2	10	15
Fe	Hypersthine	Ka	LIF	2	10	50
Mn	Bustamite	Ka	LIF	2	10	10
Cr	Chromite	Ka	LIF	2	10	20
k	Sanidine	Ka	PET	3	10	10
Ca	Bustamite	Ka	PET	3	10	30
Ti	pxTiAl	Ka	PET	3	10	30

Notes:

[1] All analyses were carried out using an accelaring voltage of 15kV, a focussed beam current of 30 nA.

[2] Sodium was calibrated with a 15 micron diameter beam current of 25 nA.

3.5. Alloy [1]

Element	Standard	Line	Crystal	Spect.	Time (s) on standard	Time (s) on sample
Fe	Pentlandite	Ka	LIF	1	10	10
Co	Co	Ka	LIF	1	10	10
Re	Re	La	LIF	2	10	25
Os	Os	La	LIF	2	10	25
Ir	Ir	La	LIF	2	10	25
Ru[2]	Ru	La	PET	3	10	25
Rh[2]	Rh	La	PET	3	10	25
Pd	Pd	La	PET	3	10	25

Notes:

[1] All analyses were conducted using an 20 kV accelerating voltage, a focussed beam current of 60 nA.

[2] The Ru , and Pd interferences on Rh were resolved using an overlap correction procedure produced by Cameca software.

Table A3. Continued;

3.6. Sulphide [1]

Element	Standard	Line	Crystal	Spect.	Time (s) on standard	Time (s) on sample
Fe	Pentlandite	Ka	LIF	1	10	10
Ni	Pentlandite	Ka	LIF	2	10	10
S	Pentlandite	Ka	PET	3	10	10
Re	Re	La	LIF	2	10	20
Os	Os	La	LIF	2	10	20
Ir	Ir	La	LIF	2	10	20
Ru	Ru	La	PET	3	10	20
Rh	Rh	La	PET	3	10	20
Pd	Pd	La	PET	3	10	20

Notes:

[1] All analyses were completed using a 15 kV accelerating voltage, and a 15 micron in diameter defocussed beam current of 15nA. Re and PGEs were analysed using a second condition at 15kV and a 100 nA beam current.

Table A4. The minimum detection limit (ppm) of Re and PGEs in NIST 610 Glass from run analysis [1]

Samples	Re	Ru	Rh	Pd	Os	Ir	Pt
PGE1b	0.0071	0.0523	0.01336	0.0634	0.0147	0.0108	0.0246
PGE2b	0.002	0.0293	0.0116	0.0484	0.01624	0.009	0.02142
PGE1c	0.0074	0.0644	0.0214	0.0867	0.0497	0.041	0.0208
PGE2c	0.0041	0.0378	0.0075	0.031	0.0338	0.0059	0.0137
PGE1d	0.015	0.0392	0.024	0.089	0.02	0.012	0.029
PGE1e	0.0068	0.0341	0.01	0.0475	0.0273	0.0069	0.0144
IPRe4	0.0052	0.0436	0.01146	0.0608	0.0052	0.0059	0.0092
PGE5a	0.015			0.11		0.035	0.1122
PGECo	0.0102	0.0377	0.0139	0.0537	0.0046	0.0047	0.0072
PGECoS	0.0105		0.0254	0.1734	0.0105	0.0373	0.0429
PGE8a	0.06	0.16	0.04	0.23	0.02	0.01	0.03
PGE8b	0.06	0.09	0.02	0.12	0.015	0.05	0.01

[1] Run detection limit based on count rates of 2 sigma above background.

Table A5. Summary of major element composition (wt%) of phases produced in partitioning experiments (numbers in parentheses represent 1σ precisions of multiple analyses)

5.1. Basaltic Glass (20 points analysed in each sample)

Sample #	Na_2O	SiO_2	TiO_2	MnO	Cr_2O_3	FeO	MgO	Al_2O_3	CaO	SO_2	CoO	Total
IPRe4	2.75 (0.11)	52.31 (0.24)	1.73 (0.19)	0.19 (0.05)	0.44 (0.03)	10.17 (0.14)	7.97 (0.1)	15.21 (0.11)	9.11 (0.16)	0.05		99.92
PGE1b	2.75 (0.12)	52.06 (0.35)	1.80 (0.18)	0.18 (0.05)	0.54 (0.04)	10.09 (0.18)	8.12 (0.12)	14.55 (0.09)	9.18 (0.11)	0.09		99.37
PGE2b	2.63 (0.28)	52.22 (0.61)	1.95 (0.20)	0.16 (0.04)	0.60 (0.04)	9.73 (0.13)	8.08 (0.10)	14.62 (0.16)	9.36 (0.12)	0.08		99.43
PGE1c	2.57 (0.11)	51.88 (0.44)	1.92 (0.27)	0.18 (0.07)	0.49 (0.06)	9.82 (0.23)	8.04 (0.15)	14.25 (0.14)	9.38 (0.12)	0.08 (0.01)		98.61
PGE2c	2.79 (0.1)	51.98 (0.44)	1.89 (0.18)	0.16 (0.06)	0.45 (0.05)	10.32 (0.16)	8.05 (0.19)	14.50 (0.15)	9.21 (0.16)	0.07 (0.01)		99.40
PGE1d	3.78 (0.12)	50.66 (0.73)	1.78 (0.21)	0.16 (0.05)	0.48 (0.04)	10.75 (0.38)	7.59 (0.11)	14.07 (0.12)	9.05 (0.12)	0.29 (0.01)		98.63
PGE1e	2.85 (0.07)	51.51 (0.50)	1.77 (0.14)	0.15 (0.07)	0.50 (0.05)	9.50 (0.30)	7.82 (0.12)	14.41 (0.11)	9.16 (0.14)	0.26 (0.02)		97.94
PGE5a	4.06 (0.11)	52.32 (0.47)	1.77 (0.07)	0.19 (0.07)	0.17 (0.04)	10.14 (0.20)	7.50 (0.13)	14.09 (0.15)	9.14 (0.10)	0.19 (0.01)		99.57
PGECo	2.74 (0.07)	52.81 (0.27)	1.91 (0.15)	0.18 (0.06)	0.63 (0.05)	8.62 (0.22)	7.00 (0.08)	14.40 (0.18)	9.79 (0.09)		0.25 (0.02)	98.09
PGECoS	2.75 (0.08)	52.61 (0.22)	1.92 (0.14)	0.18 (0.04)	(0.42) (0.06)	9.26 (0.16)	6.56 (0.11)	14.16 (0.09)	9.73 (0.15)		0.21 (0.02)	97.37
PGE8a	1.98 (0.08)	51.77 (0.25)	1.43 (0.07)	0.20 (0.05)	0.27 (0.04)	10.93 (0.28)	14.85 (0.14)	12.31 (0.13)	8.06 (0.15)			101.81
PGE8b	1.84 (0.09)	50.02 (0.48)	1.47 (0.14)	0.19 (0.04)	0.24 (0.03)	10.83 (0.26)	14.76 (0.22)	12.38 (0.14)	8.05 (0.14)			99.80

5.2. Clinopyroxene (10 points analysed)

PGE5a	0.786 (0.097)	53.235 (0.689)	0.6347 (0.142)	0.163 (0.018)	1.997 (0.315)	7.069 (0.576)	18.313 (1.279)	4.889 (0.973)	12.908 (1.069)			99.993

Table A5. Continued;

5.3. Chromite (10 points analysed in each sample)

Sample #	SiO_2	TiO_2	MnO	Cr_2O_3	FeO	MgO	Al_2O_3	CoO	NiO	Total
IPRe4	0.11 (0.01)	0.76 (0.01)	0.21 (0.01)	50.39 (0.29)	18.97 (0.12)	11.16 (0.16)	17.49 (0.23)			99.10
PGE1b	0.16 (0.02)	0.75 (0.02)	0.22 (0.01)	53.97 (0.65)	18.77 (0.07)	10.97 (0.27)	14.85 (0.58)			99.67
PGE2b	0.12 (0.02)	0.76 (0.04)	0.23 (0.01)	54.11 (0.67)	18.31 (0.12)	11.24 (0.16)	15.05 (0.63)			99.83
PGE1c	0.12 (0.07)	0.80 (0.04)	0.22 (0.01)	52.72 (1..21)	19.61 (0.13)	10.49 (0.29)	15.02 (0.88)			98.99
PGE2c	0.10 (0.13)	0.78 (0.02)	0.22 (0.01)	53.37 (0.67)	19.52 (0.12)	11.38 (2.56)	14.44 (1.21)			99.81
PGE1d	0.12 (0.02)	0.77 (0.03)	0.21 (0.01)	53.67 (0.29)	20.16 (0.11)	10.24 (0.44)	14.34 (0.62)			99.52
PGE1e	0.10 (0.01)	0.78 (0.03)	0.23 (0.01)	54.52 (0.39)	18.88 (0.08)	10.94 (0.25)	14.28 (0.36)			99.73
PGE5a	0.08 (0.04)	0.75 (0.07)	0.23 (0.01)	54.29 (1.15)	20.33 (0.26)	9.98 (0.18)	13.42 (0.33)		0.07 (0.01)	99.15
PGECo	0.12 (0.11)	0.68 (0.02)	0.25 (0.02)	54.42 (0.58)	17.74 (0.11)	10.60 (0.23)	13.21 (0.43)	1.18 (0.02)		98.20
PGECoS		0.80 (0.02)	0.25 (0.02)	52.43 (0.62)	18.84 (0.09)	9.69 (0.45)	13.76 (0.74)	1.08 (0.02)		96.84
PGE8a	0.11 (0.01)	0.93 (0.01)	0.18 (0.01)	53.76 (0.46)	15.13 (0.09)	14.22 (0.39)	14.13 (0.39)		0.17 (0.02)	98.64

Table A5. Continued;

5.4. Olivine (10 points analysed in each sample)

Sample #	SiO_2	MgO	FeO	MnO	Cr_2O_3	CaO	NiO	Total
PGE8a	40.38	47.55	11.42	0.14	0.21	0.19	0.40	100.29
	(0.17)	(0.24)	(0.13)	(0.01)	(0.01)	(0.01)	(0.01)	
PGE8b	41.14	47.39	10.53	0.14	0.14	0.17	0.38	99.89
	(0.12)	(0.45)	(1.04)	(0.01)	(0.04)	(0.02)	(0.03)	

5.5. Sulphides (40 points analysed in each sample)

Sample #	Fe	Ni	S	O	Total
IPRe4[1]	35.20	28.95	31.08	0.35	95.58
PGE1b	56.95	5.00	34.00	2.42	98.37
PGE2b	53.33	11.28	34.01	0.57	99.19
PGE1c	49.18	15.16	33.72	0.61	98.67
PGE2c	50.39	14.15	33.14	1.00	98.68
PGE1d	47.12	18.70	32.86		98.68
PGE1e	45.65	18.60	34.17		98.42
PGE5a[1]	33.36	27.25	27.18		87.79

Table A5. Continued;

5.6. Alloys

Sample #	Fe	Ni	Co	Ru	Rh	Pd	Re	Os	Ir	Total
PGECo[2]	4.95	NA[4]	0.83	8.33	24.96	18.26	9.25	13.08	20.32	99.98
	(2.61)		(0.29)	(4.77)	3.79	(2.46)	(5.61)	(8.01)	(8.44)	
PGECo[3]	6.53	NA	1.07	6.18	35.85	11.85	7.97	7.92	23.55	100.93
	(0.33)		(0.06)	(0.65)	(0.89)	(1.65)	(1.66)	(0.55)	(0.34)	
IPRe4	1.41	0.33	NA	NA	NA	NA	38.30	NA	59.34	99.47
	(0.12)	(0.03)					(1.74)		(1.46)	

Notes:

[1] samples with totals less than 95%,, which also contained 5-11 wt% Pd, and some Pt.
[2] average of 3 points within the crystalline alloy.
[3] average of 10 points within the anhedral-shaped alloy.
[4] NA represents the elements that are not analysed.

Table A6. Summary of PGEs. Re and Ni concentrations (ppm) of all phases in this study **(numbers in parentheses show the 1σ error of the mean of analyses)**

6.1. Basaltic glass

Samples	# of pts	Ni	Ru	Rh	Pd	Re	Os	Ir	Pt
PGE1b	4 pts	88.29 (7.71)	<0.0534	<0.02	<0.12	0.015 (0.003)	<0.03	<0.01	<0.04
PGE2b	3 pts	28.25 (6.73)	<0.04	<0.02	<0.07	0.029 (0.006)	<0.02	<0.01	<0.03
PGE1c	3 pts	213.52 (32)	<0.053	<0.04	<0.16	0.016 (0.006)	<0.019	<0.02	<0.057
PGE2c	3 pts	105.61 (14.24)	0.0440 (0.0131)	<0.1	<0.08	0.028 (0.009)	<0.021	<0.008	0.051
PGE1d	3 pts	131.00 (18.98)	<0.057	<0.02	<0.1	0.013 (0.005)	<0.026	<0.02	<0.031
PGE1e	4 pts	143.66 (18.97)	<0.075	<0.01	<0.06	0.012 (0.002)	<0.01	<0.01	<0.02
IPRe4	8 pts	221.75 (35.25)			0.374 (0.189)	0.041 (0.014)		0.127 (0.083)	1.030 (0.08)
PGE5a	5 pts	82.50 (6.5)			<0.16	<0.02		<0.028	<0.04
PGECo	15 pts		0.270 (0.119)	3.164 (1.591)	0.290 (0.165)	8.601 (6.067)	0.122 (0.122)	<0.02	0.584 (0.2)
PGECoS	6 pts			2.984 (0.462)	<0.4	15.327 (3.432)			
PGE8a^1	5 pts	414.50 (14.72)	<0.35	<0.12	<0.48	<0.09	<0.03	<0.03	0.11
PGE8b^1	3 pts	375.67 (24.96)	<0.16	<0.06	<0.37	<0.29	<0.02	<0.01	<0.03

Table A6. Continued;

6.2. Chromite

Samples	no of pts	Ni	Ru	Rh	Pd	Os	Re	Ir	Pt
PGE1b	1 pts	587	<1.15	<0.8	<3.63	<1.09	0.88 (0.11)	<0.57	<1.21
PGE2b	1 pts	207	<2.71	<0.77	<3.98	<1.74	0.82 (0.21)	<0.7	<1.52
PGE1c	1 pts	720	<1.43	<0.62	<2.52	<0.33	<0.28	<0.37	0.91
PGE2c	2 pts	502	<1.68	<0.53	<6.36	<0.31	<1.69	<0.39	<2.87
PGE1d	2 pts	571	<2.79	<0.89	<2.51	<0.94	<0.63	<0.49	<1.39
PGE1e	2 pts	587	<2.86	<0.52	<3.86	<0.58	<0.33	<0.43	<0.61
IPRe4	1 pts	854			<0.087		<0.34	<0.15	1.32
PGE5a	1 pts	380			<4.62		<0.74	<0.77	<1.86
PGECo	6 pts		<2.77	<0.53	<5.00	<0.52	1.29 (0.62)	<0.47	<0.58
PGECoS	1 pts			<0.39	<2.98		0.68		<0.41
PGE8a	1 pts	1700	<25.81	<11.62	<77.33	<6.88	<14.28	<2.99	<7.6

Table A6. Continued;

6.3. Olivine

Sample #	# of pts	Ni	Ru	Rh	Pd	Os	Pt
PGE8a	3	3120 (250)	<0.29	<0.1	<0.87	<0.04	<0.11
PGE8b	2	2954 (789)	<0.3	<0.14	<0.63	<0.03	0.1

6.4. Sulphides

Samples #	# of pts	Ni	Ru	Rh	Pd	Re	Os	Ir	Pt
PGE1b	3 pts	79778 (10997)	308.12 (95.38)	206.30 (52.32)	626.44 (146.52)	189.78 (14.53)	164.36 (62.99)	297.81 (118.96)	435.31 (325.33)
PGE2b	6 pts	39557 (2145)	719.62 (58.01)	129.33 (96.99)	696.30 (281.11)	396.64 (103.88)	409.25 (126.09)	8098.40 (150.68)	821.80 (240.22)
PGE1c	5 pts	157215 (36638)	210.82 (69.13)	2.69 (1.39)	466.08 (217.58)	52.98 (9.69)	281.02 (97.86)	181.70 (98.79)	172.13 (56.21)
PGE2c	3 pts	144516 (2753)	722.26 (112.73)	36.62 (22.11)	870.45 (159.73)	166.97 (103.91)	189.21 (10.93)	358.81 (142.37)	210.40 (121.80)
PGE1d	3 pts	137303 (20947)	290.55 (44.607)	10.22 (12.33)	464.55 (221.32)	137.13 (20.15)	173.95 (42.08)	94.42 (46.62)	78.09 (72.81)
PGE1e	3 pts	152167 (37618)	401.67 (74.51)	7.16 (3.59)	329.87 (209.17)	223.18 (84.39)	312.95 (122.86)	136.35 (0.51)	242.26 (207.64)
IPRe4	3 pts	277833 (5760)		743.33 (5.44)	10957.00 (558.43)	86.33 (14.66)	3.34 (0.82)	2041.20 (109.9)	66.51 (20.98)
PGE5a	2 pts	130514 (9780)			24467.00 (3305)	10.25 (5.55)		826.10 (384.3)	46.05 (9.95)

Table A7.1. Summary of sulphide-melt/silicate melt partition coefficients measured in this study

Sample #	Ni	Re	Os	Ir	Ru	Rh	Pd
PGE1b	904	13081	>5479	>29781	>5770	>10315	>5220.33
PGE2b	1400	13591	>20462	>80919	>17990	>6466	>9947.14
PGE1c	672	2391	>14791	>9085	>3977	>67.25	>2913
PGE2c	1368	6207	>9167	>47212	>16377	>366	>10881
PGE1d	1120	10311	>6768	>4721	>5115	>511	>4646
PGE1e	1059	18323	>31295	>13635	>5355	>716	>5498
IPRe4	1062	2116		16136			29290
PGE5a	1582	513		>29504			>152919

Table A7.2. Summary of chromite/silicate-melt partition coefficients measured in this study

Sample #	Ni	Re	Os	Ir	Ru	Rh	Pd
PGE1b	3.8 (0.6)	<60.7	<46.3	<57	<40.64	<40	<30.2
PGE2b	6.6 (0.8)	<28.1	<87	<70	<67.8	<38.5	<56.9
PGE1c	7.3 (1.8)	<19.4	<17.4	<18.5	<26.9	<16	<15.8
PGE2c	3.4 (0.5)	<61.2	<9.8	<19.5	<78.9	<5.3	<79.5
PGE1d	4.8 (0.6)	<47.4	<36.6	<64.5	<49.1	<44.5	<25.1
PGE1e	4.4 (1.5)	<27.1	<43	<14	<38.1	<52.9	<64.3
IPRe4	4.1 (0.6)	<8.3		≤1.2			≤0.23
PGECo		0.15 (0.12)	<4.3	<17.3	<10.2	<0.1675	<17.3
PGECoS		0.044 (0.009)				<0.13	<7.4
PGE8a	4.1 (0.2)						

Table A.I. Summary of recalculations of chromite analyses

Experiment #	IPRe4							Mg #	$Cr^{3+}/(Cr^{3+}+Fe^{3+}+Al^{3+})$	Cr #
Oxides	wt%	MW	mol prop	Prop. of Cation		no of cation in formula				
SiO_2	0.1078	60.08	0.002	0.002	Si	0.003				
TiO_2	0.7643	79.88	0.010	0.010	Ti	0.018				
Al_2O_3	17.4867	101.96	0.172	0.343	Al	0.659				
Cr_2O_3	50.3861	151.99	0.332	0.663	Cr	1.274		53.531	0.644	64.393
Fe_2O_3		159.69			Fe3					
FeO	18.975	71.85	0.264	0.264	Fe2	0.507				
MnO	0.2123	70.94	0.003	0.003	Mn	0.006				
MgO	11.1641	40.3	0.277	0.277	Mg	0.532				
ZnO		81.38			Zn					
CaO		56.08			Ca					
Total	99.0963			1.562						
						Total Divalent Cation	0.538			
	Oxygen factor = 3/[Oxg]= 1.921					Fe^{2+}	0.462			
						Fe^{3+}	0.045			

	PGE1b									
Oxides	wt%	MW	mol prop	Prop. of Cation		no of cation in formula				
SiO_2	0.1552	60.08	0.003	0.003	Si	0.005				
TiO_2	0.7472	79.88	0.009	0.009	Ti	0.018				
Al_2O_3	14.854	101.96	0.146	0.291	Al	0.564				
Cr_2O_3	53.968	151.99	0.355	0.710	Cr	1.375		52.982	0.695	69.536
Fe_2O_3		159.69			Fe3					
FeO	18.768	71.85	0.261	0.261	Fe2	0.506				
MnO	0.2173	70.94	0.003	0.003	Mn	0.006				
MgO	10.965	40.3	0.272	0.272	Mg	0.527				
ZnO		81.38			Zn					
CaO		56.08			Ca					
Total	99.6747			1.550						
						Total Divalent Cation	0.533			
	Oxygen factor = 3/[Oxg]= 1.936					Fe^{2+}	0.467			
						Fe^{3+}	0.038			

	PGE2b									
Oxides	wt%	MW	mol prop	Prop. of Cation		no of cation in formula				
SiO_2	0.119818	60.08	0.002	0.002	Si	0.004				
TiO_2	0.76454	79.88	0.010	0.010	Ti	0.018				
Al_2O_3	15.05245	101.96	0.148	0.295	Al	0.569				
Cr_2O_3	54.11273	151.99	0.356	0.712	Cr	1.373		54.116	0.694	69.423
Fe_2O_3		159.69			Fe3					
FeO	18.30973	71.85	0.255	0.255	Fe2	0.491				
MnO	0.23036	70.94	0.003	0.003	Mn	0.006				
MgO	11.23955	40.3	0.279	0.279	Mg	0.538				
ZnO		81.38			Zn					
CaO		56.08			Ca					
Total	99.629178			1.556						
						Total Divalent Cation	0.544			
	Oxygen factor = 3/[Oxg]= 1.928					Fe^{2+}	0.456			
						Fe^{3+}	0.035			

Table A.I. Continued;

	PGE1c									
		MW	mol prop	Prop. of		no of cation in formula		Mg #	$Cr^{3+}/(Cr^{3+}+Fe^{3+}+Al^{3+})$	Cr #
Oxides	wt%			Cation						
SiO_2	0.12457	60.08	0.002	0.002	Si	0.004				
TiO_2	0.80136	79.88	0.010	0.010	Ti	0.020				
Al_2O_3	15.0175	101.96	0.147	0.295	Al	0.575				
Cr_2O_3	52.7239	151.99	0.347	0.694	Cr	1.354		51.125	0.685	68.527
Fe_2O_3		159.69			Fe3					
FeO	19.6091	71.85	0.273	0.273	Fe2	0.533				
MnO	0.22014	70.94	0.003	0.003	Mn	0.006				
MgO	10.4904	40.3	0.260	0.260	Mg	0.508				
ZnO		81.38			Zn					
CaO		56.08			Ca					
Total	98.98697			1.537						
						Total Divalent Cation	0.514			
	Oxygen factor = 3/[Oxg]= 1.952					Fe^{2+}	0.486			
						Fe^{3+}	0.047			
	PGE2c									
		MW	mol prop	Prop. of		no of cation in formula				
Oxides	wt%			Cation						
SiO_2	0.1	60.08	0.002	0.002	Si	0.003				
TiO_2	0.7799	79.88	0.010	0.010	Ti	0.019				
Al_2O_3	14.4439	101.96	0.142	0.283	Al	0.547				
Cr_2O_3	53.3738	151.99	0.351	0.702	Cr	1.356		54.820	0.685	68.541
Fe_2O_3		159.69			Fe3					
FeO	19.5221	71.85	0.272	0.272	Fe2	0.524				
MnO	0.21582	70.94	0.003	0.003	Mn	0.006				
MgO	11.378	40.3	0.282	0.282	Mg	0.545				
ZnO		81.38			Zn					
CaO		56.08			Ca					
Total	99.81352			1.554						
						Total Divalent Cation	0.551			
	Oxygen factor = 3/[Oxg]= 1.930					Fe^{2+}	0.449			
						Fe^{3+}	0.075			
	PGE1d									
		MW	mol prop	Prop. of		no of cation in formula				
Oxides	wt%			Cation						
SiO_2	0.12165	60.08	0.002	0.002	Si	0.004				
TiO_2	0.77113	79.88	0.010	0.010	Ti	0.019				
Al_2O_3	14.2812	101.96	0.140	0.280	Al	0.547				
Cr_2O_3	53.7147	151.99	0.353	0.707	Cr	1.381		49.872	0.699	69.851
Fe_2O_3		159.69			Fe3					
FeO	20.117	71.85	0.280	0.280	Fe2	0.547				
MnO	0.2136	70.94	0.003	0.003	Mn	0.006				
MgO	10.2257	40.3	0.254	0.254	Mg	0.496				
ZnO		81.38			Zn					
CaO		56.08			Ca					
Total	99.44498			1.535						
						Total Divalent Cation	0.502			
	Oxygen factor = 3/[Oxg]= 1.954					Fe^{2+}	0.498			
						Fe^{3+}	0.049			

Table A.I. Continued;

PGE1e

Oxides	wt%	MW	mol prop	Prop. of Cation		no of cation in formula		Mg #	$Cr^{3+}/(Cr^{3+}+Fe^{3+}+Al^{3+})$	Cr #
SiO_2	0.010233	60.08	0.000	0.000	Si	0.000				
TiO_2	0.7778	79.88	0.010	0.010	Ti	0.019				
Al_2O_3	14.28017	101.96	0.140	0.280	Al	0.544				
Cr_2O_3	54.5249	151.99	0.359	0.717	Cr	1.393		53.061	0.703	70.334
Fe_2O_3		159.69			Fe3					
FeO	18.8783	71.85	0.263	0.263	Fe2	0.510				
MnO	0.2275	70.94	0.003	0.003	Mn	0.006				
MgO	10.944	40.3	0.272	0.272	Mg	0.527				
ZnO		81.38			Zn					
CaO		56.08			Ca					
Total	99.642903			1.545						
						Total Divalent Cation	**0.534**			
	Oxygen factor = 3/[Oxg]= 1.942					**Fe^{2+}**	**0.466**			
						Fe^{3+}	**0.044**			

PGE5a

Oxides	wt%	MW	mol prop	Prop. of Cation		no of cation in formula				
SiO_2	0.0753	60.08	0.001	0.001	Si	0.002				
TiO_2	0.75465	79.88	0.009	0.009	Ti	0.019				
Al_2O_3	13.4198	101.96	0.132	0.263	Al	0.519				
Cr_2O_3	54.2893	151.99	0.357	0.714	Cr	1.408		49.120	0.711	71.149
Fe_2O_3		159.69			Fe3					
FeO	20.33033	71.85	0.283	0.283	Fe2	0.558				
MnO	0.2293	70.94	0.003	0.003	Mn	0.006				
MgO	9.9799	40.3	0.248	0.248	Mg	0.488				
ZnO		81.38			Zn					
CaO		56.08			Ca					
Total	99.07858			1.522						
						Total Divalent Cation	**0.494**			
	Oxygen factor = 3/[Oxg]= 1.971					**Fe^{2+}**	**0.506**			
						Fe^{3+}	**0.052**			

PGECo

Oxides	wt%	MW	mol prop	Prop. of Cation		no of cation in formula				
SiO_2	0.117167	60.08	0.002	0.002	Si	0.004				
TiO_2	0.68225	79.88	0.009	0.009	Ti	0.017				
Al_2O_3	13.21008	101.96	0.130	0.259	Al	0.518				
Cr_2O_3	54.4217	151.99	0.358	0.716	Cr	1.433		53.024	0.724	72.406
Fe_2O_3		159.69			Fe3					
FeO	17.73953	71.85	0.247	0.247	Fe2	0.494				
MnO	0.25	70.94	0.004	0.004	Mn	0.007				
MgO	10.60396	40.3	0.263	0.263	Mg	0.527				
ZnO		81.38			Zn					
CaO		56.08			Ca					
Total	97.024687			1.499						
						Total Divalent Cation	**0.534**			
	Oxygen factor = 3/[Oxg]= 2.001					**Fe^{2+}**	**0.466**			
						Fe^{3+}	**0.028**			

Table A.I. Continued;

PGECoS

Oxides	wt%	MW	mol prop	Prop. of Cation		no of cation in formula		Mg #	$Cr^{3+}/(Cr^{3+}+Fe^{3+}+Al^{3+})$	Cr #
SiO_2		60 08	0 017	0 017	Si	0 033				
TiO_2	0.80225	79 88	0.010	0.010	Ti	0 020				
Al_2O_3	13.7575	101.96	0.135	0.270	Al	0.542				
Cr_2O_3	52.432	151.99	0.345	0.690	Cr	1.387		48.659	0.712	71.248
Fe_2O_3		159.69			Fe3					
FeO	18.8385	71.85	0.262	0.262	Fe2	0.527				
MnO	0.2485	70.94	0.004	0.004	Mn	0.007				
MgO	9.6875	40.3	0.240	0.240	Mg	0.483				
ZnO		81.38			Zn					
CaO		56.08			Ca					
Total	95.76625			1.493						
						Total Divalent Cation	0.490			
	Oxygen factor = 3/[Oxg]= 2.010					Fe^{2+}	0.510			
						Fe^{3+}	0.017			

PGE8a

Oxides	wt%	MW	mol prop	Prop. of Cation		no of cation in formula		Mg #	$Cr^{3+}/(Cr^{3+}+Fe^{3+}+Al^{3+})$	Cr #
SiO_2	0.3372	60 08	0.006	0.006	Si	0.011				
TiO_2	0.9177	79 88	0.011	0.011	Ti	0.022				
Al_2O_3	14.617	101 96	0.143	0.287	Al	0.542				
Cr_2O_3	53.984	151.99	0.355	0.710	Cr	1.343		68.622	0.712	71.244
Fe_2O_3		159.69			Fe3					
FeO	15.066	71.85	0 210	0 210	Fe2	0.396				
MnO	0	70.94	0.000	0.000	Mn	0.000				
MgO	14 628	40.3	0.363	0.363	Mg	0.686				
ZnO		81.38			Zn					
CaO		56.08			Ca					
Total	99.5499			1.587						
						Total Divalent Cation	0.686			
	Oxygen factor = 3/[Oxg]= 1.891					Fe^{2+}	0.314			
						Fe^{3+}	0.083			

Table A.11. Summary of recalculations of olivine analyses

	PGE8a										Fo
Oxides	wt%	MW	mol prop	atom prop of Oxg for each mol	No anion based on 4	**Cations**		**Atomic Ratio**	**Fe*=(Fe2++Fe3++Mn2+)**	**Mg+Fe**	**100Mg/(Mg+Fe*)**
MgO	47.003	40.300	1.166	1.166	1.745	**Mg**	1.745				
SiO_2	40.400	60.080	0.672	1.345	2.012	**Si**	1.006	**1.000**			
FeO	11.190	71.850	0.156	0.156	0.233	**Fe^{2+}+Fe^{3+}**	0.233				
MnO	0.067	70.940	0.001	0.001	0.001	**Mn**	0.001		**0.234**	**1.979**	**88.157**
Cr_2O_3	0.165	151.990	0.001	0.003	0.005	**Cr^{3+}**	0.003				
NiO	0.230	74.690	0.003	0.003	0.005	**Ni**	0.005				
								1.987			
Total	99.055			2.674							

Oxg fact= 4/[Oxg]= 1.496

	PGE8b										
Oxides	wt%	MW	mol prop	atom prop of Oxg for each mol	No anion based on 4	**Cations**		**Atomic Ratio**	**Fe*=(Fe2++Fe3++Mn2+)**	**Mg+Fe**	**100Mg/(Mg+Fe*)**
MgO	47.39	40.3	1.176	1.176	1.741	**Mg**	1.741				
SiO_2	41.14	60.08	0.685	1.370	2.028	**Si**	1.014	**1.000**			
FeO	10.53	71.85	0.147	0.147	0.217	**Fe^{2+}+Fe^{3+}**	0.217				
MnO	0.14	70.94	0.002	0.002	0.003	**Mn**	0.003		**0.220**	**1.961**	**88.79**
Cr_2O_3	0.14	151.99	0.001	0.003	0.004	**Cr^{3+}**	0.003				
NiO	0.38	74.69	0.005	0.005	0.008	**Ni**	0.008				
								1.971			
Total	99.72			2.702							

Oxg fact= 4/[Oxg]= 1.480